Experimental and theoretical study on the vortex system of a tubercled wing:

from leading-edge vortex to stall cells

Haozhe Zeng
(5698065)

TU Delft

Experimental and theoretical study on the vortex system of a tubercled wing:

from leading-edge vortex to stall cells

Thesis report

by

Haozhe Zeng
(5698065)

to obtain the degree of Master of Science
at the Delft University of Technology
to be defended publicly on September 19, 2024 at 10:00

Thesis committee:	
Chair:	Dr. F. Scarano
Supervisors:	Dr. M. Li
	Dr. S.J. Hulshoff
External examiner:	Dr. A. Sciacchitano
Place:	Faculty of Aerospace Engineering, Delft
Project Duration:	January, 2024 - September, 2024
Student number:	5698065

Faculty of Aerospace Engineering · Delft University of Technology

Abstract

Wings with leading-edge (LE) tubercles have gained increasing attention over the past decade. Despite their impressive aerodynamic performance, the underlying flow control mechanisms of tubercles remain controversial. In this thesis, both experimental and theoretical approaches are employed to investigate the flow patterns of a tubercled wing at pre-stall and post-stall angles of attack (AoAs).

In the experimental study, 2D Particle Image Velocimetry (PIV) was used to measure flow patterns at cross-flow planes along the chord. At a pre-stall AoA, high-vorticity regions generated by the tubercles appear in an alternating pattern near the LE. A quantitative comparison was conducted to examine the similarities between a tubercle and a delta wing. The results show that tubercles cannot be regarded as small delta wings in terms of vortex generation. The leading-edge vortex (LEV) sheets are convected downstream, where they interact with laminar separation bubbles (LSBs), creating complex flow patterns in the downstream regions. At a post-stall AoA, stall cells (SCs) appear along the span, with their formation dependent on both Reynolds number (Re) and tubercle amplitude. However, the spacing of SCs is relatively independent of AoA, Re, and amplitude, consistently ranging between 5 to 7 tubercle wavelengths.

In the theoretical study, the lifting line theory (LLT) approach was first used to predict the LEV strength but proved ineffective due to the absence of thickness effects. A subsequent analysis using the panel method in xflr5 showed that the Kutta condition should also be applied to the leading edge (LE) rather than only to the trailing edge (TE). Crow's model was adapted by taking LEVs into consideration. However, a global description of the instability was not obtained due to difficulties in representing LEVs and related mathematical challenges.

This thesis contributes to a further understanding of the tubercle's role in flow control. The LEVs generated by the tubercles are identified as key factors influencing flow evolution, yet these effects are not captured by LLT-based models or a conventional panel method. Future reduced-order models (ROMs) should account for the influence of LEVs to provide accurate representations of tubercled wing flow dynamics.

Contents

List of Figures

List of Tables

Nomenclature

List of Abbreviations

AoA	Angle of attack
BL	Boundary layer
FOV	Field of view
fps	Frames per second
KJ	Kutta-Joukowski
LE	Leading edge
LEV	Leading-edge vortex
LLT	Lifting line theory
LSB	Laminar separation bubble
NLLT	Non-linear lifting line theory
NLLT	Nonlinear lifting line theory
OJF	Oil flow visualization
PIV	Particle image velocimetry
PTU	Programmable time unit
ROM	Reduced-order modeling
RPM	Revolutions per minute
SC	Stall cell
SNR	Signal-to-noise ratio
std	Standard deviation
TE	Teading edge
TSR	Tip speed ratio
UAV	Unmanned aerial vehicle

List of Symbols

λ	Tubercle wavelength
A	Tubercle amplitude
C_D	3D drag coeffcient
$C_{L,max}$	3D maximum lift coeffcient
C_L	3D lift coeffcient
C_l	2D lift coeffcient
Re	Reynolds number
α_i	Induced AoA
β	Sweep angle
Δt	Laser Pulse separation time
δt	Laser pulse duration
δ_z	Focal depth
ϵ_{wb}	Correction factor of the wake blockage
Γ_0	Mean circulation along the wing
Γ_1	Amplitude of circulation variation along the wing
Γ_{straight}	Spanwise circulation distribution of a straight wing
Γ_{tubercle}	Spanwise circulation distribution of a tubercled wing
Λ	Allen and Vincenti shape factor
λ_{2D}	Glauert shape factor
ω_x	Mean streamwise vorticity
$\overline{v}$	Mean spanwise velocity
$\overline{w}$	Mean wall-normal velocity
$\vec{l}$	Trajectory vector of the integration path
$\vec{V}_{2D}$	Mean velocity vector on the plane
$\vec{V}_{3D}$	Mean velocity vector in the space
A^*	Nondimensionalized tubercle amplitude
c_0	Chord length of the baseline airfoil
d_{diff}	Particle diameter variation caused by diffraction effect
d_τ	Particle diameter in the image
d_i	Image distance

d_o	Object distance
d_p	Particle actual diameter
f	Focal length
$f_{\#}$	Focal ratio
H	Object dimension
h	Image dimension
L	SC size
l_{pixel}	Pixel pitch
M	Magnification factor
N_{pixel}	Dimension of the interrogation window in pixel
T	Temporal resolution of PIV measurements
t	Airfoil thickness
u	Streamwise velocity
U_∞	Inflow velocity
v	Spanwise velocity
w	Wall-normal velocity

1
Introduction

Biomimetics is of great interest to engineers as bio-inspired structures can provide promising solutions for engineering problems from a perspective of nature. In recent years, airfoils with such designs have gained increasing attention for their exceptional aerodynamic performances. Humpback whales, among other cetaceans, are unique for their pectoral flippers whose leading edge has tubercles; those protuberances are believed to enhance the maneuverability of the whales during feeding. A better understanding of the related flow control mechanisms would be beneficial for wing design in the future. In this chapter, a brief introduction to the humpback whale will be given in Section 1.1, followed by the literature review on the bio-inspired tubercled wing in Section 1.2. Then, the research objectives and research questions are explained in Section 1.3. In the end, the outline of the thesis is illustrated in Section 1.4.

1.1. Humpback whale *(Megaptera novaeangliae)*

Humpback whales can be found in oceans and seas around the world and are one of the most-observed and well-studied whale species [1]. The reason why this species is familiar to humans could be that they are active near the sea surface; they can leap clear of the sea and slap to make large visible sea sprays, which makes them appealing to whale watchers [2]. Those whales have a special hump on the back, which is the origin of their name. In addition, they feature a distinctive spindle-shaped body and paired long pectoral fins with irregularly located protuberances along their leading edges, which can be seen in Figure 1.1. In fact, the Latin name of the species, *Megaptera novaeangliae*, translates directly into 'giant winged New England', which can be inferred that the humpback whale was first seen near New England and impressed then whalers with its large pectoral fins [2]. It is thus not difficult to imagine that other body parts should be compatible with the fins in size: an adult humpback whale can be 14-17 m in length and its flippers are even larger than those of blue whales [3, 4]. The adult humpback whale can weigh up to 40 tons [5]. To maintain such a huge body, the humpback whale has to spend around 22 hours, which is about 92% time of the day, foraging for 2-2.5 tons of krill and other small fish as food in the summer feeding season. They are migratory animals and do not eat in the winter reproduction period [6].

Figure 1.1: Photograph of the humpback whale breaching. Note the tubercles along the front edge of the pectoral fins (image credit: Whit Welles [5]).

One intriguing feeding strategy used by humpback whales is 'bubble-net feeding'. The strategy normally requires a group of humpback whales to act cooperatively; they swim around a school of prey in an upward spiral while exhaling air out of their blowholes to create a 'bubble curtain'. This will form a net over time as shown in Figure 1.2, confining the prey in a narrow tube in the center so that the whales can lunge from the bottom to swallow the prey efficiently. The net size created is in the range of 3-30 m in diameter [7], which is surprisingly short compared to the body length of the whale.

The agility of the whales suggests that certain structures of their body can serve as prototypes for biomimetic designs in vehicles moving in fluids. It is widely believed that this sharp-turning ability can be attributed to the tubercles along the front edge of pectoral fins [4]. The presence of the tubercles can modify the flow field around the pectoral fins and thus increase their hydrodynamic efficiency. In short, the winglike tubercled fins facilitate the high lift generation and hence provide the required centripetal force to allow a sharp turning [8, 9, 10]. Although other structures, such as flukes of the tail, also contribute collectively to improve the performance, the tubercles are regarded as the main underlying factor and therefore this phenomenon is called the 'tubercle effect'.

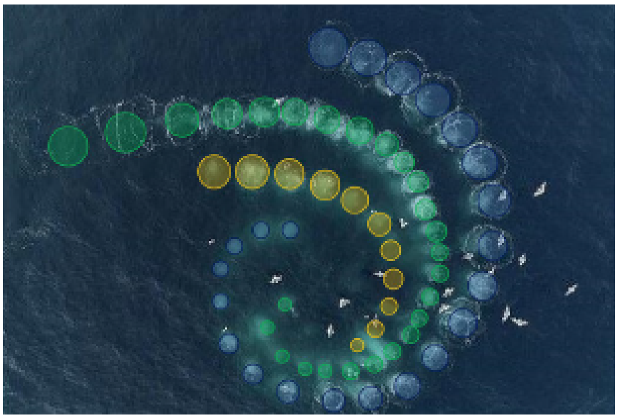

Figure 1.2: Photograph of the bubble-net spiral; the circles of different colors represent the bubbles created by different whales over time (image credit: Moscato et al., 2022 [11]).

1.2. Tubercled wing

Pioneering studies on the 'tubercle effect' have a strong biological background and the analyses are relatively qualitative. This encourages academia and industries focusing on fluid dynamics to investigate the phenomenon with more quantitative approaches, such as theoretical analyses, experiments, and numerical simulations. The purpose of this section is to provide a review of the progress achieved so far.

1.2.1. Performance and geometry effect

Although the tubercled pectoral fins had been believed to improve the maneuverability of humpback whales, it was not clear whether they could outperform ordinary ones. This doubt was solved by a series of wind tunnel experiments on a 3D fin model resembling the pectoral fin of a humpback whale [12]. The results showed that performance was indeed enhanced; the maximum lift coefficient $C_{L,max}$ increased up to 0.95 from 0.875, the stall AoA was delayed by about 40%, and the post-stall drag coefficient C_D was reduced, which are favorable for a wing working at a high AoA [12]. However, the improvement was not found to be applicable to any airfoil with LE tubercles. To elucidate the potential causes, two types of modified wings were used in wind tunnel tests; one was of full-span and the other was semi-span with the latter possessing a shape similar to the fin [13]. The motivation was to examine the 2D and 3D effects in this scenario. It was found that the 3D effect played a significant role in the performance improvement; the full-span (i.e., 2D case) wing experienced a performance deterioration in both pre- and post-stall regions with stall occurring earlier and the drag coefficient C_d becoming larger compared to the baseline [13]. The semi-span wing, in contrast, performed similarly to that reported in the previous research [12]. The only merit for the full-span wing is a softer post-stall behavior in which the lift coefficient decreases gradually rather than dropping drastically. The Re effect is also involved due to the variant chord length along the span and considered to be a factor contributing to the difference [13, 14].

Although the application of tubercles on a full-span wing does not enhance aerodynamic performance as much as for the semi-span one, the simple geometry makes it ideal as a baseline to investigate the effects of underlying factors. A comprehensive study was conducted to investigate the influences of the tubercle geometry by changing the amplitude A, wavelength λ, and LE curvature of tubercles along the LE of NACA 63(4)-021 airfoil, which is similar to the cross-section of humpback whale fin [15]. It was concluded that the amplitude dominates the wing performance over other factors; a large amplitude results in an early stall and reduced $C_{l,max}$, while a small amplitude allows the wing to reach a higher $C_{l,max}$ and to have a softer stall behavior and is thus preferred. Similar results regarding A were obtained in other research [16]. It has been postulated that an optimal λ might exist for a certain A. Thus the parameter $\frac{A}{\lambda}$, which is the ratio between the amplitude and the wavelength has been proposed as a non-dimensional similarity parameter for the effect of tubercle geometry [16]. Therefore, despite the dominating effect of amplitude, the wavelength should also be considered in design [17].

1.2.2. Engineering applications

Since its effectiveness was validated, the tubercled wing has emerged as a promising candidate to improve the efficiency of artificial devices in various industries. Instead of adopting the exact shape of the front edge of the fins, engineers choose to modify the edge into a simple sinusoidal shape for the convenience of manufacturing. Currently, tubercled wings are primarily used in the renewable energy industry to improve energy conversion efficiency.

Renewable energy covers a wide range of energy sources that can be replenished on a relatively short timescale compared to the human lifetime [18]. The section focuses exclusively on wind energy, tidal energy, and nuclear energy, as the tubercled wing can be utilized in rotating machinery which is commonly employed in these three industries. One of the complexities of blade design for rotating machinery is that the blades normally work under inflow conditions where an extra velocity component due to rotating motion should be considered. This extra velocity varies radially which makes the inflow condition more difficult to analyze. The strong unsteadiness and interaction of the wake pose other challenges for control and operation.

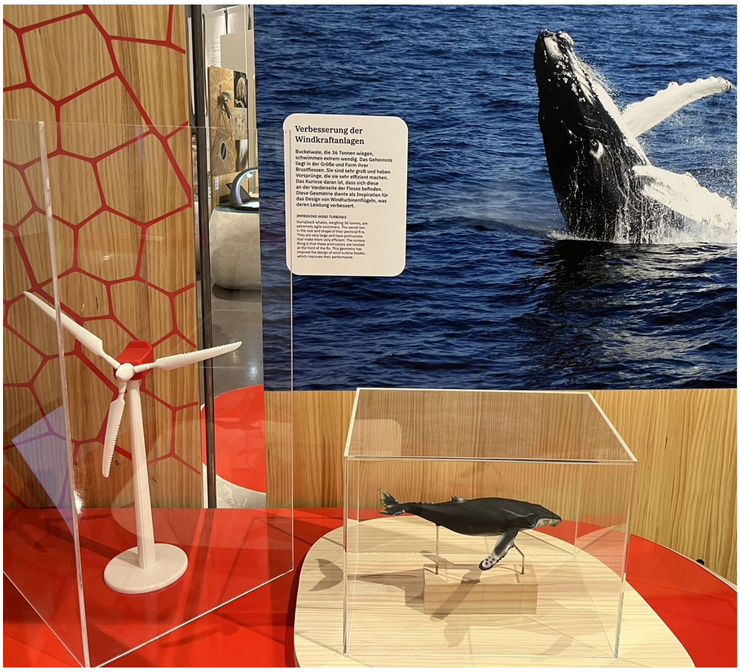

Figure 1.3: Photograph of the wind turbine with a modified trailing edge (TE) inspired by humpback whale tubercled fins in a biomimicry exhibition at the Vienna Museum of Science and Technology.

In the wind energy sector, the tubercled wing has already shown its value in power generation. A field test on the 2-blade turbine with tubercled blades designed by the WhalePower Corporation showed that electrical output outperformed that of an unmodified turbine [19]. It was found that the wind turbine with the LE tubercles has an increased lift-to-drag ratio, or aerodynamic efficiency, in the post-stall region, which can compensate for the negative influences of the blade's rough surface [20]. Additionally, the load fluctuation caused by the vortex shedding was reduced, which is beneficial for stabilizing the turbine output [20]. The LE tubercles can also reduce the hysteresis effect of a dynamic pitching blade and thus contribute to the control of aerodynamic load [21]. In addition to modifying the LE, there is the alternative of placing tubercles along the TE as shown in Figure 1.3. This modification was reported to be suitable for wind turbines operating in a turbulent inflow condition. The retrofitted TE can inhibit the turbulence level at the TE, and stabilize and improve the wind turbine output in the post-stall region [22].

Similar conclusions of enhanced conversion performance are obtained in the tidal energy and nuclear energy sectors. Tidal turbines with LE tubercled blades were reported to have higher power output when the tip-speed ratio (TSR) is low [23, 24]. The TSR is defined as the ratio between the rotational speed and the axial speed felt at a specific radial location along the blade. The lower the TSR, the higher the local AoA should be. Therefore, tidal turbine blades with tubercles operate more efficiently in post-stall regions when the inflow AoA is high. The output power of a nuclear steam turbine working at the low-mass rate was also improved by adopting the wavy LE blades, which again demonstrates the advantage of the tubercled blade [25].

1.2.3. Flow control mechanisms

Despite the continuously growing application of tubercled wings in industry, the flow control mechanisms of LE tubercles remain unclear, and a consensus is far from being reached. The most widely recognized theory is that the tubercles are analogous to vortex generators, which can generate streamwise vortices along the span [9, 14, 16, 26, 27]. Freestream momentum is introduced towards the wing surface by the turbulent mixing effect, which re-energizes the flow and thus delays separation. A similar conclusion was obtained but only for tubercles with small amplitudes [28]. This conclusion could be justified by the argument that tubercles cannot be modeled as vortex generators as their dimensions are normally much larger than the boundary thickness [29]. Instead, the induced AoA at each wing section was modified by the existence of streamwise vortices which the delayed separation could be attributed to [29]. Wings with tubercles of large amplitude were assumed to function similarly to delta wings [3, 30, 31], which can generate high lift at high AoA on the merit of vortex lift effect [32]. Therefore, the underlying flow control mechanisms might be dependent on the tubercle geometry [33]. In both experimental and numerical results, the stall was found to occur first at tubercle troughs (i.e., sections with shortest chord lengths). Based on this observation, a mechanism involving secondary flow caused by a spanwise pressure gradient was proposed. The counter-rotating vortex pair arising at a valley section can induce early separation of the flow behind the valley [34, 35]. Another theory conceptualized the tubercle as a wing fence. The compartmentalization effect resulting from the attached flow behind the peak sections is reminiscent of the wing fence, which can inhibit the spanwise extension of flow separation [14, 36]. All assumptions above are based on the presence of streamwise counter-rotating vortices; the real mechanism might involve all of the opinions discussed above [26]. Further studies on the pattern and evolution of the streamwise vortices are needed to better understand the underlying control mechanisms of tubercles.

1.2.4. Similarity to a delta wing

Among the above mechanisms, a competitive argument is taking a tubercle as a small delta wing since the flow fields around both structures are similar which can be seen in Figure 1.4. This similarity can be instrumental in understanding the tubercle effect from the perspective of a delta wing, especially on the vortex formation mechanism along the LE. Both tubercles and delta wings have swept LE where flow rolls over on the suction side, resulting in a vortex. The vortex accumulated along the chord and the vorticity calculated on a streamwise plane at the TE location would be highest. Therefore, it would be appealing to evaluate the vorticity of a delta wing at the TE location and compare it with that of a tubercle at the first streamwise plane.

Hemsch and Luckring propose a semi-empirical model of vortex strength estimation for a delta wing [39]. The model gives the accumulated circulation on a plane at the TE with inputs of AoA and the sweep angle β. The formula of non-dimensionalized circulation is given below:

$$\frac{\Gamma}{c_0 U_\infty} = \frac{9.2 A^* \cos(\alpha) \tan^{1.2}(\alpha)}{\tan^{0.8}(\beta)}, \tag{1.1}$$

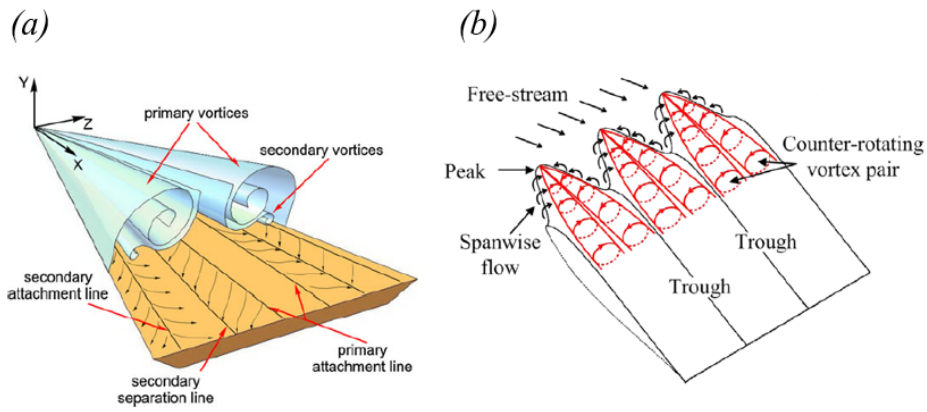

Figure 1.4: Schematics of flow patterns over (a) a delta wing (image credit: Sidorenko et al., 2013 [37]); (b) LE tubercles (image credit: Wei et al., 2015 [38]).

where A^* is the amplitude non-dimensionalized by the mean chord length c_0, and α is the AoA in radians. $\tan(\beta)$ is defined as $\frac{2A}{\lambda/2} = \frac{4A}{\lambda}$. The 9.2 is an empirical value estimated from numerical results [39]. Traub puts forward another empirical model to predict the LEV circulation of a delta wing based on the Kutta-Joukowski theorem [40]. The spanwise variation of lift is represented by shed vortices traveling downstream. The strength of accumulated streamwise shed vortices at the TE location is regarded as the LEV circulation and is modeled as:

$$\frac{\Gamma}{c_0 U_\infty} = \frac{2.212 A^* \pi \sin(\alpha)}{\tan^{0.8}(\beta)}, \tag{1.2}$$

which has a similar form to that of Hemsch and Luckring.

Although tubercles and delta wings have similar flow patterns, a tubercled wing functions differently from a delta wing. The vortex lift effect is a significant feature of the delta wing, while applying this concept to a tubercled wing is problematic, as the tubercle operates under conditions that are very different from those of a delta wing [26]. The vortices generated along the swept LE would have downwash and upwash effects at the neighboring locations while only the former effect affects the performance of a delta wing as there are no other delta wings nearby. Therefore, even if vortex lift exists for a tubercle, the overall performance enhancement cannot be attributed to it. The rolling motion of vortices could lead to performance deterioration at other locations, making the net enhancement negligible.

1.2.5. Flow pattern over the suction side

Alongside investigations of the general governing mechanisms of the flow around a tubercled airfoil, particular attention has been put on the complicated flow phenomena on the suction side at both pre- and post-stall AoAs.

Pre-stall case

In the Re range where the tubercled wing normally operates, a laminar separation bubble (LSB) is commonly observed. The LSR is a flow structure that can be found on the suction side of a low-speed wing at a pre-stall AoA. Its formation and bursting greatly change the pressure distribution and thus affect the overall performance of the wing. The formation of a LSR is primarily determined by Re and the airfoil geometry (i.e., pressure distribution). When the Re is moderate (i.e., at the order of magnitude of $10^4 - 10^5$ [41]) and the pressure gradient is not strong, a local separation region occurs on the upper surface of the airfoil as shown in Figure 1.6. Before the separation point, the boundary layer (BL) is laminar. At the separation point, there is an inflection point in the local velocity profile, which indicates a disturbance that evolves downstream and triggers transition. However, the transition is damped at the inflection point as it is near the wall. After separation, the BL remains laminar for some distance and is gradually lifted above

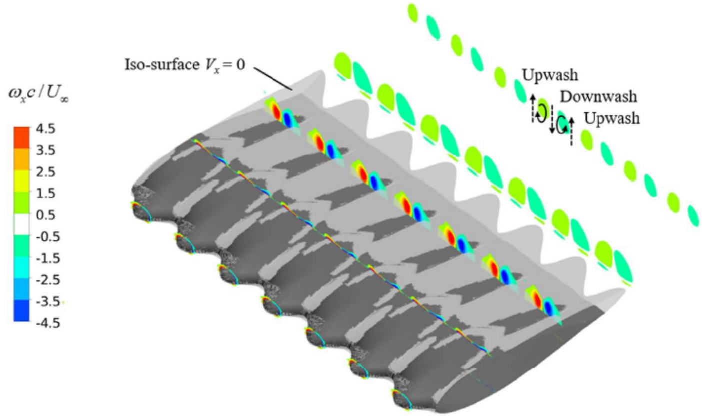

Figure 1.5: Pre-stall flow pattern of a tubercled wing (image credit: Cai el al, 2017 [41]).

the 'dead water zone' located at the front part of the bubble, in which the fluid elements are almost still. The recirculating motion at the rear part of the bubble is caused by the existence of the free shear layer, which is the result of the inflection point evolving downstream. The downstream inflection point is far enough away from the wall and promotes transition. The mechanism for vorticity generation in the bubble is ascribed to the Kelvin-Helmohotz instability, which is inherently an inviscid process triggered by the difference in velocity of the two adjacent layers of flow. At the peak of the bubble, transition occurs and the BL becomes turbulent, allowing it to gain more momentum from the energetic external flow which enhances the BL's ability to withstand a stronger adverse streamwise pressure gradient. The BL reattaches to the wall because the pressure requirement for being an attached flow is satisfied due to the turbulent mixing [42]. Since a turbulent BL is developed after reattachment while the external flow is not affected, the LSB could be regarded as a process to facilitate transition [41]. Similarly, the LSB can also be interpreted as a modification of the airfoil to prevent flow separation when the adverse pressure gradient is too high. Except for the blockage effect, the existence of the LSB complicates the vortex system as vortices can be generated inside an LSB and travel downstream like trailing vortices. This phenomenon is investigated in a previous study using the DNS technique and the results are given in Figure 1.7.

The alternating regions of upwash and downwash along the wing's span are a primary feature of a tubercled wing. This feature greatly changes local AoAs and thus affects the formation of LSBs. The leading edge vortices (LEVs) generated at the LE tubercles interact with the LSB, which results in a more complicated flow pattern on the suction side as can be seen in Figure 1.5. After generation at the LE, LEVs are in the form of thin sheets and close to the wing surface. As they travel downstream, they are lifted by separated regions and deform into a rounded shape. Secondary vorticity is generated underneath the primary vorticity region and has an opposite sign to the primary one, as seen in the wake region. LSBs first occur at trough locations due to high local AoAs and then extend to the downstream peak location. Flow reattachment is found to occur for both trough and peak locations, but the flow at trough locations separates soon and forms a large separation area. The flow at peak locations, in contrast, only separates near the TE.

Unlike a straight wing, where the spanwise pressure distribution is relatively uniform, the distribution of LSB on a tubercled wing is not spanwise constant. This phenomenon can be explained by the fact that the streamwise pressure gradient experienced by fluid elements is different from one location to another along the span. For example, the distance between the location of maximum thickness and the LE at a trough location would be shorter than that at a peak location, which means that the pressure peak is higher. Besides, the induced velocity at trough locations is upward and will increase the local AoA, which further strengthens the pressure peak. Therefore, the LSB bubble emerges earlier near the trough locations and later near the peak locations along the chord.

Depending on the inflow condition and tubercle geometry, the LSB pattern can be either wavy or discontinuous [34, 43, 44]. The pattern can be complex as shown in Figure 1.8. It can be concluded that the tubercle geometry (i.e., $A, \lambda, \frac{A}{\lambda}$) plays a significant part in the flow patterns [17]. Since the LEV is directly affected by the tubercle geometry, research on the interaction between the LEV and the LSB could provide

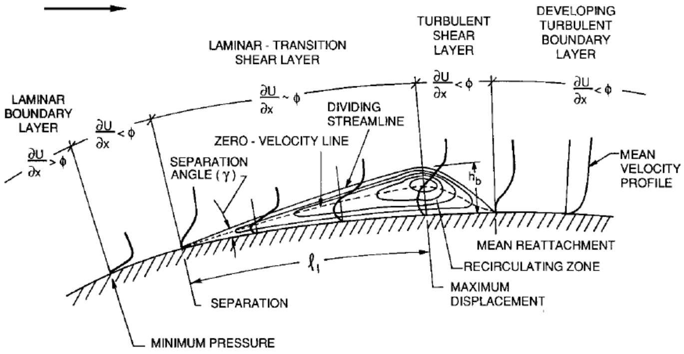

Figure 1.6: The side view of a laminar separation bubble (image credit: Gad el hak, 2001 [41]).

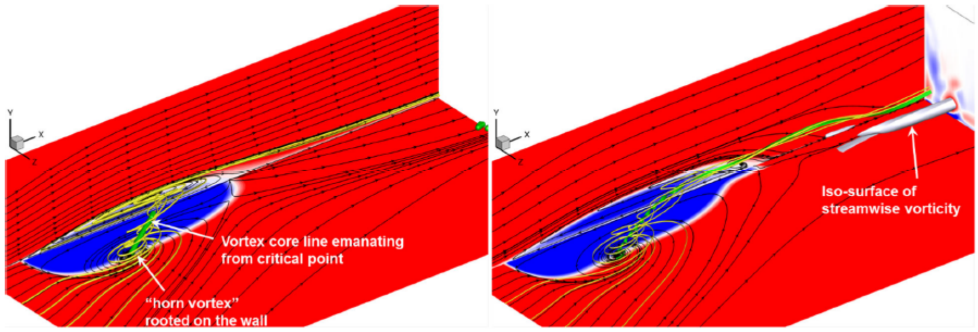

Figure 1.7: DNS results of a vortex filament generated inside an LSB; the blue region represents the reverse flow region inside an LSB (image credit: Hosseinverdi et al., 2015 [45]).

insightful information on pre-stall flow conditions.

Post-stall case
The flow pattern in a high AoA region is believed to be relevant for improved post-stall performance of a tubercled wing [46].

Flow evolution has been investigated in previous studies to provide detailed and precise descriptions on flow structures. The streamwise vorticity is used as an indicator to study these flow structures. In Figure 1.9, the result at several cross-flow planes is demonstrated. Although the AoA is high, the LEVs are still close to the wall after generation. Then, the LEVs located at separated regions are lifted and become separated shear layers. These layers will induce sublayers underneath, and the interaction between them leads to the formation of a strong rolled-up vortex core next to a separated region. This structure persists until it gradually decays further downstream. The flow structures located at separated regions are demonstrated in Figure 1.10. Complicated vorticity patterns can be observed at trough locations and their evolution is represented on several cross-flow planes. It is found that the interaction between the LEV, LSB, and induced secondary vortices is important in the evolution. The flow structures can also be visualized by using the turbulent kinetic energy which represents the velocity fluctuation. In Figure 1.11, strong shear layers are captured due to their high unsteadiness.

A notable flow pattern of interest is the stall cell (SC), which occurs for airfoils near or in the post-stall region [48, 49]. The stall cells are 'mushroom-like' mean flow structures [50, 51], which are believed to be the result of impingement of separated TE vortices on the wing surface [52]. In Figure 1.12 (a), the evolution of TE vortex pairs and the formation of a SC is illustrated. Two vortices near the TE tend to interact with each other, resulting in a wavy deformation of the vortex filaments. The deformed filament will impinge on the wing surface once the disturbance is large enough and SCs form. The existence of a SC greatly modifies the surface shear stress distribution, the SC patterns can be visualized by the oil flow visualization (OJF) technique. The oil painted on the wing is fluorescent and accumulates at low-shear-stress locations on the

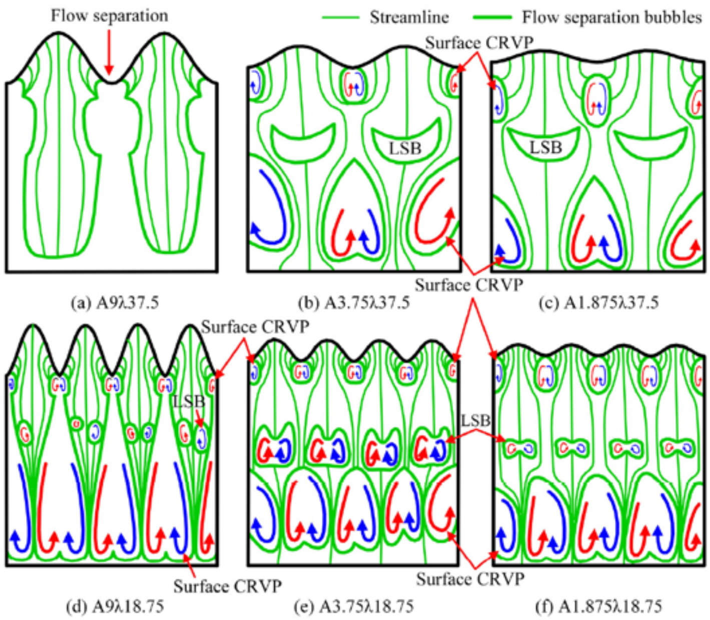

Figure 1.8: Schematics of flow patterns on tubercled wings at a pre-stall AoA (image credit: Wei et al., 2019 [17]).

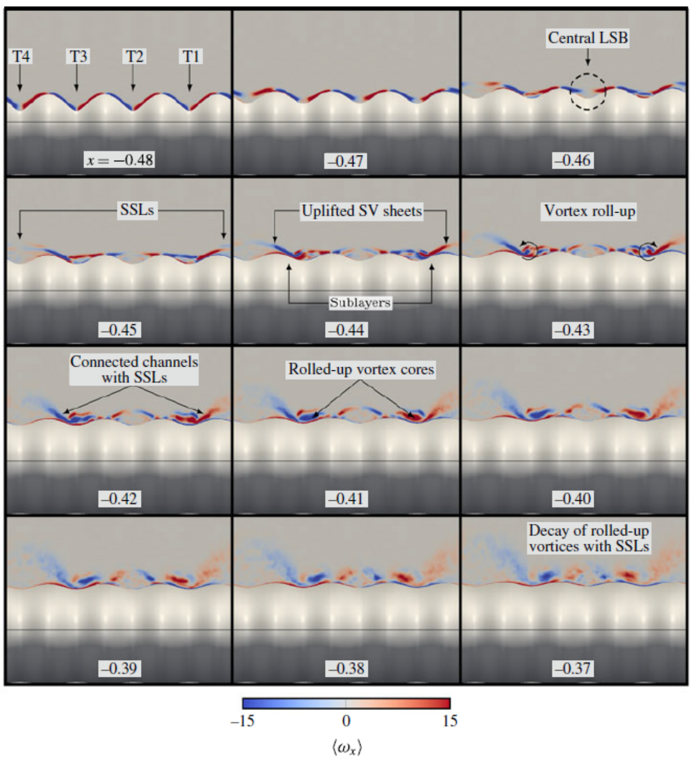

Figure 1.9: Evolution of streamwise vorticity at different cross-planes of a tubercled wing (image credit: Pérez-Torró and Kim, 2017 [47]).

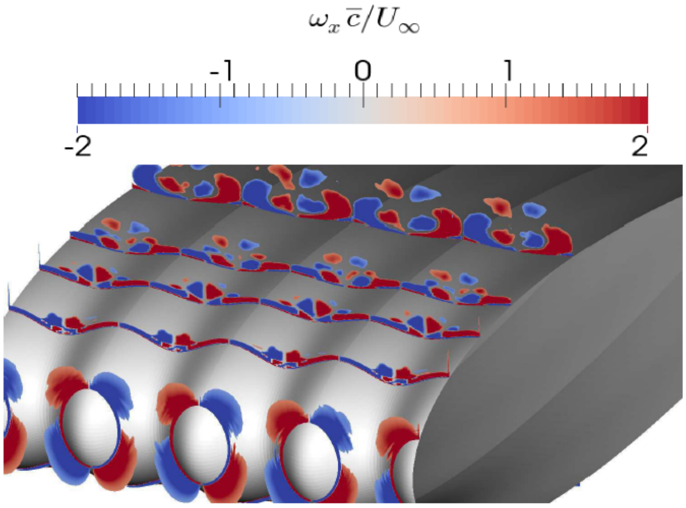

Figure 1.10: Slices colored by time-averaged streamwise vorticity (image credit: Skillen et al, 2014 [35]).

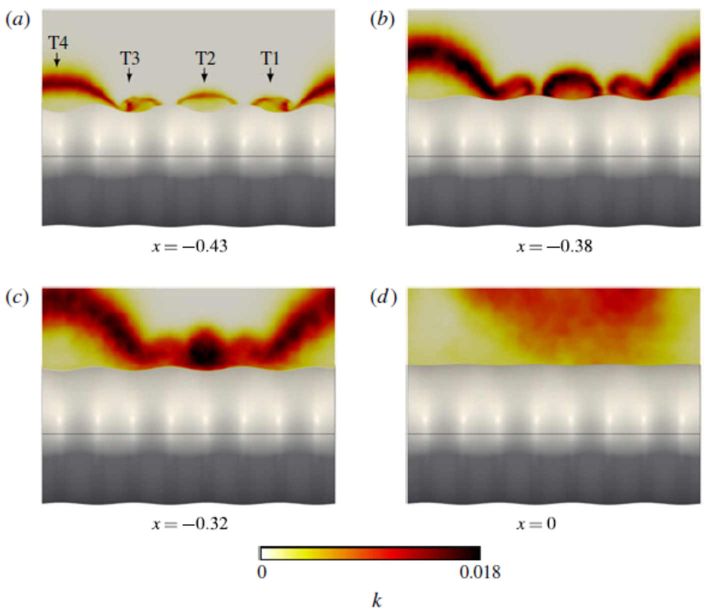

Figure 1.11: Evolution of turbulent kinetic energy at different cross-planes of a tubercled wing (image credit: Pérez-Torró and Kim, 2017 [47]).

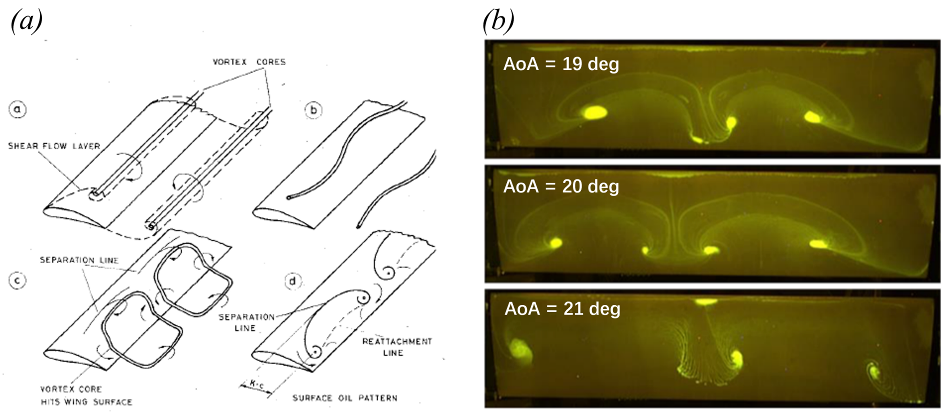

Figure 1.12: (a) Schematic of the vortex interaction with the wing surface and the resulting cellular patterns in the separated flow over rectangular wings (image credit: Weihs and Katz, 1982, [52]); (b) Stall cell patterns visualized by the OJF technique on the surface of a wing in the post-stall region (image credit: Dell'Orso and Amitay, 2018 [55]).

Table 1.1: Summary of SC spacing in previous studies.

Reference	A/c_0	λ/c_0	$Re_{c_0} \times 10^5$	AoA [°]	SC spacing
Custodio [30]	0.12	0.5	0.15	12, 18, 24	2λ
Dropkin et al. [56]	0.12	0.5	1.8	18 24	2λ 3λ
Cai et al. [31]	0.12	0.5	1.8	15 24	2λ 2λ
Zhao et al. [57]	0.12	0.5	2	18, 21, 23	2λ
Cai et al. [46]	0.0476	0.2381	1.8	16 24	4-6λ 4-8λ

surface. Therefore, the shear stress pattern can be indirectly visualized by the thickness distribution of the oil, which is quantifiable by its brightness under specific illumination conditions as shown in Figure 1.12 (b), where a bistable pattern can be observed. However, the number of stall cells on a wing surface partially depends on the airfoil stall characteristics (e.g., post-stall lift curve slope) [53], and the wing geometry (e.g., aspect ratio) [54]. The scenario becomes more intricate for a tubercled wing.

The spanwise periodicity of stall cells of an airfoil with LE tubercles was first visualized by using dye and in water tunnel tests [30]. In Figure 1.13 (a), A bi-periodic stall cell pattern, which is the alternating appearance of the attached flow and separated flow at trough regions was observed. This was reproduced in the later studies [23, 31]. However, this bi-periodicity does not hold for all cases as seen in Figure 1.13 (b). A tri-periodic pattern was found at AoA $= 24°$, by applying 6 tubercles along the LE [56]. In the studies where the bi-periodicity was reported, however, only 4 tubercles were placed at the LE [30, 31]. The understanding of this aspect was furthered by using different numbers of protuberances. The stall cell distribution was found to be either periodic or aperiodic [46]. The interval (or cell size) between two neighboring stall regions was found to vary from 4 to 8 times the wavelength of tubercles, depending on both the AoA and the tubercle number [46]. So far, the convincing mechanism for the patterns remains a research challenge.

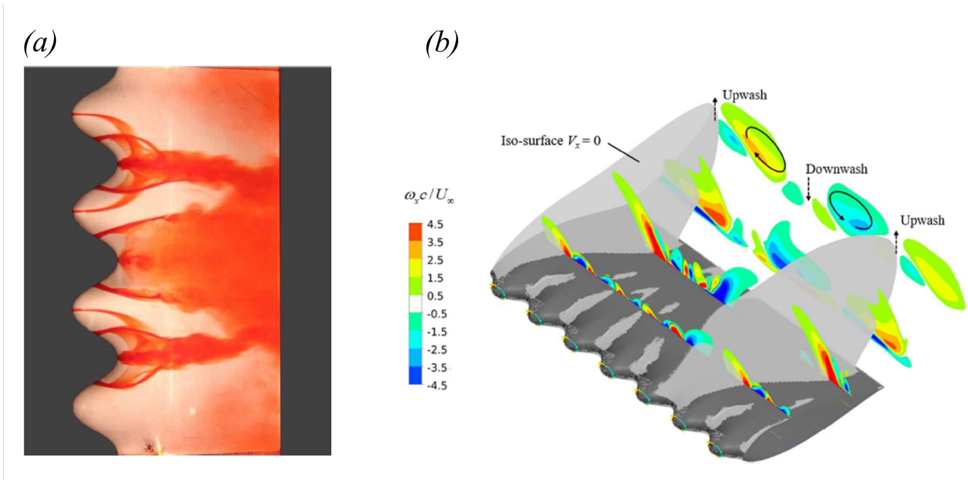

Figure 1.13: (a) Bi-periodic SC pattern visualized by the dye flow visualized technique (image credit: Custodio, 2007, [30]); (b) Stall cell pattern visualized by the iso-surface $V_x = 0$; note the interaction between the LEVs and the SCs (image credit: Cai et al., 2017 [46]).

1.2.6. Theoretical modeling approaches

Accurate predictions of flow patterns and their evolution are necessary to evaluate the pre- and post-stall performances of the vehicles equipped with tubercled wings. In addition to experimental and CFD approaches, theoretical modeling could also be used for this purpose. Van Nierop et al. developed an analytical aerodynamic model to explain the increased performance and concluded that the tubercle wavelength did not have much effect on the stall delay, which agreed with previous experimental results [29]. Linear stability analysis was used by Owen and Frendi to investigate the relation between critical Re and tubercle geometry [58]. Although both works are not directly related to the SC, they shed some light on predicting the SC pattern of a tubercled wing in a theoretical way. An image vortex method was used to empirically estimate the SC number based on aspect ratio [52]. As previously discussed, the impingement of the TE vortex on the wing surface is the cause of the SC. This process has been modeled by assuming a reflected image vortex of the TE vortex above the wing, mirrored around the upper surface while disregarding the downstream wake vortex as illustrated in Figure 1.15. This is intended to capture the flow characteristics of the suction-side [52]. The quantitative relation between the distance of two vortex cores and the cell size can be estimated from Crow's vortex-pair model shown in Figure 1.15 (b) [59], and the derivation of the model is given in Appendix C.

Lifting line theory (LLT) could be another candidate for theoretical modeling because of its simplicity and versatility. The method was developed primarily by Ludwig Prandtl in the early 20th century, and it is an important theory in the field of incompressible aerodynamics. It provides a simplified yet effective way to predict the lift distribution along the span of a wing with the 3D effect included. In a typical LLT model, the finite wing is modeled by a series of horseshoe vortices. One horseshoe vortex includes one bound vortex located at the wing location and two trailing vortices. The bound vortex is also called the 'lifting line' as it represents the lift generated by the wing. Trailing vortices of the same circulation as the bound vortex, are used to model the downwash or upwash effect on the wing. The spanwise distribution of circulation can be represented by superimposing those horseshoe vortices with different strengths and bound vortex lengths as shown in Figure 1.14.

In practice, a linear system of equations can be developed at pre-stall AoAs and the spanwise circulation distribution can be obtained by solving it. If the AoA exceeds the stall AoA or the spanwise chord distribution is not uniform, the system of equations becomes non-linear, and an iterative approach is required. Anderson developed a nonlinear lifting line theory (NLLT) based on the iteration method to evaluate the performance of a wing with drooped LE along the outboard part [60]. In the context of a tubercled wing, the NLLT can be easily adapted to account for the wavy chord length. This method has been utilized to calculate the spanwise distribution of the circulation for modified wings with a wavy distribution chord and twist AoA respectively up to AoA $= 19^\circ$ [61]. Instead of using the wing geometry, Gross et al. utilized LLT to model the stall cell pattern on an infinite wing and showed that the stall cell only existed when the lift curve slope

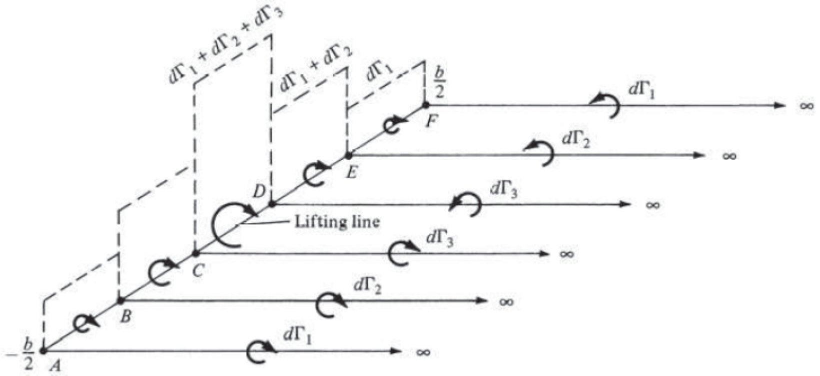

Figure 1.14: Superposition of a finite number of horseshoe vortices along the lifting line (image credit: Anderson, 2010 [64]).

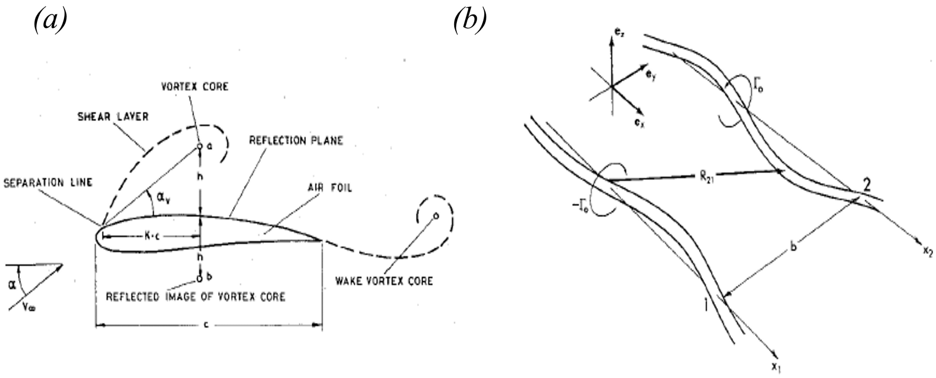

Figure 1.15: Schematics of (a) the vortex-wing model used to estimate the stall cell size (image credit: Weihs and Katz, 1982 [52]); (b) Schematic of the vortex pair model (image credit: Crow, 1970 [59]).

was negative [53]. The cell size could be estimated from the negative slope [53]. Rather than in a spatial domain, the theory can also be implemented in a spectral domain. The spectral version of the NLLT method was developed initially to prove that the multiple solutions found in the RANS results at post-stall AoAs were caused by the intrinsic non-linearity of the problem, rather than the turbulent models used. It has demonstrated its capability of capturing stall cell patterns [62]. This method was further extended to a lifting surface model [63]. This 3D model utilized the vortex-lattice method together with viscous 2D airfoil data to predict stall cells and showed better convergence performance [63]. To predict the stall cell size of a tubercled wing, however, existing methods need some modifications to take the distinctive flow characteristics into consideration.

1.3. Research objective and questions

By integrating knowledge from high-resolution experimental results, the details of characteristic structures and underlying mechanisms determining the flow evolution towards stall can be captured. The effectiveness of previous theoretical modeling approaches can be assessed by using this knowledge and an improved model could possibly be developed. In a word, the research objectives of the thesis can be summarized as:

> To further understand the influences of the LEV on tubercled wings in both pre- and post-stall regions at different streamwise planes as a function of amplitude and Re, and to evaluate the previous theoretical modeling approaches while proposing a new theoretical model based on the experimental results.

These objectives can be answered with the following four research questions:

1. **Can a tubercle be considered as a small delta wing?**
   LEVs emanating along the tubercled LE are a distinctive feature of tubercled wings and their generation mechanism is controversial. One competitive mechanism claims that the tubercle functions similarly as a small delta wing. The results obtained in this study could provide insightful information for the problem;
2. **How does the LEV affect flow patterns on the suction side in pre-stall regions?**
   The pre-stall flow patterns on the suction side are determined primarily by the LEV-LSB interaction. The resolution of previous experimental results, however, is not high enough to capture details of this interaction. High-resolution 2D particle image velocimetry (PIV) results will be used to further understand this aspect;
3. **What are the influences of amplitude and Re on stall cell patterns?**
   The stall cell patterns are very sensitive to inflow conditions (e.g., Re) and tubercle geometry. Hence, the influences of these factors should be investigated for phenomenon interpretation and model development;
4. **What are the limitations of current analytical approaches to model a tubercled wing?**
   Despite different physical mechanisms included, previous theoretical models demonstrate remarkable simplicity and provide insights into the main factors contributing to the problem. For a tubercled wing, however, the model should be more intricate as more flow features are involved.

1.4. Thesis outline

The experimental setup of the 2D PIV system is illustrated in Chapter 2, along with a discussion on parameter selection and velocity measurement procedures. Then, comprehensive flow field results of tubercled wings are provided and analyzed in Chapter 3. The effects of Re and tubercle amplitude are evaluated, and the mechanism of LEV formation is investigated quantitatively. In Chapter 4, the insights gained from the experimental study are applied to assess the capability of potential flow approaches in capturing the flow features of a tubercled wing, with the adaption procedures of the Crow's model introduced as well. Finally, conclusions and recommendations are given in Chapter 5 and Chapter 6, respectively.

Part I

Experimental Study

2

Experimental setup

2.1. Wing geometry

The wing used in this study had modified NACA 0021 profiles, as used in previous studies [16, 26, 34, 65]. Its popularity in the tubercled wing study can be explained by its application on wind turbine blades [65, 66]. There are at least 2 ways of modifying airfoil profiles for a tubercle wing. The simpler way is to scale the chordwise coordinates by the ratio between the desired chord length and the baseline chord length. The other is to retrofit the airfoil while preserving as many airfoil characteristics as possible. For example, the airfoil LE radius is a critical parameter affecting the airfoil performance [15], and it would be changed by using the former modification approach. Therefore, a nonlinear shearing transformation was applied in this work to modify the airfoil profiles. This transformation maintains the LE radius, location of maximum thickness, and the profile behind the maximum thickness location, while ensuring smooth transition at joint part [38]. The rest of the section introduces the coordinate system, modified airfoils, and the tubercled wing used in the experiments.

The coordinate system origin is defined at the nose of the baseline profile at AoA $= 0°$, with x, y, z standing for the streamwise, spanwise and wall-normal direction respectively. The $y = 0$ is at the right middle of the span where a trough is located. The z direction follows the rule of the right-hand system. The sinusoidal LE streamwise coordinate can be expressed as:

$$x_{LE} = A \sin\left(\frac{2\pi}{\lambda}y + \frac{\pi}{2}\right), \tag{2.1}$$

where A and λ represent the tubercle amplitude and wavelength respectively, which are defined in Figure 2.1. In this thesis work, two cases will be studied, which are $A = 0.05c_0$ and $A = 0.1c_0$ with $\lambda = 0.25c_0$. The corresponding wings are denoted as A05 and A10 in the rest of the thesis. The phase shift of tubercle distribution by $\frac{\pi}{2}$ enusres that x-axis is aligned with a trough location. The nonlinear shearing transformation follows the equations [38]:

$$x_1 = \begin{cases} x_0 + 0.5x_{LE}(1 + \cos(\pi x_0/0.3c_0)), & 0 \leq x_0 < 0.3c_0 \\ x_0, & x_0 \geq 0.3c_0 \end{cases}, \tag{2.2}$$

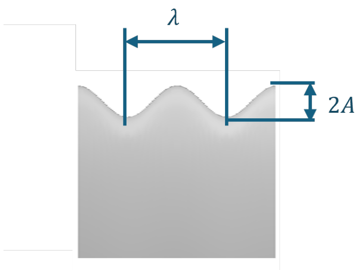

Figure 2.1: Definitions of the tubercle amplitude A and wavelength λ.

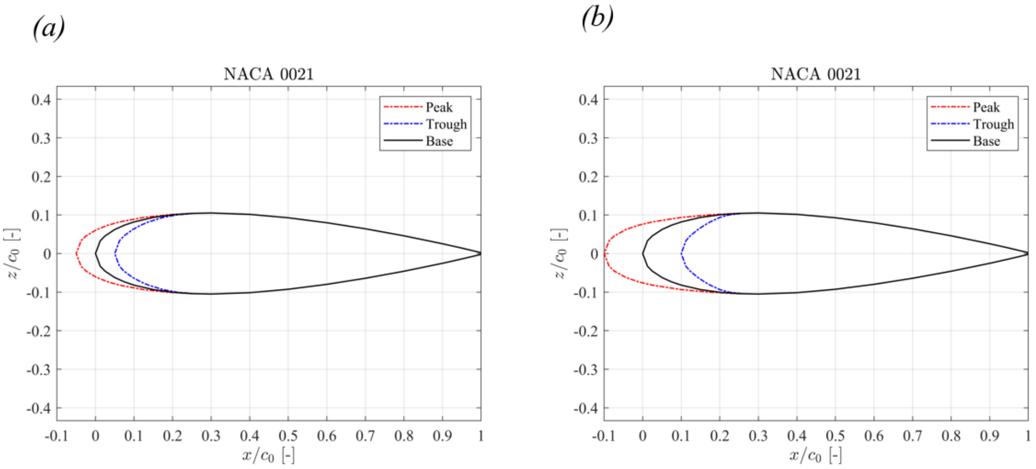

Figure 2.2: Airfoil profiles of baseline, peak, and trough: (a) $A = 0.05\,c_0$, (b) $A = 0.1\,c_0$.

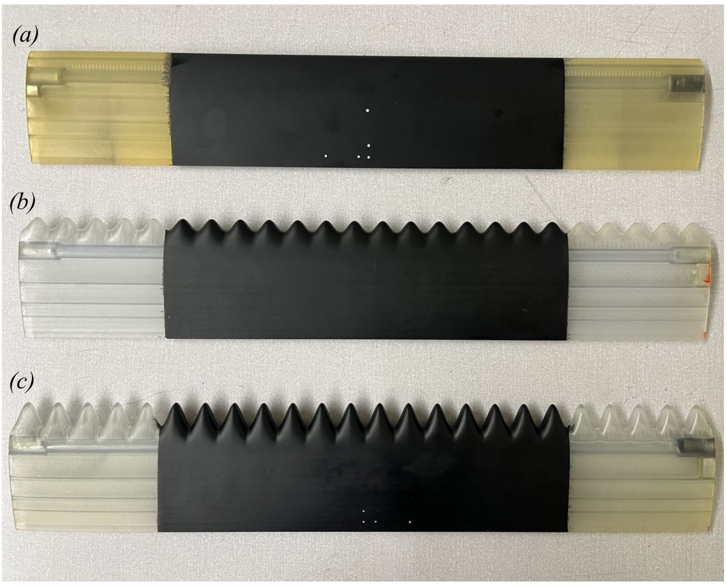

Figure 2.3: Top view of the wings: (a) baseline, (b) A05, (c) A10.

where x_0 and x_1 are the streamwise coordinates of the profile data points before and after transformation, and $0.3c_0$ represent the maximum thickness location of the airfoil. The results of modified airfoils at peak and trough locations of two cases are shown in Figure 2.2 in comparison with the baseline airfoil. It can be seen that the modified airfoils still have smooth streamlined shape, and the LE radius and the part behind the $0.3c_0$ are kept identical to the unmodified ones.

By applying this transformation along the span based on the LE coordinates, a tubercled wing can be obtained. Figure 2.3 shows the top view of unmodified and modified wings. The chord length c_0 of the baseline wing is 0.1 m, and the span is 0.6 m which corresponds to 24 LE tubercles. Tubercles in the middle of the span are painted black in order to avoid influences of lights reflected from and penetrating through the wing. The tubercles close to both ends are left without paint as the wall effect can be strong there, which would cause great uncertainty in measurements. In the tests, only black tubercles will be in the field of view (FOV).

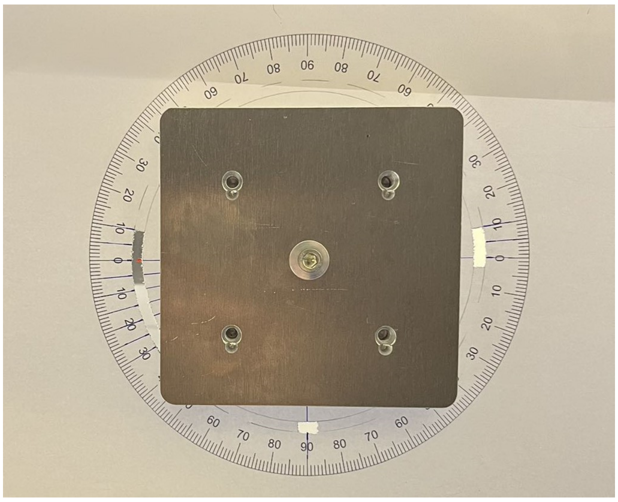

Figure 2.4: Photograph of the AoA mechanism. Note that the metal pad is used to fix the wing. Note that the red point pointing to 0 on the left is the TE of the wing model.

Table 2.1: Inflow velocity and corresponding Re

Velocity [m/s]	2	5	15
Re [-]	1.3×10^4	3.3×10^4	1.0×10^5

2.2. Wind tunnel

The tests are conducted in the W-Tunnel at the aerodynamics laboratory of TU Delft. The wind tunnel is an open jet wind tunnel with a square 0.6 m $\times$ 0.6 m exit, operating in the velocity range from 0 to 35 m/s. The wind tunnel functions as below: the flow is entrained and driven by the a centripetal fan into the open room with dimensions ($L \times W \times H$) 2.0 m $\times$ 1.5 m $\times$ 2.0 m, where tracer particles are added for PIV measurements [67]. After leaving the chamber, the flow will pass a contracted section get accelerated, and then leave from the exit. The inflow velocity in the test section is determined by the rotating velocity set in a computer on the control panel. By tuning the revolutions per minute (RPM) of the fan, the desired velocity can be obtained. The turbulence level of the wind tunnel depends on the inflow speed, and is estimated to be about 1% if the inflow velocity is 5 m/s.

In the experiments, the Re effect is investigated and three inflow velocities are used, which are summarized in Table 2.1.

2.3. AoA mechanism

There is no AoA mechanism that is suitable for the wing models used coming with the test section, and thus a AoA mechanism is customized. A photograph of the mechanism is shown in Figure 2.4. The mechanism is essentially a protractor printed on a paper, which is modified with 5 bolt holes to fit the metal pad seen in the photo. Besides, extra hollow parts are made on the paper in the range of AoA measured (i.e., 0 - 30°). In this way, the AoA of the wing can be read from the location of the red ”pointer” which is the airfoil’s rear part close to the TE. Since NACA 0021 airfoil is symmetrical, no extra calculation is needed. The uncertainties of this mechanism would only come from the way it is installed and the way the AoA value is read.

2.4. Imaging system

The imaging system consists of laser, camera (including lens), seeding generator and a customized laser fence. Their basic information together with the parameters will be briefly introduced below.

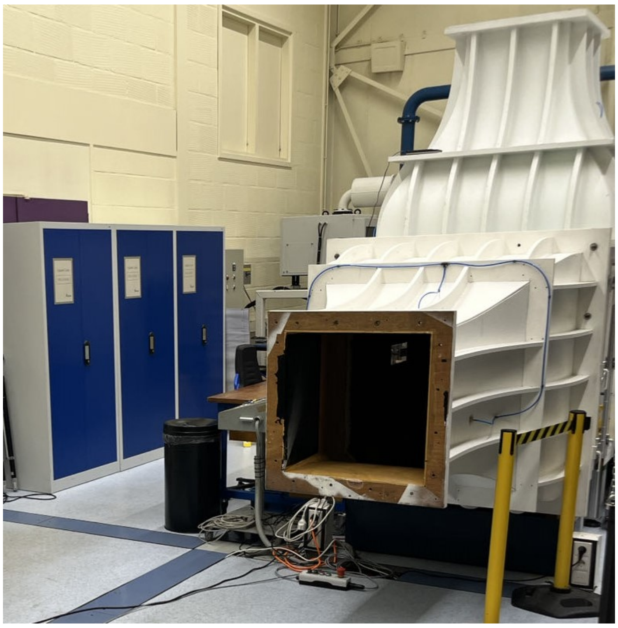

Figure 2.5: Photograph of the W-Tunnel at the aerodynamics laboratory, TU Delft.

Laser

The light source used in the PIV measurement is Quantel Evergreen 200 laser and the head of the laser is demonstrated in Figure 2.6 (a). As its name shows, the laser produces a monochromatic visible green light with its wavelength being 532 nm. The emitted laser beam is 6 mm in diameter and one laser pulse has 200 mJ energy at maximum, making the laser hazardous as the energy is concentrated in a narrow direction [67]. In PIV measurements, a pair of images with short time interval in between is required to calculate the velocity field. Therefore, the laser needs to emit twice in a short period of time. This is normally not possible for a single laser pulse emitter as the required power is too high. Hence, two laser emitters are be used in the laser head to ensure short repetition rate during measurements. The Quantel Evergreen 200 laser is a double pulsed Nd:YAG laser designed in this way which makes it possible to illuminate the area of interest twice at an attainable energy level while masking the time interval short. One laser pulse would last for 8 ns and the the laser can operate at a maximum frequency of 15 Hz, which means that at most 15 pairs of image can be created in one second and the maximum frequency can be accurately captured is 15 / 2 = 7.5 Hz according to the Nyquist sampling theorem.

The laser can be controlled by the Davis software, where the laser power, pulse separation time and data acquisition rate (i.e., repetition rate) can be set. This information would be first processed by the programmable time unit (PTU) connected to the computer and control signals are then sent to the laser and camera; The role of PTU is to synchronize laser illumination and camera shooting.

Camera

A specially-designed camera is used in the test, which can overcome the harsh conditions of low illumination and high unsteadiness in the PIV data acquisition and it can reach around the best quantum efficient operating at the laser light wavelength [69]. The camera sensor has the highest resolution of 2560 $\times$ 2160 pixels with a 6.5 μm pixel pitch. At the highest resolution, the acquisition rate of images is 50 fps, which means 25 pairs of images per second as the interframing time ($\approx$ 120 ns) is negligible [69]. This allows the camera shooting rate to be the same as the laser emitting rate as the former is higher than the latter. In the experiments, the camera is used together with the lens of which parameters are determined by the magnification factor M, FOV dimensions, and laser sheet thickness. A photograph of the camera with a connected lens is shown in Figure 2.6 (b).

(a) (b)

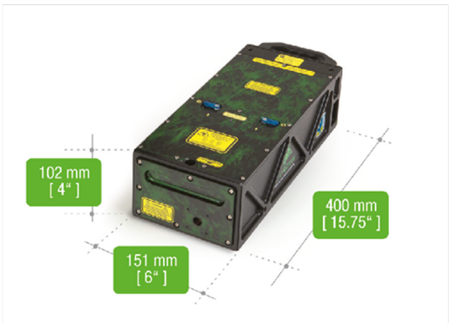

Figure 2.6: Photographs of (a) Quantel Evergreen 200 laser head with dimensions (image credit: Lumibird [68]); (b) LaVision's Imager sCMOS CLHS camera (image credit: LaVision GmbH [69]).

Seeding generator

The camera cannot image the fluid particles in the FOV if those elements do not reflect any visible light. To visualize the moving fluid elements in the illuminated region, the SAFEX fog generator is utilized to create tracers, which are small droplets from the SAFEX normal power mix fluid [67]. The tracers can form a non-toxic water-glycol based fog in the whole wind tunnel facility, and the flow inside can be visualized even by naked eyes.

The generator needs to be heated for about 5 minutes before use, allowing the fluid inside to reach the necessary high temperature to produce fog. The generator is operated via a remote control unit located on the control panel. By adjusting the unit's knob, the amount of tracers released can be regulated.

Light fence

Cross sections of the emitted laser beam are, without any manipulation, 6 mm in diameter. For the purpose of measurements on cross-flow planes, a rectangular cross section shape is preferred for as the whole plane can be illuminated by the laser sheet. A system of optical lenses is employed in front of the exit of emitted laser light to convert the beam into a laser sheet. This setup, however, still has the difficulty of controlling the laser sheet thickness, which is a important factor to determine the camera parameters. To avoid a varying laser sheet thickness in the tests, a customized laser light fence is designed and applied to the test section as shown in Figure 2.7. The principle of the fence is to control the laser sheet thickness by creating slots of the same streamwise dimension (i.e., 2 mm, and the reason of choosing this value is discussed in the next section) at different streamwise locations, which are x/c_0 = [0.15, 0.25, 0.45, 0.6, 0.8, 1.0] for a wing at AoA = 0°. To be more specific, the slot is first located at the nominal location and then extended 1 mm on both sides horizontally. After passing the fence, the laser sheet has the same thickness of 2 mm. Additionally, when measurements are being taken at a certain slot, other slots are covered with black tapes to ensure that only the desired plane is illuminated, this would avoid interference from other slots.

2.5. Parameters determination

The parameters of the laser and camera are determined based on the experimental purpose. In the PIV experiments, detailed flow patterns on streamwise planes and stall cell patterns along the span close to the LE are needed, which indicates two sets of parameters. In this section, three crucial PIV parameters, which are magnification factor M, laser sheet thickness H, and laser pulse separation time Δt, will be introduced at first along with the principles of determining their values. The parameter values used in the experiments are discussed and summarized at the end of this section.

Magnification factor M

One of the crucial parameters in PIV experiments is the magnification factor M, which is the ratio between the image dimension and the actual dimension of an object. It stands for to which extent the object in the physical space is scaled down to a pixel level. Since the pixel pitch is a constant, the larger the M, the

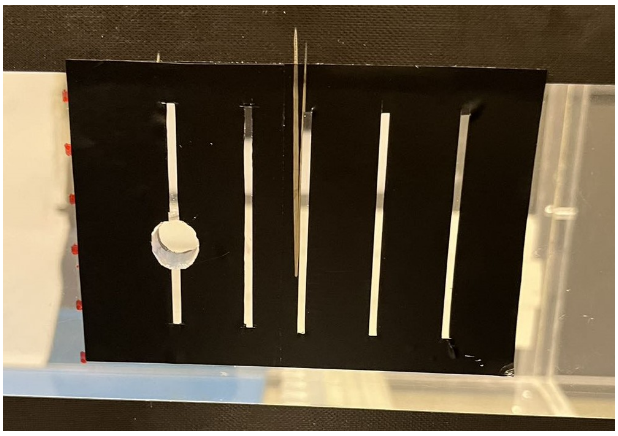

Figure 2.7: Photograph of the laser light fence on the external wall surface of the test section. Note that the slot at $x/c_0 = 0.15$ was added after this photo was taken and thus did not shown in this photo, and a hole is made at $x/c_0 = 0.25$ to accommodate the bolt fixing the wing model.

more similar the object and the pixel in dimension and the smaller the object in physical space.

Laser sheet thickness H

The estimation of laser sheet thickness is based on the requirement that camera focal depth, or depth of view, should be larger than the laser sheet thickness so that all particles illuminated in the laser sheet are in focus. To calculate the focal depth, we should first obtain the focal ratio $f_\#$, which is the ratio between the lens focal length and the camera aperture diameter. The parameter value can be estimated from the particle diameter d_τ in the image:

$$d_\tau = \sqrt{(M d_p)^2 + (d_{\text{diff}})^2}, \tag{2.3}$$

where the d_{diff} is the diameter variation caused by the diffraction effect, and it can be calculated from $d_{\text{diff}} = 2.44\lambda(1 + M) f_\#$. The average actual tracer particle diameter d_p is 1 μm [67], and the particle size in the image should be at least 2 pixels, which is 13 μm, to avoid the "peak-locking effect". From these, the $f_\#$ can be calculated. Furthermore, The focal depth δz can be estimated from:

$$\delta z = 4.88\lambda f_\#^2 \left(\frac{M+1}{M}\right)^2. \tag{2.4}$$

The δz is essentially not equivalent to the sheet thickness H. Rather, it is the upper limit of the H if all particles illuminated need to be imaged in focus.

Pulse separation time Δt

There are three time scales involved in any typical PIV experiments: pulse duration δt, pulse separation time Δt, and the temporal resolution T, as shown in Figure 2.8. Among those scales, δt and T are mostly determined by instruments, while the Δt needs to be determined based on optimization rules for better correlation.

The primary principle of choosing Δt is preventing large displacement of any particles in an interrogation window, which is beneficial for increasing the signal-to-noise ratio (SNR). Both in-plane displacement and out-of-plane displacement should be considered as we would desire that a particle does not travel too long a distance in any direction. Ideally, the displacement in the y, z direction and in the x direction during the Δt should be smaller than 1/4 of the actual size of the interrogation window and laser sheet thickness respectively, and intersection of two results sets is the desirable Δt value, which means in mathematical terms:

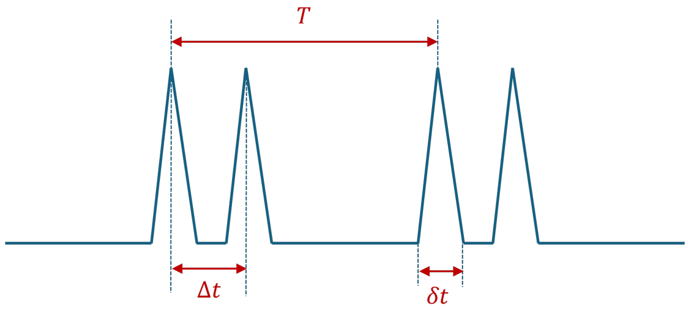

Figure 2.8: Schematic of different time scales in a typical PIV experiment.

$$\Delta t \leq \text{min}(\frac{1}{4}\frac{N_{\text{pixel}} \times l_{\text{pixel}}}{v}, \frac{1}{4}\frac{N_{\text{pixel}} \times l_{\text{pixel}}}{w}, \frac{1}{4}\frac{H}{u}), \tag{2.5}$$

where N_{pixel} is the pixel number of the interrogation window in each direction, l_{pixel} is the pixel pitch, H is the laser sheet thickness, v, w are in-plane velocities, and u is the out-of-plane velocity.

Parameters in the experiments

Two main measurement campaigns are in the thesis. The first is detailed measurement of flow pattern evolution along the suction side behind a tubercle peak, and the second is about the stall cell pattern at a plane close to the LE. The former campaign requires a larger M as one would need to zoom into a small region for preciser data, while for the latter, a much smaller M is needed since the purpose is to know about the interval between two separated regions.

In the first measurement campaign, the FOV is 5 mm along the span which covers 2 tubercles as shown in Figure 2.1. In Table 2.2, the sensor parameters are given, and the corresponding number of pixel for such a length is 2560. The magnification factor can then be calculated as:

$$M_1 = \frac{2560 \times 6.5\,\mu m}{5\,cm} = 0.3328, \tag{2.6}$$

which is relatively a large value for M, and this means that we will focus on a small region where more details can be revealed. The FOV dimensions are estimated to be about 5 cm $\times$ 4.22 cm. The 4.22 cm is the length of the FOV plane in the z direction. The $f_{\#}$ is computed to be around 7.5 based on a lens with f = 105 mm, and the depth of view δz is estimated to be around 2.3 mm, which provides a reference for the slot width of the light fence. In practice, the slot width is chosen to be 2 mm. The process of determining pulse separation time Δt is more like a trial-and-error as precise estimation of in-plane and out-of-plane velocities is not possible in practice, and it would be time-consuming to adjust it during the measurements. Therefore, the Δt is determined per inflow velocity: 75 μs, 30 μs, and 10 μs are chosen for inflow velocity 2 m/s, 5 m/s, and 15 m/s respectively. The corresponding streamwise displacement of a tracer particle moving at the inflow speed is 0.15 mm which is smaller than 1/4 of the laser sheet thickness.

In the measurement campaign of the SC pattern, 14 tubercles painted in black are in the FOV, and similarly, the magnification factor is calculated to be:

$$M_2 = \frac{2560 \times 6.5\,\mu m}{35\,cm} = 0.0475, \tag{2.7}$$

which is about 1/7 of the M_1, but should be enough for the SC pattern. The estimated parameters are summarized in Table 2.3. The parameters of the lenses are provided in Table 2.4. Those parameters are tested to be effective in experiments for the setting made in the previous estimation.

Table 2.2: Camera sensor parameters

Sensor resolution	2560 pixels × 2160 pixels
Pixel pitch	6.5 μm

Table 2.3: Estimated parameters of PIV measurements

	Campaign 1	Campaign 2
M [-]	0.3328	0.0475
δz [mm]	2	2
$\Delta t_{u=2}$ [μs]	10	20
$\Delta t_{u=5}$ [μs]	30	60
$\Delta t_{u=15}$ [μs]	75	150

2.6. Velocity measurements

A similar experimental setup is employed for both measurement campaigns, which is demonstrated in Figure 2.9. The first step of measurement at a new plane is to adjust the laser to align the laser sheet with a slot. The laser head should aim roughly at the center of the desired slot. In this process, the laser is regulated by its internal triggering signals, and the power is set to the lowest to avoid any potential harm to operators. Once the laser sheet is aligned with the slot, one should see a vertical green stripe flashing on the other side of the wall. Then, the camera can be calibrated by using a reference object with known scales. Ideally, the object face with known scales should be in the laser sheet and face the camera. Before the calibration process, the object face should be in focus, this can be achieved by tuning the f of the camera slightly. Once the face pattern is clear and sharp, a photo is taken and used to calibrate the length scale in the camera sensor. After the camera calibration, the object is removed and the wing model is put into the test section with both ends fixed at the wall at a desired AoA, which can be easily adjusted later by loosening the bolts on one end where the AoA mechanism is located. The seeding generator and the wind tunnel fan are turned on to create a fog. Once the seeding intensity is high enough, the seeding generator is turned off and the wind tunnel fan RPM is specified to obtain the desired inflow velocity in the test section. The laser is then switched to an external mode and its emitting is controlled by the PTU with input from the Davis software.

Three important parameters need to be specified in the Davis, which are laser pulse separation time Δt, the number of image pairs, and the laser power. The first is explained in detail in the previous section and the focus would be on the last two here. The number of image pairs represents the number of instantaneous velocity fields. The number should be large enough so that the average results obtained in the postprocessing can converge and the uncertainty from random sources is reduced. Therefore, the number is set as 1000, which takes around 70 s to acquire at the maximum data acquisition rate of 15 Hz. If the time of storing data is included, the total time of one measurement case would be around 5 minutes. The laser is determined by the imaging quality; If most tracer particles are clear and sharp in the FOV, the imaging quality can be considered as good. Otherwise, the laser power might need to be increased to ensure that the particles are illuminated and create enough scattered light. The imaging quality can also be improved by changing the $f_{\#}$ and making the laser head better aligned with the slot. In practice, the laser power is set to be above 80%, meaning 80% of the full capacity. In the second measurement campaign where the FOV is relatively large, the laser power is increased up to 90% to ensure enough illumination. The details of the parameters setup can be referred to in Appendix A.

The image pairs obtained are post-processed in the Davis 8 software and the defined operations are given in Figure 2.10. The 'frame shifting' operation is not a mandatory process for low-speed cases. However, for measurement cases in which the inflow velocity is 15 m/s, this operation is needed as the high-speed wind would cause strong vibration for the camera and thus the FOV is not fixed at where it should be. The idea of the operation is to shift frames by a displacement determined by the deviation from a selected reference point which should be located at the wing surface and reflect strongly. If all image pairs are taken in the same FOV, then they can be processed by the 'time filter', which subtracts the mean value of all image pairs from each image pair. This would get rid of the influence of background in the FOV

Table 2.4: Parameters of camera lenses

	Campaign 1	Campaign 2
f [mm]	200	120
$f_{\#}$ [-]	11	9

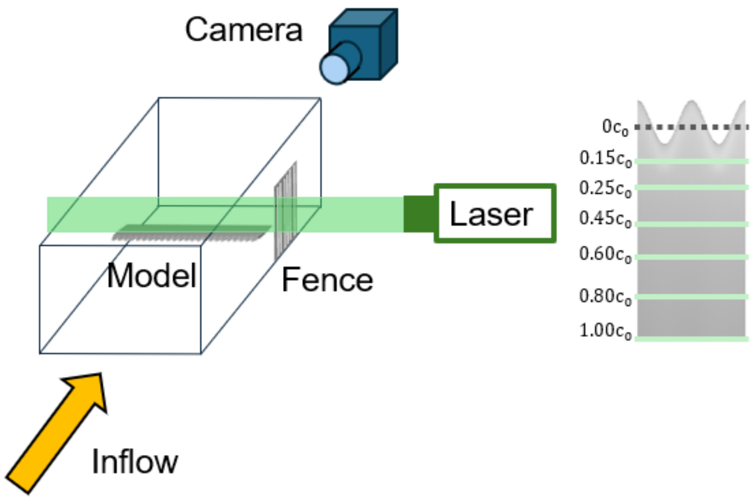

Figure 2.9: Schematic of the on-site setup in the wind tunnel.

and improve the imaging quality. 'PIV correlation' involves all necessary operations to obtain a velocity field from an image pair. A multi-pass approach is used to calculate the displacement correlation. The last interrogation window has the size 16 $\times$ 16 in pixel and the overlap ratio is set to be 50%, meaning that a velocity vector is determined for every 8 pixels in one direction. Therefore the size of the obtained instantaneous velocity field is 320 $\times$ 270 in pixels. The spatial resolution is 8 $\times$ 6.5 μm = 52 μm, which is small enough to resolve the BL to some degree. At the end of the postprocessing, the results of the mean velocity field and standard deviation (std) are obtained in the 'vector statistics' part, which can provide information on mean flow patterns and corresponding unsteadiness.

2.7. Wind tunnel correction

In the wind tunnel experiments, the tubercled wing models are tested in a closed test section. The effects of the test section wall and the model should be considered to correct the experimental data obtained. In this section, the aspects that need to be considered are discussed and it is shown at the end that all aspects can be ignored, and the correction is not necessary. In the tests, 2 full-span wing models are used and thus only 2D corrections are required. Three primary aspects are considered, which are the buoyancy effect, lift interference, and the blockage effect.

Buoyancy effect

The buoyancy effect is essentially a negative pressure gradient due to the growth of wall BL along the test section. The effective cross-section is reduced as the BL increases in thickness, which results in a contraction of the stream tube. The model immersed in this contraction section would experience an extra force in the streamwise direction, which needs to be removed from the experimental data. However, in the

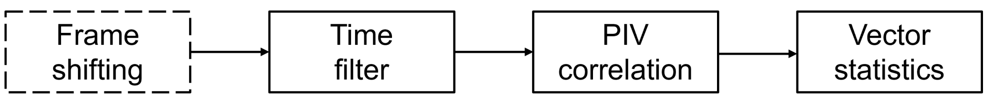

Figure 2.10: Flowchart of the PIV data postprocessing in Davis.

experiments of this thesis, the test section is short, and wing models are very close to the exit of the test section. Hence, the cross-section can be assumed to be constant at streamwise locations of the models, and the buoyancy effect can be left out.

Lift interference

Due to the existence of test section walls, the streamlines around the wing are modified, which further indicates that the lift obtained does not represent the real value. In other words, any lifting body tested in a closed test section would need to correct the lift data based on its theoretical lift performance. The tubercled wings tested, nonetheless, do not produce high lift and experience an early stall. Thus, the correction of lift interference is assumed to be small.

Blockage effect

The blockage effect is caused by either solid bodies or low-speed regions in the test section, which modifies the cross-section shape and flow speed along the section. The solid body in the context of the thesis work is the tubercled wing, which takes a certain place in the test section. The flow between the model and the test section wall would accelerate as the stream tube is reduced in diameter. This solid body blockage effect is ignored as well as the thickness of the wing is not large. Besides, the correction requires drag information, which is not measured in the tests. The blockage effect of the wake is considered and the correction factor is denoted as ϵ_{wb}, which is defined as the ratio between the velocity variation after correction and the un-corrected inflow velocity. It can be computed from [70]:

$$\epsilon_{wb} = \frac{\pi^2 t^2}{12h^2}\lambda_{2D}, \tag{2.8}$$

where t is the airfoil thickness, h is the test section height, and λ_{2D} is the Glauert shape factor. The Glauert shape factor can be determined indirectly by another shape factor Λ proposed by Allen and Vincenti [71]. For a tubercled wing, the shape factor Λ is defined as:

$$\Lambda = 4\frac{t^2}{c_0^2}\lambda_{2D}, \tag{2.9}$$

and its value can be estimated from Figure 2.11. The thickness ratio is 21% for the tubercled wing, and the Λ is estimated to be about 0.452. The correction factor is then calculated to be:

$$\epsilon_{wb} = \frac{\pi^2 t^2}{12h^2}\lambda_{2D} = \frac{\pi^2 c_0^2}{48h^2}\Lambda = \frac{\pi^2}{48}\,{\frac{0.1}{0.6}}^2\,0.452 \approx 0.26\%, \tag{2.10}$$

which is even smaller than the turbulence level of the wind tunnel operating at 5 m/s, and can be assumed to be negligible. Therefore, the experimental data can be used without corrections as their influences are small.

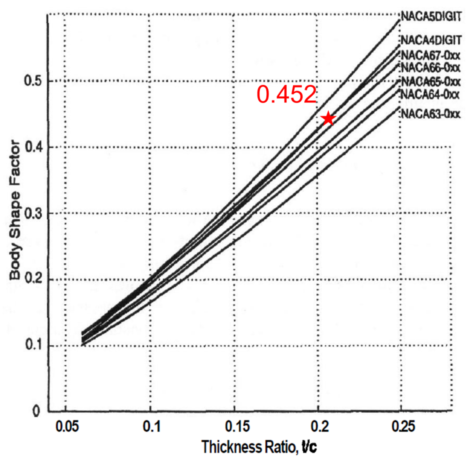

Figure 2.11: Values for Λ for several airfoil families (image credit: Barlow et al., 1999 [70]).

3

Results and discussion

The experimental results of wings A05 and A10 are discussed in this chapter. The chapter starts with a comprehensive discussion on wing 05 tested at U_∞ = 5 m/s in Section 3.1 regarding its SC patterns, pre- and post-stall mean velocity and mean vorticity results, LEV strength, and pre-stall flow structure evolution on its suction side. In Section 3.2 and Section 3.3, the influences of the tubercle amplitude and Re are examined on the aforementioned aspects . Lastly, the results are summarized in Section 3.4, which are informative for the theoretical study.

3.1. Flow field results

3.1.1. Stall cell patterns

The SC patterns were captured in the second measurement campaign, where 14 tubercles are in the FOV at three different AoAs, 5°, 10°, 15°, to provide a comprehensive view of the flow field evolution before narrowing our focus to a much smaller region on the surface.

The measurements were taken at the first slot, corresponding to the streamwise location x/c_0 = 0.15. In principle, the plane measured should be close to the LE as the SCs tend to merge downstream and thus would be difficult to distinguish. The mean streamwise vorticity of flow fields was used to visualize regions of strong shearing effect. This indicates the existence of SCs as a strong velocity gradient is expected to be found at boundaries. The streamwise vorticity can be obtained by using the formula below:

$$\omega_z = \frac{\partial \overline{v}}{\partial z} - \frac{\partial \overline{w}}{\partial y}. \tag{3.1}$$

Since the results are calculated from mean velocity fields, unsteadiness is absent. The velocity fluctuation is reflected in the std result. Without loss of generality, the std of the wall-normal velocity component v was used.

The results of mean vorticity fields and unsteadiness effect are shown in Figure 3.1 and Figure 3.2 respectively. At AoA = 5°, the stall does not occur yet and the vorticity magnitude is small. It can be observed that positive and negative ω_z regions are close to trough locations and their formation can be ascribed to the pressure gradient between peak and trough regions. However, the tubercle influence can still be seen by positive and negative ω_z regions and an upwash pattern, which both have a periodicity that is the same as that of tubercles. A similar phenomenon is observed in the corresponding std result, where the distribution of high std regions follows the same spatial frequency. It is also clear that those high std regions are located within a stripe region which corresponds to the regions affected by the upwash effect. The presence of tubercles would cause strong unsteadiness and increase the std close to the wing. The stall occurs when the AoA is increased to 10°, and an SC pattern can be seen in the ω_x result. Except for higher vorticity magnitude, the SC pattern changes as well; two obvious humps can be observed at y/λ = -4 and 2, which represent the SC development at an early stage. The flow separates first at trough locations due to the strong upwash effect which increases local AoAs. The extension of separated regions is inhibited by tubercles due to its compartmentalization effect [36]. Hence, the flow between two separated regions remains attached to a streamwise location further downstream and improves the post-stall performance of the wing. Another characteristic of the post-stall result is that the wall-normal

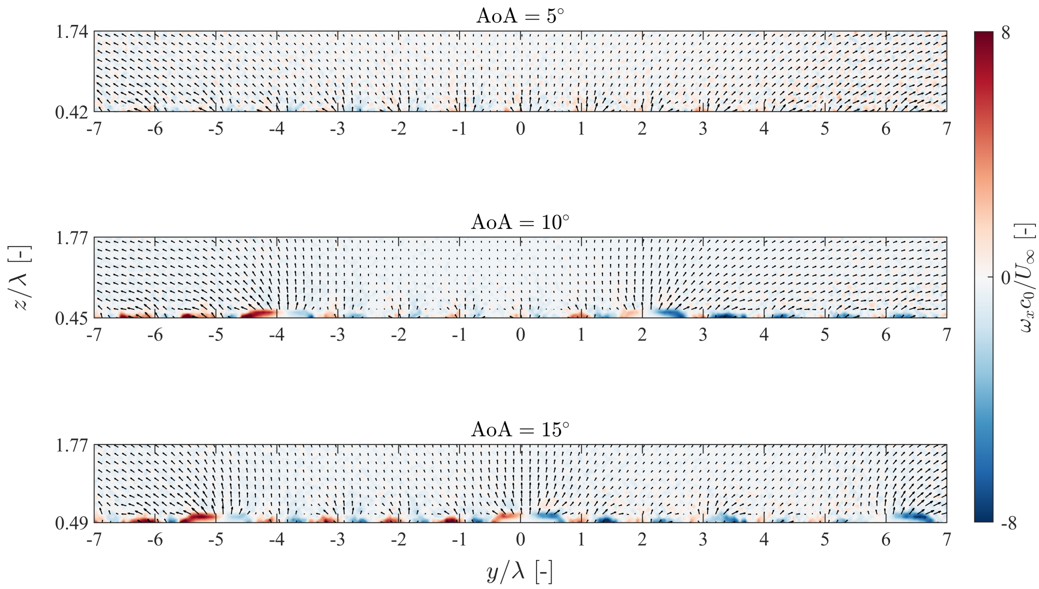

Figure 3.1: Contour plots of mean non-dimensionalized vorticity overlaid by vector fields of the mean velocity of A05 wing on the plane x/c_0 = 0.15, at AoA = 5°, 10°, 15°, U_∞ = 5 m/s, showing every 3rd vector for clarity.

Table 3.1: SC spacing of A05 (U_∞ = 5 m/s).

AoA [°]	5	10	15
SC spacing	-	6λ	5λ, 6λ

velocity at the SC locations is increased even at a location far away from the wing. This can be explained by the blockage effect of SC where the velocity is low and the flow is 'pushed' upward. The low-speed region inside the SC is also visualized in the std result. The regions of low unsteadiness are shown in a brighter color and can be categorized into two types. The first type is located near the wing and it has a half-spherical shape which is reminiscent of the SC structure seen in the vorticity result. This low-std feature can be ascribed to the low velocity in the 'dead water zone' inside an SC, where the velocity fluctuation is small [72]. The low-std region of the second type is above the SC corresponding to the high wall-normal velocity regions. The reason for the formation of the region could be that the acceleration of the flow reduces its turbulence level, which shares a similar mechanism of decreasing turbulence intensity by using a contraction section in a wind tunnel. It is also noted that the regions between two low-std regions are of high std, which can be attributed to the strong shearing effect as they are near the SC boundaries. When AoA is further increased to 15°, the ω_z magnitude continues to increase while the flow features are very similar to the previous case.

As found in post-stall cases, the high wall-normal velocity is one of the important features and can be used to indicate the SC locations. In Figure 3.3, the contour plots of $\overline{w}$ are given, which gives a clearer depiction of SC locations. It is found that a slight separation occurs at a trough location between two SC at AoA = 15°, which is also observed in previous research [17, 46, 47]. From the $\overline{w}$ contour plot, it is easy to calculate the SC spacing which is defined as the distance in λ between two trough regions of separated flow. The result are summarized in Table 3.1, and show that the SC spacing does not vary much from AoA = 10° to 15°.

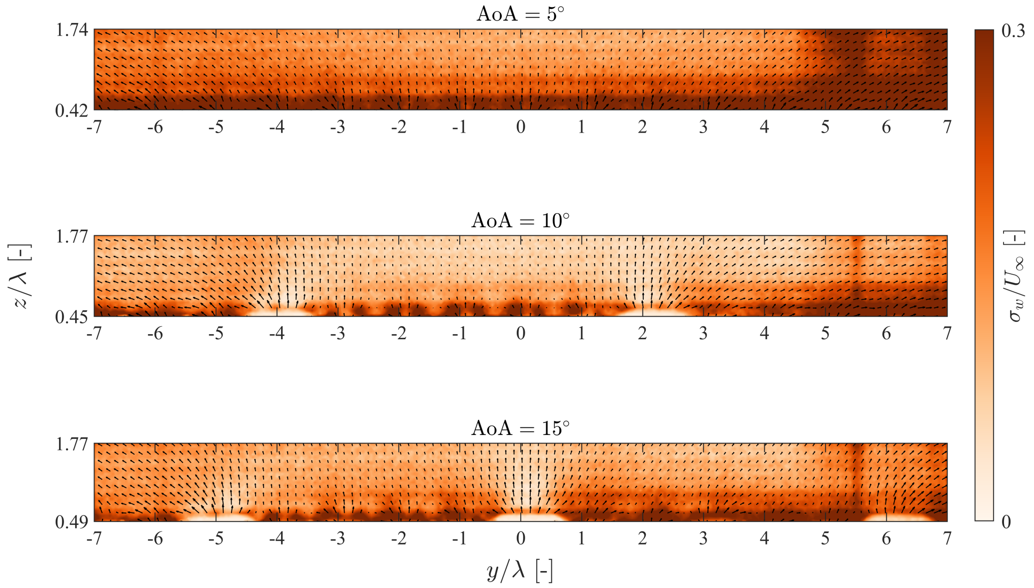

Figure 3.2: Contour plots of non-dimensionalized std of wall-normal velocity of A05 wing on the plane x/c_0 = 0.15, at AoA = 5°, 10°, 15°, U_∞ = 5 m/s, showing every 3rd vector for clarity.

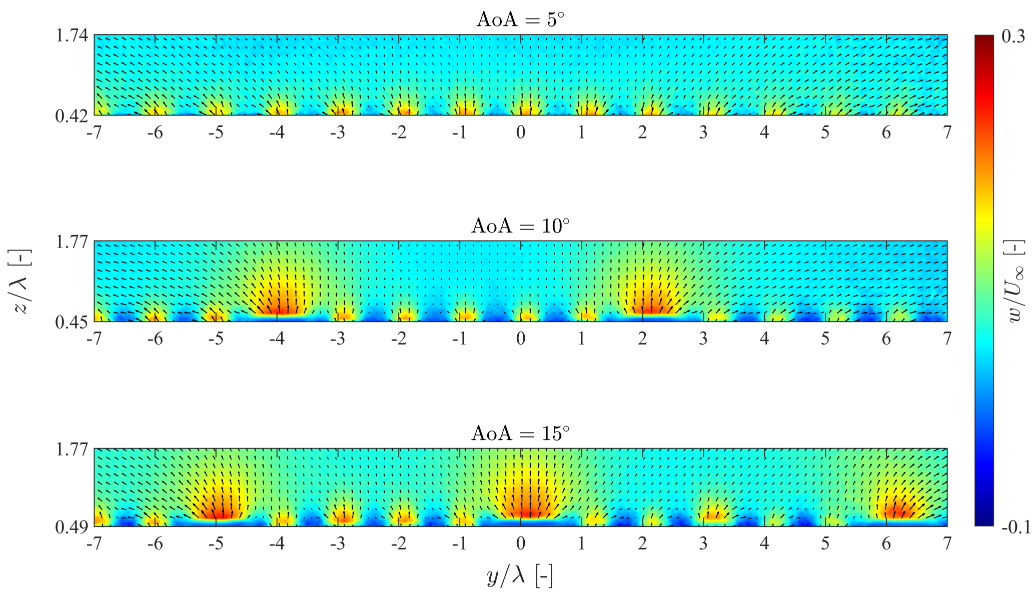

Figure 3.3: Contour plots of mean wall-normal velocity component of A05 wing on the plane x/c_0 = 0.15, at AoA = 5°, 10°, 15°, U_∞ = 5 m/s, overlaid by vector fields of the mean velocity, showing every 3rd vector for clarity.

3.1.2. Velocity and vorticity

The results of the SC pattern demonstrate a big picture of the whole flow field and its evolution. To further understand the detailed flow structures, the FOV is narrowed down and focuses on the cross-flow pattern behind a peak as demonstrated in Figure 2.9. In this part, the flow patterns on different streamwise planes at pre- and post-stall AoAs are examined first, followed by a discussion of cross-flow patterns close to the LE (i.e., x/c_0 = 0.15) which are expected to be instrumental about the tubercle effect.

Pre-stall stage

The SC pattern results show that the SCs have not emerge at AoA = 5°. Therefore, the cases of AoA = 0° and 5 ° can be safely regarded as pre-stall stages. However, the presence of tubercles complicates the cross-plane patterns even at such small AoAs as shown below.

Figure 3.4 shows cross-flow patterns at AoA = 0°. On the first plane x/c_0 = 0.15, which is the closest to the LE, the high vorticity regions are confined to a narrow region close to the wall which can also be inferred from the corresponding std result. The observation matches the results in Figure 1.5 and Figure 1.9. The tubercle effect can be represented by the mean velocity vectors pointing outward from trough locations. The background blue color is simply attributed to the limited number of levels for plotting the contour and does not mean the vorticity is high in the background. If the level number is increased, the background color should be that of ω_x = 0.

On the plane of x/c_0 = 0.25, the LEV sheets generated from the LE tubercles can be clearly observed, and the vortex sheet ends close to trough locations are slightly lifted. This result should not be surprising as the pressure gradient at trough locations is greater and thus LSBs are formed earlier behind troughs compared to other locations. The flow pattern shown is a result of the interaction between the LEV and LSB; the LEV sheets encounter the LSBs formed at troughs and their ends close to trough locations are deflected upward by LSBs. As demonstrated in the following results, the interaction between the LSB and LEV dominates the flow on the suction side and can be used to explain the observed flow pattern. The unsteadiness of this plane is the lowest among all planes measured which could be explained by the acceleration near the maximum thickness location (i.e., x/c_0 = 0.3) and the low-speed zones inside LSBs.

The pattern on the $x/c_0 = 0.45$ plane highlights the complexity introduced by the presence of tubercles along the LE. The sandwich structure observed in the vorticity result is believed to result from the LEV-LSB interaction. This feature structure is also found in Figure 1.10. However, the reason for the structure formation is not discussed in previous research. An attempt is made to explain its formation from the perspective of LEV-LSB interaction. As moving downstream, the LEV sheets continue to deform around the boundaries of separated regions and extra high vorticity regions occur below the rolled-up vortex sheets. Those newly identified regions are believed to be vortices that are generated inside LSBs. Similar structures are observed in a DNS result as shown [45]. Vorticity in these newly identified regions is of the same sign as the vorticity sheet above them, and thus the circulation should increase for example in a spanwise interval from a trough location to a peak location. This circulation variation is observed and will be discussed in the following subsection. Peculiar high vorticity regions are identified between the LEV sheets and extra high vorticity regions and the sign of the vorticity is the opposite of the other two layers of the sandwich. A possible explanation for this is that this middle layer is generated by the shearing effect of the other two layers below and above it. The high unsteadiness regions are very close to these sandwich structures, which supports the proposed explanation.

The LSBs are closed at a streamwise location between $x/c_0 = 0.45$ and $x/c_0 = 0.6$ as the std increases drastically in the regions downstream of LSBs, suggesting that the flow has transitioned to turbulence. Meanwhile, the 'sign switching phenomenon' occurs in the regions previously occupied by sandwich structures, as can also be observed in Figure 1.10. For instance, a large negative ω_z region is observed between $y/\lambda = 0$ and $y/\lambda = 0.5$, which is occupied by positive ω_z regions in the previous plane. The phenomenon can be explained by the shearing layer observed in the $x/c_0 = 0.45$ plane. This secondary layer gains energy from neighboring layers via the shearing effect and continuously grows in strength after its formation. In the end, the shearing layer dominates the spanwise interval and persists in the downstream.

After the transition, the turbulent BL can withstand a higher adverse pressure gradient and remain attached until a certain location, after which the BL separates which usually happens near the TE. The vorticity on the fifth plane $x/c_0 = 0.8$ is hardly visible as the flow is chaotic after separation and those fluctuations

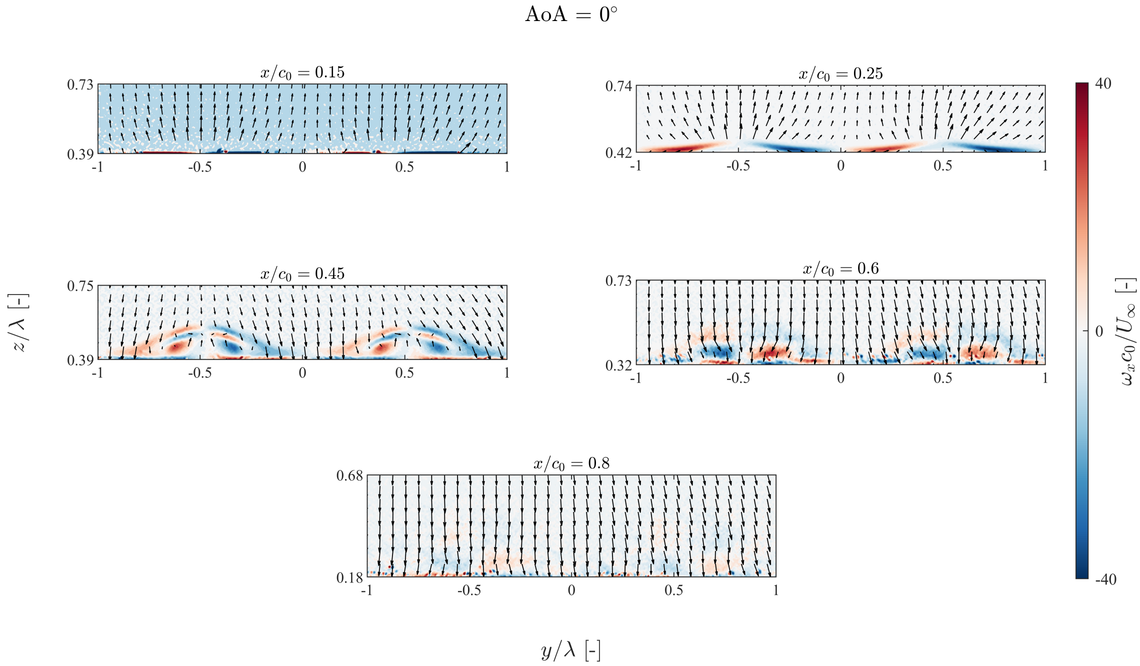

Figure 3.4: Contour plots of mean non-dimensionalized vorticity overlaid by vector fields of the mean velocity of A05 wing on the planes x/c_0 = [0.15, 0.25, 0.45, 0.6, 0.8], at AoA = 0°, U_∞ = 5 m/s, showing every 10th vector for clarity.

are removed after taking the average. The std result, nonetheless, can provide valuable information on the separated flow structure. The regions of higher std values in the plot are the wake regions where the velocity fluctuations are large. As can be seen in the result, the std values of the near-wall region are high, meaning that the flow has separated along the span.

At AoA = 5°, the cross-flow patterns are similar to that of AoA = 0°. However, due to the change of streamwise pressure gradient, the flow pattern evolves faster across planes. For example, on the first plane in Figure 3.6, the LEV sheets are observed already and are very similar to that of the second plane in Figure 3.4. Besides, the flow tends to separate earlier. The vorticity pattern becomes noisy already in the third plane. In short, the stronger pressure gradient makes the flow pattern develop faster and makes separation happen earlier. Therefore, although the measured planes are fixed, the relative locations where the velocities are measured are not the same from one AoA to another. In fact, this difference in measurement locations could provide more complete streamwise cross-flow patterns with a proper interpretation.

Post-stall stage

At AoA = 10°, the wing has already stalled and an SC can be seen in Figure 3.8. The flow FOV on the first plane is similar to that of lower AoAs, but on the second plane, the flow exhibits a clear preference; Positive and negative regions merge, resulting in higher standard deviation in those areas, which are also presented in the previous research [47]. On the x/c_0 = 0.25 plane, the region next to a separated region is captured. This region is well discussed by Pérez-Torró and Kim [47] due to the rolled-up vortex cores observed. In their research, the vortex core should be of the same sign as the neighboring separated shearing layer, whereas in the current result, the vortex has the opposite sign. Besides, the structure does not sustain its shape and deforms further downstream. The shear layer of the SC is captured in the std result. This SC layer becomes less distinguishable in the downstream planes where flow exhibits chaotic and irregular patterns. Hence, the previous choice of using the first plane for measuring SC patterns is justified by the results presented here.

Deep-stall stage

In a deep-stall region, the flow separates from the LE, and the lift is greatly reduced. Since the local stall behavior no longer exists, the periodic pattern can be seen again in Figure 3.10. The periodic pattern on

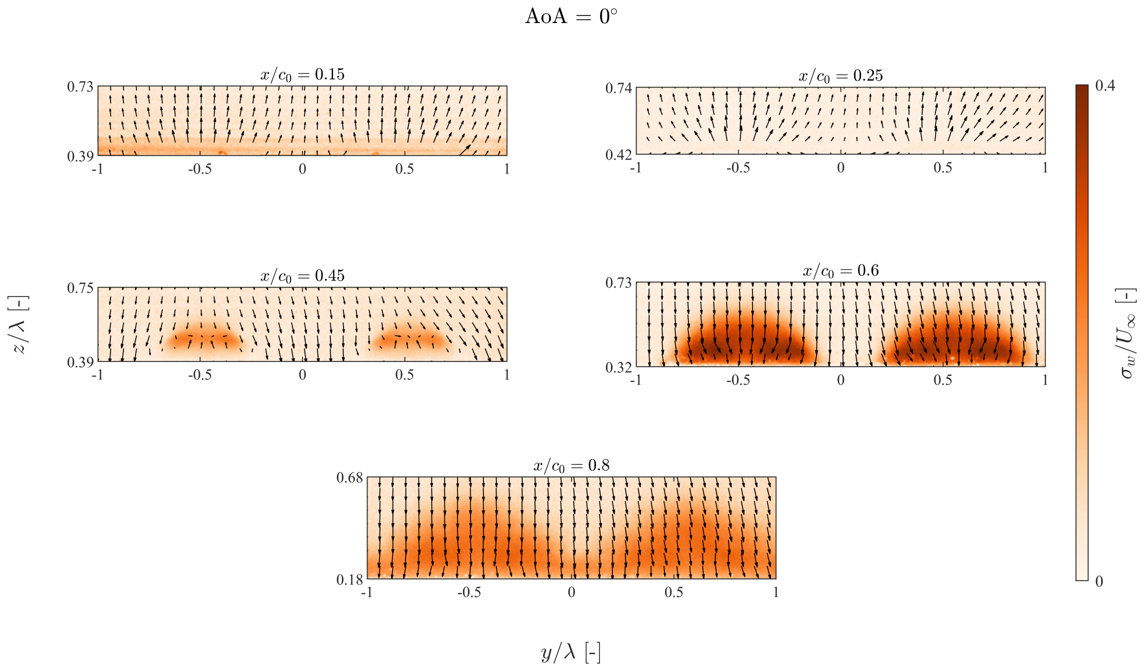

Figure 3.5: Contour plots of non-dimensionalized std of wall-normal velocity of A05 wing on the planes x/c_0 = [0.15, 0.25, 0.45, 0.6, 0.8], at AoA = 0°, U_∞ = 5 m/s, showing every 10th vector for clarity.

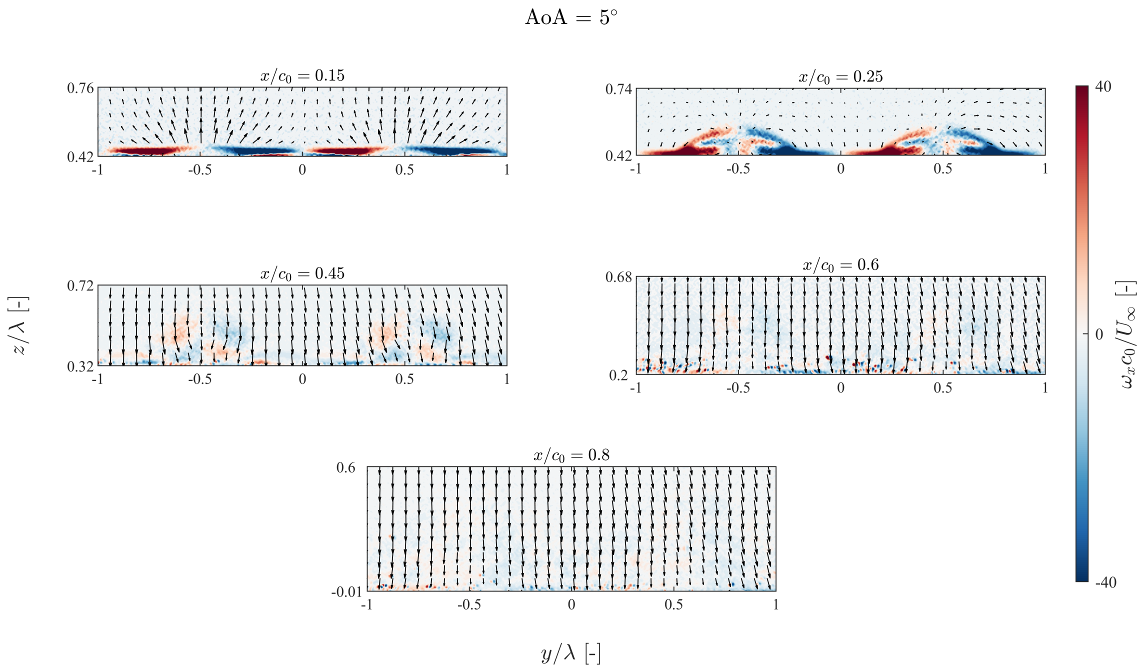

Figure 3.6: Contour plots of mean non-dimensionalized vorticity overlaid by vector fields of the mean velocity of A05 wing on the planes x/c_0 = [0.15, 0.25, 0.45, 0.6, 0.8], at AoA = 5°, U_∞ = 5 m/s, showing every 10th vector for clarity.

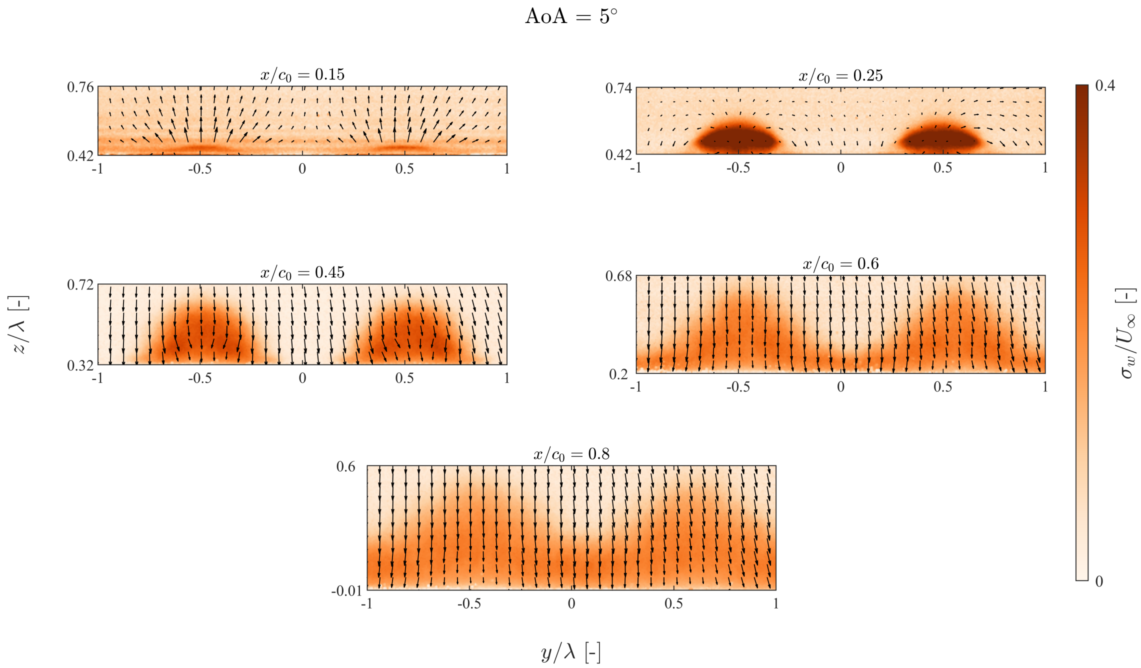

Figure 3.7: Contour plots of non-dimensionalized std of wall-normal velocity of A05 wing on the planes x/c_0 = [0.15, 0.25, 0.45, 0.6, 0.8], at AoA = 5°, U_∞ = 5 m/s, showing every 10th vector for clarity.

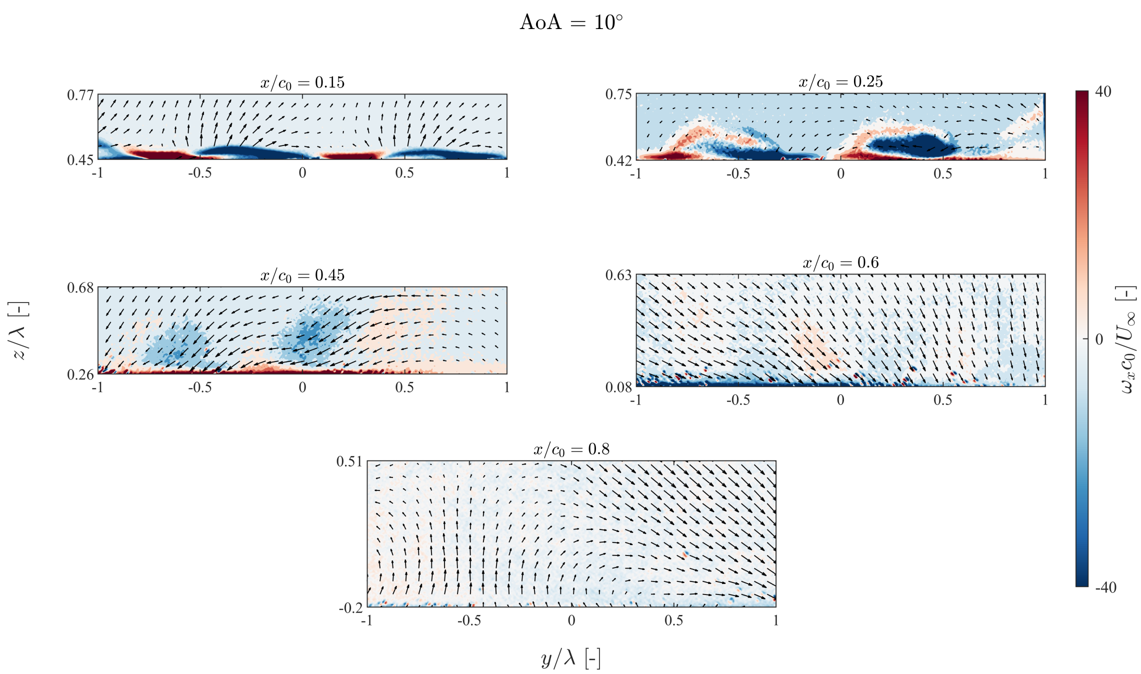

Figure 3.8: Contour plots of mean non-dimensionalized vorticity overlaid by vector fields of the mean velocity of A05 wing on the planes x/c_0 = [0.15, 0.25, 0.45, 0.6, 0.8], at AoA = 10°, U_∞ = 5 m/s, showing every 10th vector for clarity.

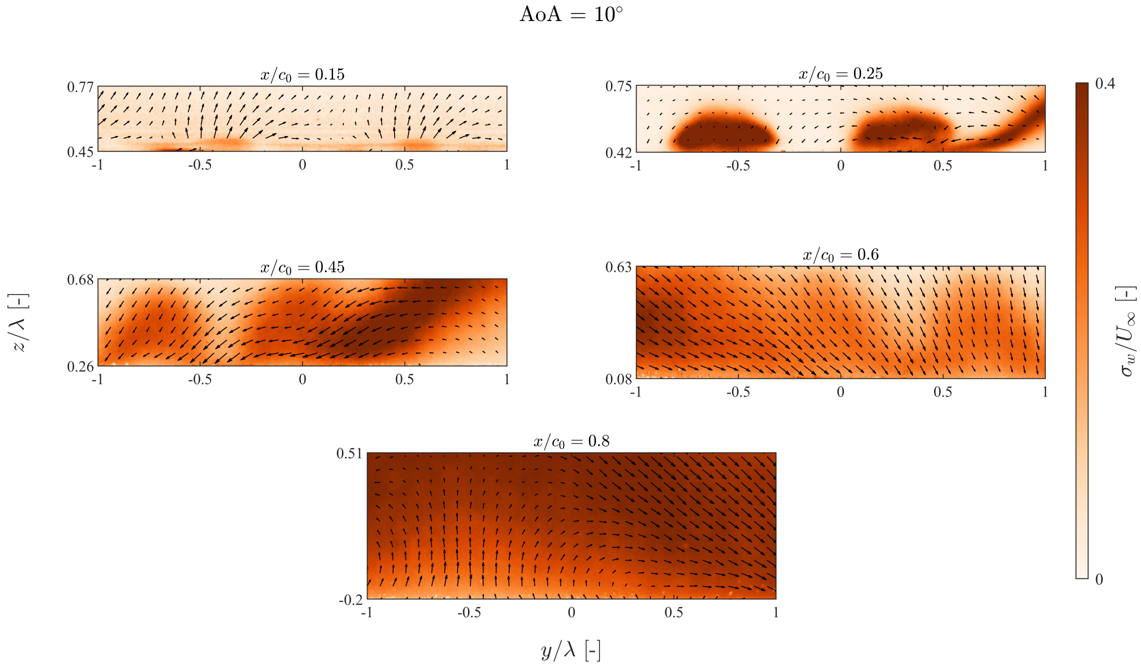

Figure 3.9: Contour plots of non-dimensionalized std of wall-normal velocity of A05 wing on the planes x/c_0 = [0.15, 0.25, 0.45, 0.6, 0.8], at AoA = 10°, U_∞ = 5 m/s, showing every 10th vector for clarity.

the first two planes indicates that tubercles can still modulate flow patterns even at a deep-stall stage.

Flow patterns near the LE

Unlike flow patterns on other streamwise planes, the flow features on the first two planes (i.e., x/c_0 = 0.15 and 0.25) can be distinguishable even at a high AoA, making them ideal for LEV formation study. Therefore, the first two planes are measured at 7 AoAs ranging from 0° to 30° with the intervals of 5° to provide more details on the cross-flow pattern evolution near the LE.

At the x/c_0 = 0.15 plane, the flow patterns are periodic at all AoAs as shown in Figure 3.12. The LEV sheets are close to the wing surface when AoA is smaller than 5° and remain so for the regions with SCs up to 15° where the unsteadiness at trough locations becomes high. At AoA = 20°, the flow undergoes a seeming transition process from partial separation to full separation as the flow structures at trough locations are not symmetrical and have certain preferences. When the AoA further increases, the flow on the suction side is fully separated, and the spanwise dependency of the separated flow does not exist anymore. The periodic pattern modulated by the tubercles appears again. One curious feature of averaged flow patterns at troughs is their squared shapes, which are also observed at the cross-plane close to the trough LE [30]. The velocity fluctuations along the upper boundaries of these deep-stall structures are significant, likely due to the strong shearing effect. The flow patterns demonstrate a similar trend of evolution on the next plane as shown in Figure 3.14, At AoA = 0° and 5°, the high vorticity regions are near the wing while the fluctuations are high in these regions. Further increase of AoA to 15° results in SC formation at certain trough locations and an SC structure on the cross-plane is nicely captured in the case of AoA to 15°. The lifted shearing layer covering several tubercle wavelengths is well demonstrated by the std result. The region below shows less uncertainty due to the low flow speed there. When the AoA is in a deep-stall region, the periodicity shows up again but the results are not completely the same as that of the previous plane. the flow patterns at troughs evolve from squared shapes into more rounded ones. In addition, the periodicity in the case of AoA = 15° is estimated to be twice λ, which could be ascribed to the transition to full separation as discussed previously.

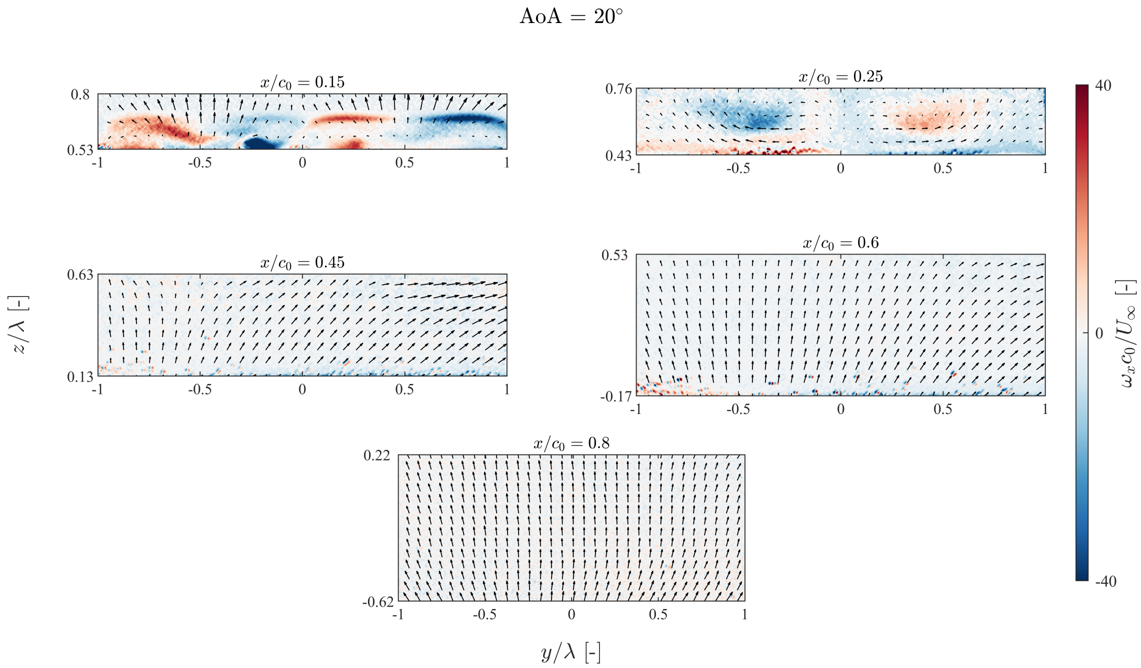

Figure 3.10: Contour plots of mean non-dimensionalized vorticity overlaid by vector fields of the mean velocity of A05 wing on the planes x/c_0 = [0.15, 0.25, 0.45, 0.6, 0.8], at AoA = 20°, U_∞ = 5 m/s, showing every 10th vector for clarity.

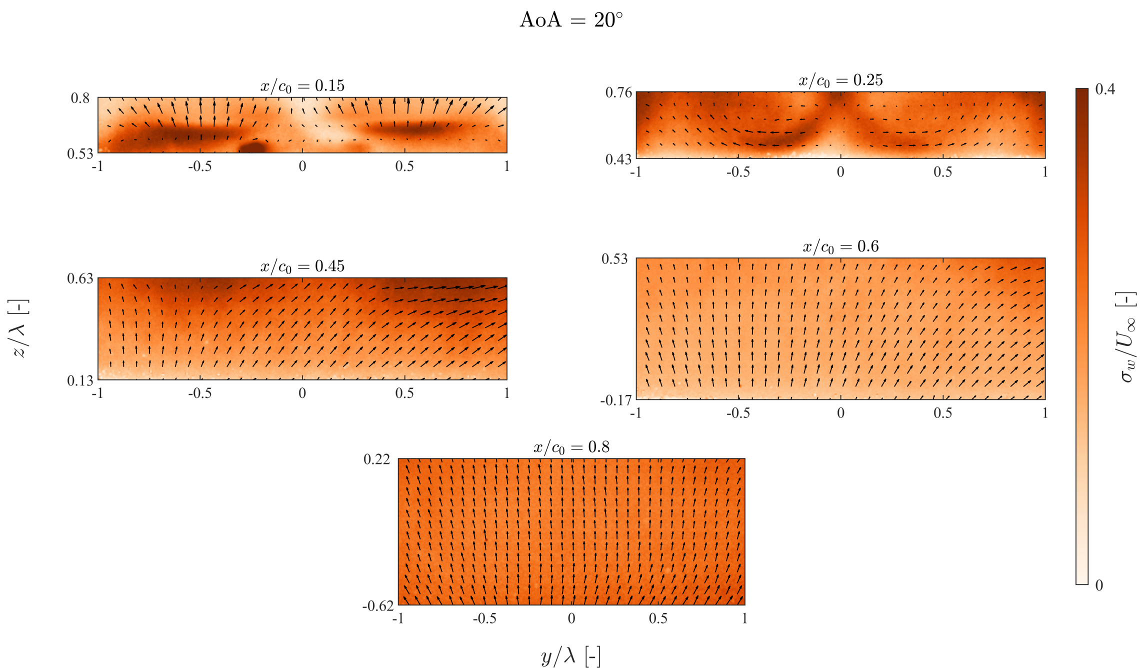

Figure 3.11: Contour plots of non-dimensionalized std of wall-normal velocity of A05 wing on the planes x/c_0 = [0.15, 0.25, 0.45, 0.6, 0.8], at AoA = 20°, U_∞ = 5 m/s, showing every 10th vector for clarity.

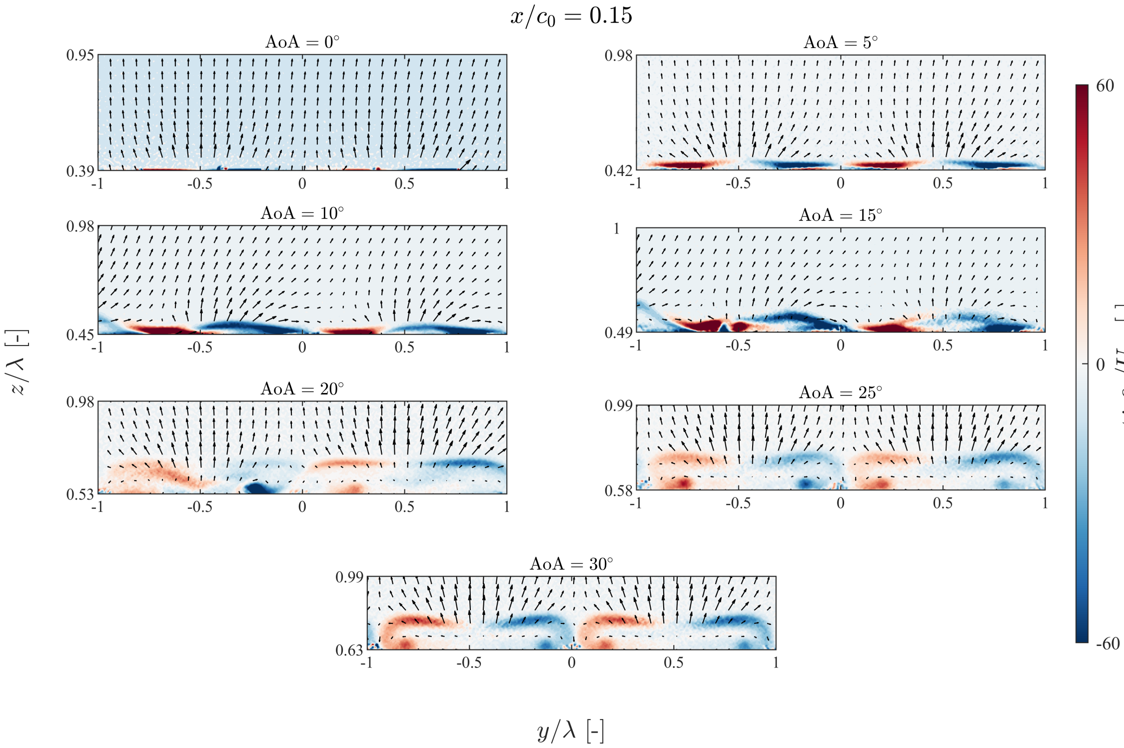

Figure 3.12: Contour plots of mean non-dimensionalized vorticity overlaid by vector fields of the mean velocity of velocity magnitude of A05 wing on the plane x/c_0 = 0.15, at AoA = [0°, 5°, 10°, 15°, 20°, 25°, 30°], U_∞ = 5 m/s, showing every 10th vector for clarity.

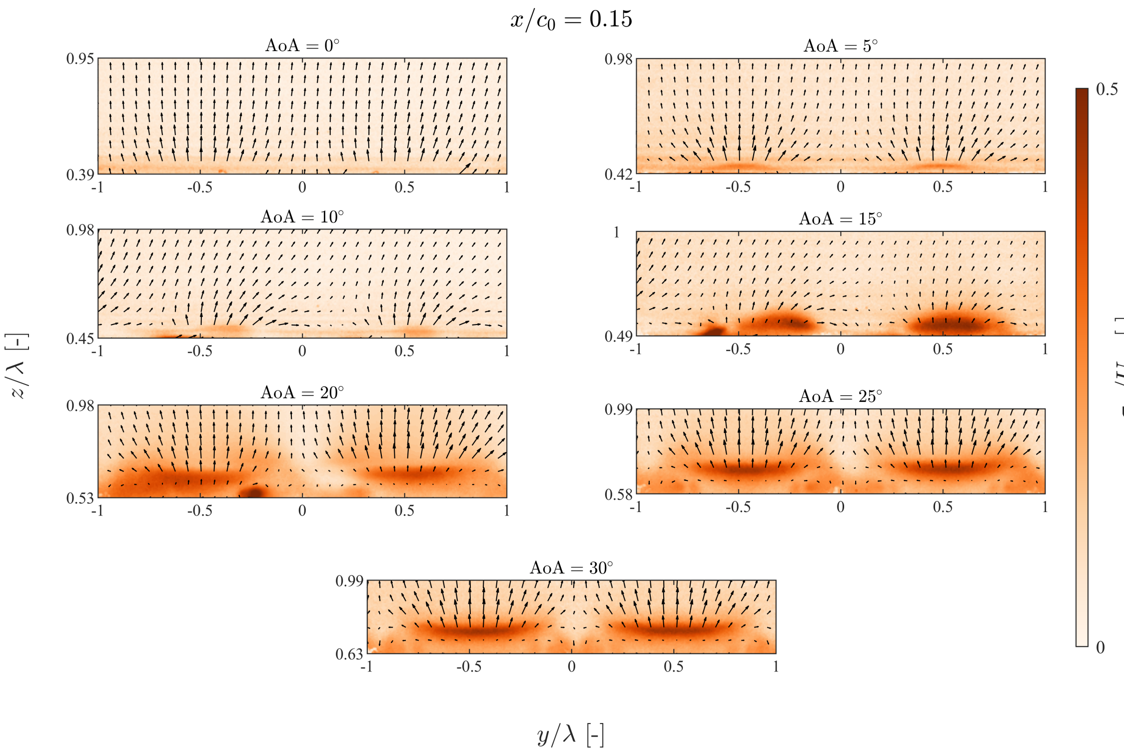

Figure 3.13: Contour plots of non-dimensionalized std of wall-normal velocity of A05 wing on the plane x/c_0 = 0.15, at AoA = [0°, 5°, 10°, 15°, 20°, 25°, 30°], U_∞ = 5 m/s, showing every 10th vector for clarity.

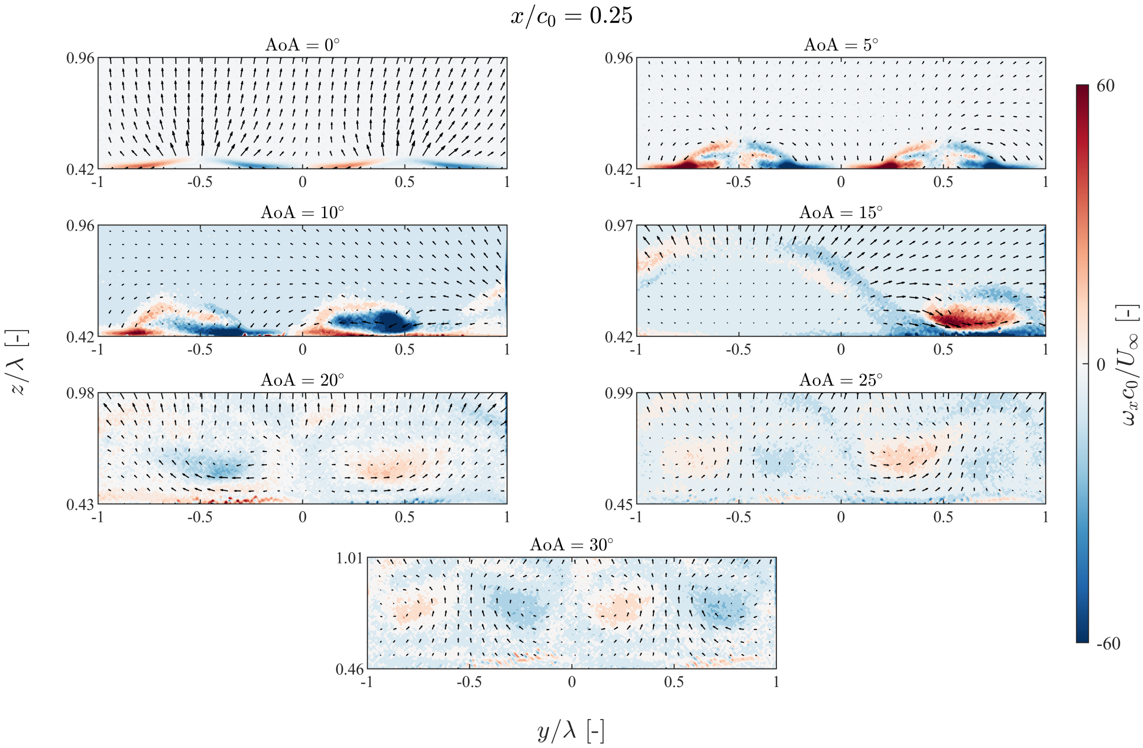

Figure 3.14: Contour plots of mean non-dimensionalized vorticity overlaid by vector fields of the mean velocity of velocity magnitude of A05 wing on the plane x/c_0 = 0.25, at AoA = [0°, 5°, 10°, 15°, 20°, 25°, 30°], U_∞ = 5 m/s, showing every 10th vector for clarity.

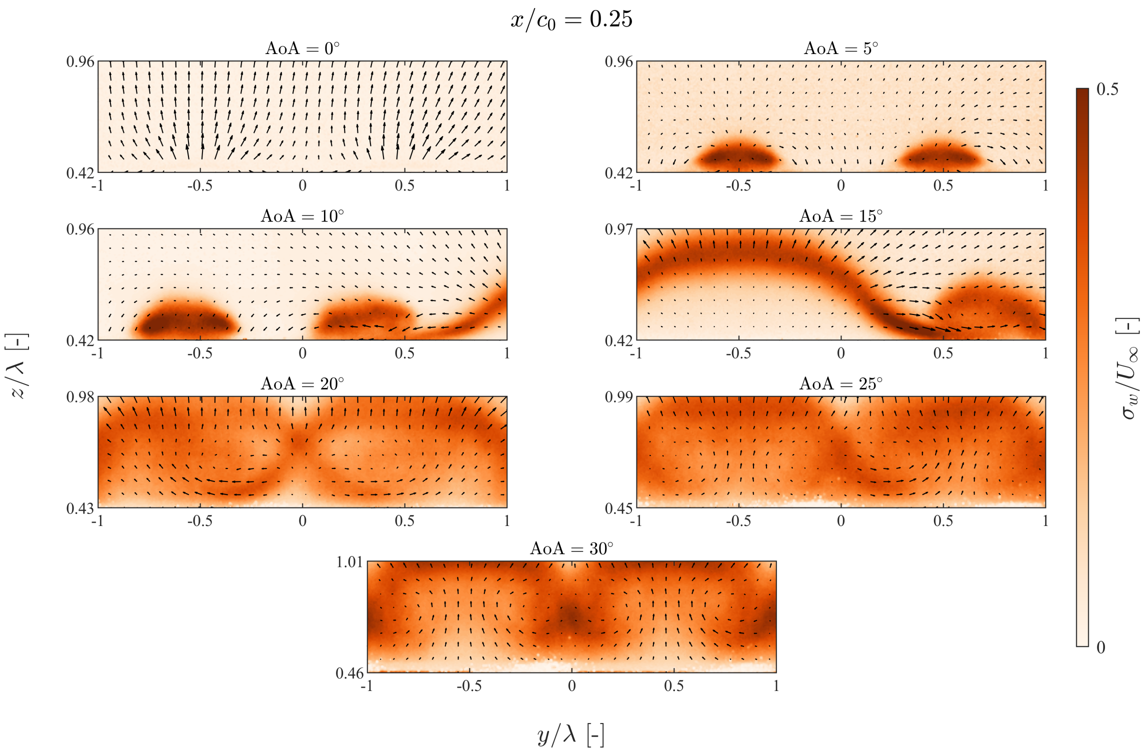

Figure 3.15: Contour plots of non-dimensionalized std of wall-normal velocity of A05 wing on the plane x/c_0 = 0.25, at AoA = [0°, 5°, 10°, 15°, 20°, 25°, 30°], U_∞ = 5 m/s, showing every 10th vector for clarity.

3.1.3. LEV strength

To quantify the flow behaviors close to the LE, the streamwise circulation can be a good choice as it requires only the velocity data on the plane and can provide insights into LEV strength evolution.

There are two approaches of calculating the circulation, which are line integral and surface integral. If we denote the circulation as Γ, the formulae would be:

$$\Gamma = \oint \vec{V}_{2D} \cdot \mathrm{d}\vec{l} = \iint \overline{\omega_x} \mathrm{d}y \mathrm{d}z, \tag{3.2}$$

where $\vec{V}_{2D}$ is the velocity vector in the plane and $\vec{l}$ is the trajectory vector along the integration path. The line integral approach is preferred for calculating Γ in a region close to the wall as it could provide a more precise result by combining physical knowledge. To illustrate the advantages of line integral, a schematic of calculating Γ near the wall is given in Figure 3.16. A box colored in blue is defined as the region of interest and four edges are represented by black lines with arrows following the conventional counterclockwise direction. The line in red is the bottom line and is supposed to be located on the wall in the FOV. Ideally, by implementing integration over this domain or edges, the Γ can be estimated accurately from the wall to a certain height. However, the red line does not always represent the bottom line on the wall. Instead, it is way above the wall due to the imperfect masking of FOV and light reflection at the wing surface; in the 'PIV-correlation' part, a binary mask with its bottom edge close to the wall is applied to images to save time in correlation operation and avoid contamination from reflected light. Therefore, a part of vorticity in the region between the blue domain and wing surface is neglected. Since the region is very close to the wall where the viscosity effect is strong, its contribution to the vorticity generation should not be excluded. The line integral approach, however, can be used to solve this problem with the knowledge that the velocity at the wall is zero due to viscosity. The non-slip boundary condition can be implemented by assuming the velocity along the red line is zero, which means the red line is 'forced' to be at the wall no matter what its actual location is. The contribution from the velocity along the two dashed vertical lines aside is ignored which can be justified by the fact the wall-normal velocity is damped strongly towards the wall and can thus be left out.

Two boxes are defined to quantify the positive and negative vorticity magnitude on both sides of a tubercle peak. The boxes are close to the wall and are centered in the intervals y/λ = [-0.5, 0], and y/λ = [0, 0.5] with the size 76 $\times$ 61 in vector. The results of circulation are non-dimensionalized by $c_0 U_\infty$ and shown in Figure 3.17. At the first plane, the non-dimensionalized circulation starts from a non-zero value at AoA = 0° and reaches about 0.06 at the maximum AoA. The non-zero circulation at the beginning can be ascribed to the thickness effect of the wing, which results in velocity gradients in the plane. Although the general trend is increasing, the positive circulation magnitude and negative circulation magnitude drop at AoA = 10° and 20 $^\circ$ respectively. The former can be explained by the transition to a post-stall state, and the latter could be ascribed to the transition to a full stall. The circulation evolution on the second plane is chaotic; the circulation labeled as positive or negative even switches the sign at the AoA ranging from 10° to 20° due to strong unsteadiness. Besides, the circulation is smaller compared to that on the first plane. The reason can be that the merging of two vorticity regions with opposite signs neutralizes the regions of high vorticity. In addition to that, the viscosity can also play a significant role in strength diffusion and dissipation between two planes.

The LEV strength can be used as an indicator to study the role of tubercles in the flow control. In Figure 3.18, a comparison is made between experimental results and analytical results. The circulation predicted by the analytical models increases as AoA becomes high, as the models are based on potential flow assumption where the flow reattaches on the wing after separation. Therefore, non-linear effects such as separation are not considered in the models and the circulation continues to grow even after the stall AoA is reached. This could be true for a delta wing but not for a tubercle. In the experiments, however, non-linear effects such as SC occur at an AoA between 5° and 10°, which can explain the deviation between predictions and experimental data in high AoA regions. The analytical results agree better with experimental ones when AoA is small. However, this does not lead to the conclusion that a tubercle can be taken as a small delta wing on the aspect of vorticity generation. The reason is that the potential flow assumption is made which means that Re of the models is much higher than that of experiments. This difference, as will be discussed in detail in Section 3.3, has a great influence on the LEV strength. Custodio [30] used a tubercled wing whose amplitude is 12%c_0 and wavelength is 50%c_0 for LEV strength measurement. The result is given in

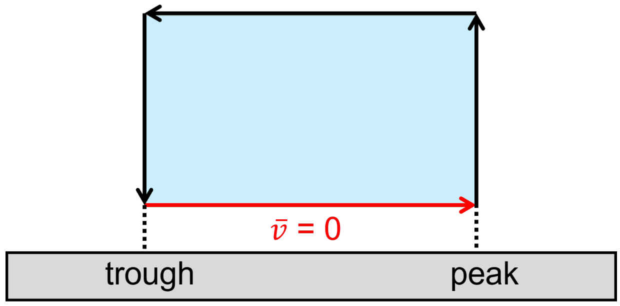

Figure 3.16: Schematic of the line integral used to calculate the circulation. The grey region represents the wing model.

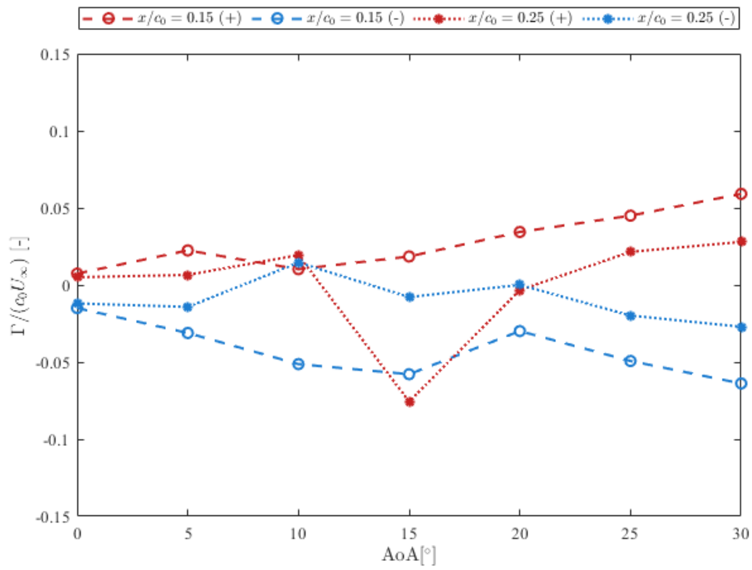

Figure 3.17: Streamwise LEV strength of A05 wing on the planes x/c_0 = 0.15 and 0.25, at AoA = [0°, 5°, 10°, 15°, 20°, 25°, 30°], U_∞ = 5 m/s.

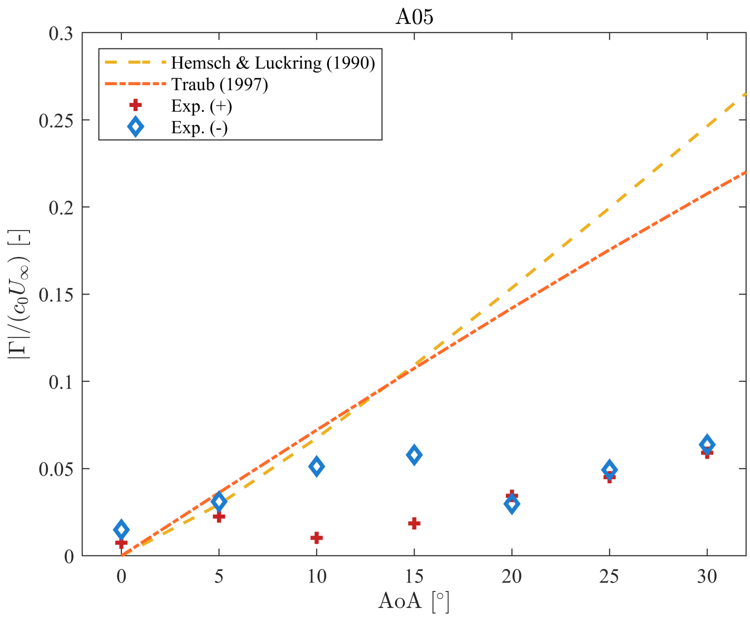

Figure 3.18: Results of streamwise LEV strength obtained experimental data and theoretical estimation of A05 wing on the plane x/c_0 = 0.15 at AoA = [0°, 5°, 10°, 15°, 20°, 25°, 30°].

Figure 3.19, and a large difference is observed even at small AoAs. Therefore, it can be concluded that a tubercle cannot be taken as a small delta wing, especially in terms of the LEV vortex generation.

3.1.4. Pre-stall flow patterns

The interaction of vortices and LSBs on the wing suction side at pre-stall AoAs is considered crucial for the flow evolution leading to SC formation. Therefore, pre-stall flow patterns are investigated qualitatively and quantitatively, aiming to offer further insights into the flow structures and vortex dynamics.

Streamwise velocity gradient

Although the velocity field results are only available on 2D cross planes at several streamwise locations, the velocity variation in the streamwise location can be obtained by using the mass conservation law, or continuity equation. If the flow is incompressible and the fluid density is assumed to be constant, the continuity equation can be written as:

$$\nabla \cdot \vec{V}_{3D} = \frac{\partial \overline{u}}{\partial x} + \frac{\partial \overline{v}}{\partial y} + \frac{\partial \overline{w}}{\partial z} = 0, \tag{3.3}$$

where the $\vec{V}_{3D}$ is the mean velocity in the 3D flow field. The streamwise velocity gradient can then be expressed to be:

$$\frac{\partial \overline{u}}{\partial x} = -\left(\frac{\partial \overline{v}}{\partial y} + \frac{\partial \overline{w}}{\partial z}\right). \tag{3.4}$$

In Figure 3.20, the results of the non-dimensionalized streamwise velocity gradient are given. In the case of AoA = 0°, planes can be categorized based on their relative locations to the maximum thickness location of the airfoil, which is x/c_0 = 0.3 for all spanwise stations. For those planes located in front of the maximum thickness location, the pressure gradient is favorable and the flow is accelerated outside BL, as can be seen in the background where the streamwise gradient is positive. Inside BL, however, the velocity gradient is negative as the velocity close to the wall is decreased due to viscosity. By comparing the results on the first plane and the second plane, the growth of BL can be observed as well and is obvious for that located at a trough location. After passing the maximum thickness location, the adverse pressure

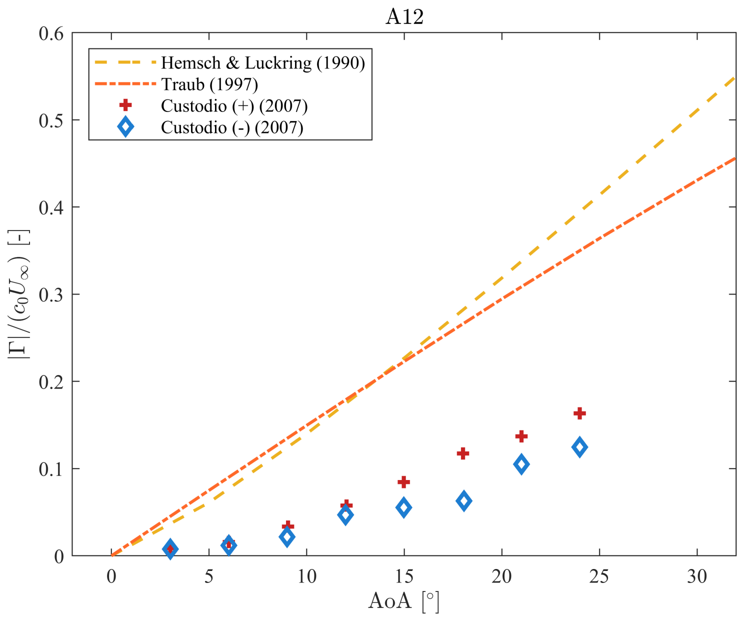

Figure 3.19: Results of streamwise LEV strength obtained experimental data and theoretical estimation of A12 wing tested at Re = 15000.

gradient dominates the flow outside BL and the flow is decelerated as shown in the blue regions in the background. On the third plane, the BL is represented by the strip region in red, which is lifted by pairs of round negative velocity gradient regions at trough locations and those deceleration regions are supposed to be caused by vortices generated inside LSBs. In fact, the flow inside BL is not accelerated and the positive gradient can be explained by that the planes considered are not normal to the wing surface, rather they are perpendicular to the bottom wall of the test section. Therefore, the velocity gradient is evaluated in a direction pointing through the BL, from a low-speed zone to a high-speed zone, making the results positive. In the following plane, the declaration regions disappear probably due to the reattachment of BL. The transition occurs and the flow becomes turbulent which allows the flow to withstand a higher adverse pressure gradient without separation. The separation occurs at a location between x/c_0 = 0.6 and x/c_0 = 0.8 as the positive velocity gradient is lower in the last plane, meaning that the flow is in a low-speed separated wake region.

The results are similar to the case of AoA = 5° as shown in Figure 3.21, except for the second plane. Unlike the third plane in Figure 3.20, the positions of deceleration regions and acceleration regions are switched. Due to the similarity between flow structures seen in the third plane of Figure 3.4 and the second plane of Figure 3.6, the result difference can be attributed to the difference in locations of measurement. The plane location could be in the rear part of the LSB, where the transition occurs and the flow experiences significant recirculation, as the unsteadiness is strong as shown in the std result of the second plane in Figure 3.6. The increased AoA results in a stronger adverse pressure gradient along the suction side and the flow is inclined to early separation which can be seen on the last three planes in Figure 3.20

Streamwise circulation evolution

The pre-stall streamwise circulation evolution can provide information on the pre-stall flow patterns from a quantitative perspective. The streamwise circulation is calculated in the same way as discussed in Subsection 3.1.3. In Figure 3.22, the circulation evolution of positive and negative vorticity region shows symmetrical patterns for AoA = 0° and AoA = 5°, as the separation does not occur yet. The general trend shows that circulation starts with high values on the first plane, gradually decreases to lower values, and then remains relatively constant towards the rear part of the wing. Besides, the larger the AoA, the higher the circulation of the first plane. At AoA = 0°, the trend is not completely true. Despite the high circulation observed at the first plane and the smaller circulation at the second plane, the circulation reaches another peak that is comparable in magnitude to that of the first plane, followed by the 'sign switching' phenomenon

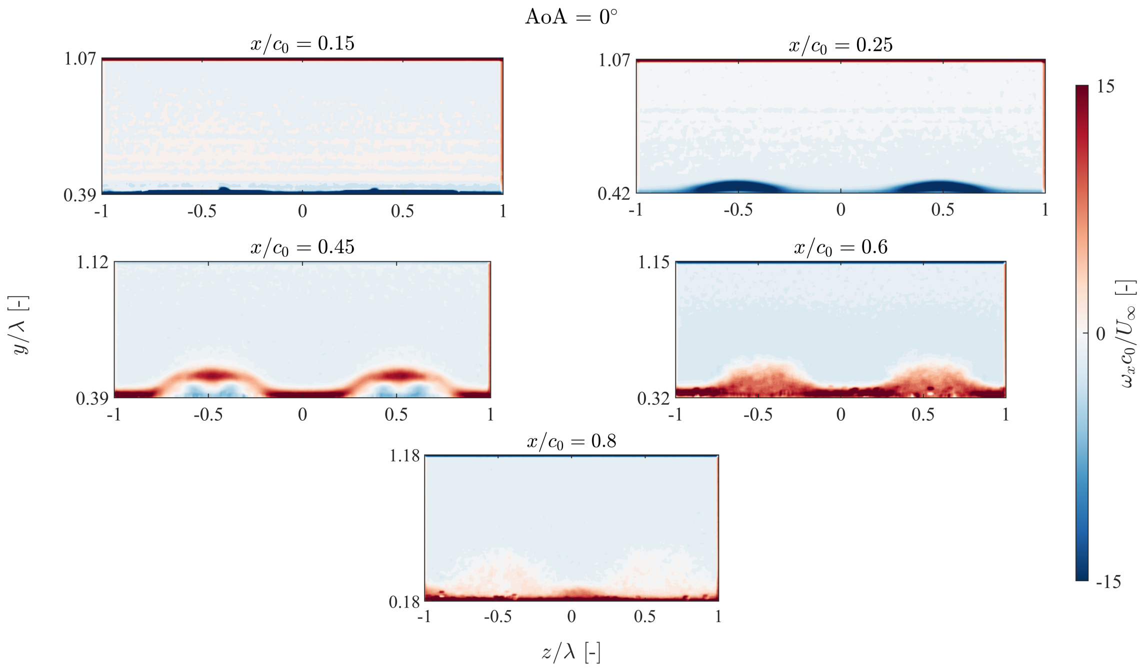

Figure 3.20: Contour plots of streamwise velocity gradient of A05 wing on the planes x/c_0 = [0.15, 0.25, 0.45, 0.6, 0.8], at AoA = 0°, U_∞ = 5 m/s.

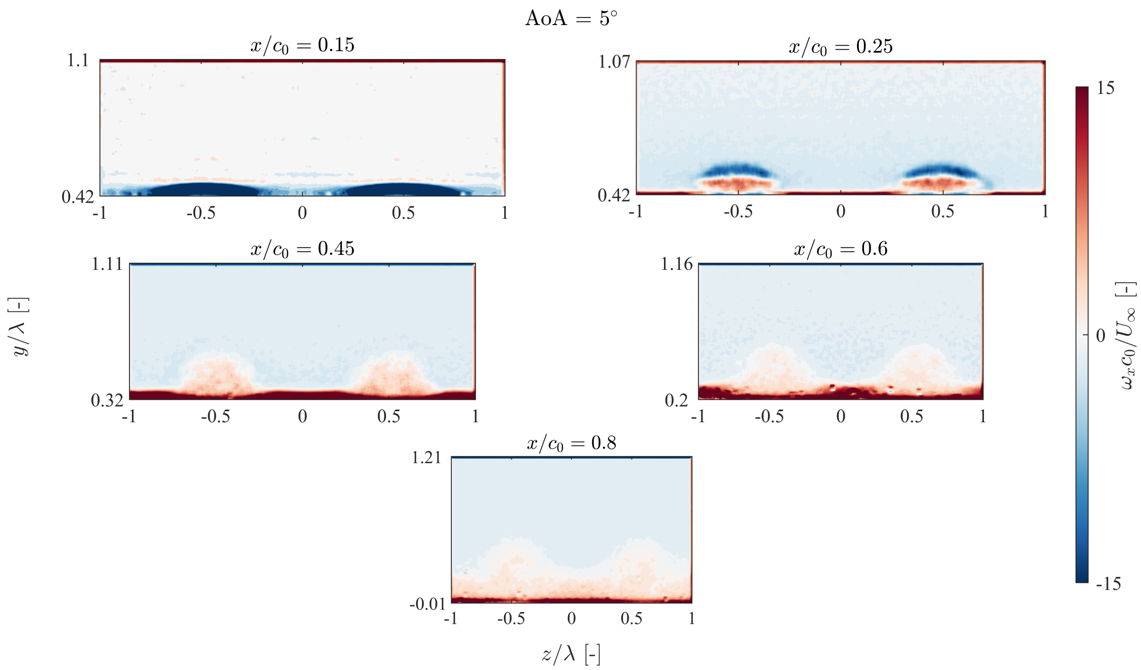

Figure 3.21: Contour plots of streamwise velocity gradient of A05 wing on the planes x/c_0 = [0.15, 0.25, 0.45, 0.6, 0.8], at AoA = 5°, U_∞ = 5 m/s.

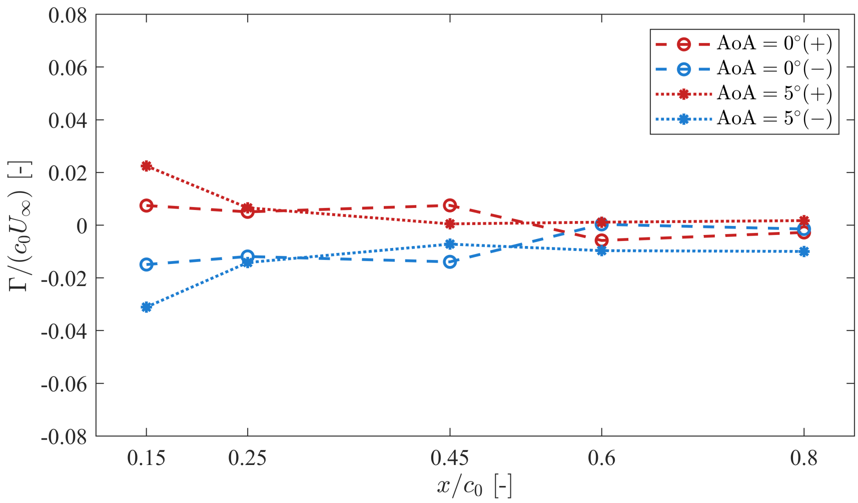

Figure 3.22: Plot of non-dimensionalized streamwise vorticity evolution behind a peak of A05 wing on the planes x/c_0 = [0.15, 0.25, 0.45, 0.6, 0.8], at AoA = [0°, 5°], U_∞ = 5 m/s..

at the fourth plane which is also observed in the results of velocity and vorticity. The observed increase of circulation can be ascribed to the new vortices emanating in the LSBs demonstrated in Figure 1.7, and the result here can be regarded as extra evidence supporting the analysis of the pre-stall flow pattern in Subsection 3.1.2. The newly generated vortices contribute to the circulation increase, otherwise, the circulation should gradually decrease due to viscous diffusion and dissipation as in the case of AoA = 5 °. The absence of the circulation increase and 'sign switching' phenomena could be attributed to the stronger adverse pressure gradient and earlier flow separation.

Vortex core distribution

Previous results primarily focused on vorticity in the flow field, providing valuable insights into flow patterns where viscous effects cannot be ignored. However, a region of high vorticity does not necessarily indicate the presence of a vortex. While a vortex represents a region where fluid elements rotate around an axis, vorticity quantifies the shearing effect in the flow field. For example, vorticity within the BL is high due to a large velocity gradient, yet no vortex can be found there.

To identify vortices in the flow field, the Q-criterion is employed. This criterion is based on the principle that, in regions where a vortex exists, rotational motion should dominate over the stretching motion of the flow elements. For the incompressible with constant density on a 2D plane, the Q of the mean flow field can be calculated from [73]:

$$Q = -\frac{1}{2}(\overline{u}_{i,j}\overline{u}_{j,i}) = -\frac{1}{2}\left[\left(\frac{\partial \overline{u}}{\partial x}\right)^2 + \left(\frac{\partial \overline{v}}{\partial y}\right)^2\right] - \frac{\partial \overline{u}}{\partial y}\frac{\partial \overline{v}}{\partial x}. \tag{3.5}$$

In Figure 3.23 and Figure 3.24, the isoline of Q = 0.001 and 0.002 are overlaid with non-dimensionalized ω_x for AoA = 0° and 5° respectively. The LEV sheet generated along the LE and the vortices inside LSBs are identified successfully, but vortices are difficult to identify when separation occurs as the concentrated vortices become scattered and the magnitude reduces due to the unsteadiness. Vortex cores are identified by calculating the mean locations of pixels with Q values that exceed specified thresholds in regions of high Q separately. Results of vortex cores distribution are given in Figure 3.25 and Figure 3.26 respectively. From the top view, it can be concluded that the vortices generated on the suction side are very close to the wing surface. Additionally, the vortices near the LE are difficult to identify due to the small thickness of the LEV sheet, and they tend to break down earlier at a higher AoA. In the top view results, the vortices generated are clearly visible, along with the 'sign switching' phenomenon. However, due to the limited number of measured planes, the streamwise evolution of the vortices is not fully understood and current results could only provide a rough idea. Therefore, a series of tests with higher streamwise resolution should be considered in future studies.

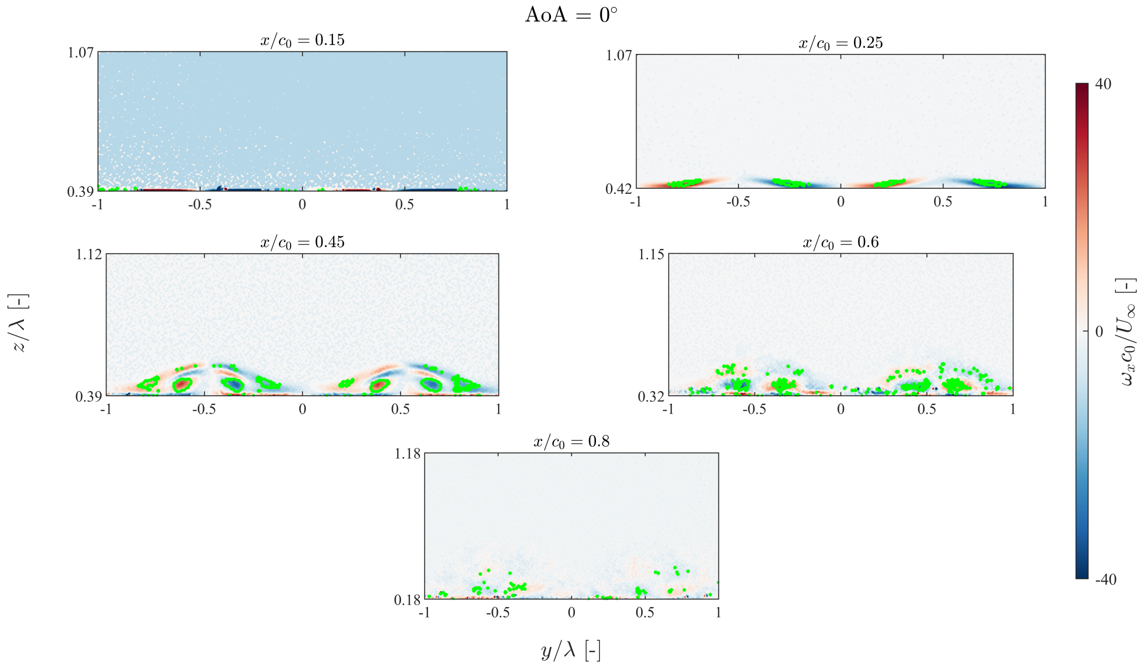

Figure 3.23: Contour plots of non-dimensionalized streamwise vorticity overlaid with iso-lines of Q = 0.001 of A05 wing on the planes x/c_0 = [0.15, 0.25, 0.45, 0.6, 0.8], at AoA = 0°, U_∞ = 5 m/s.

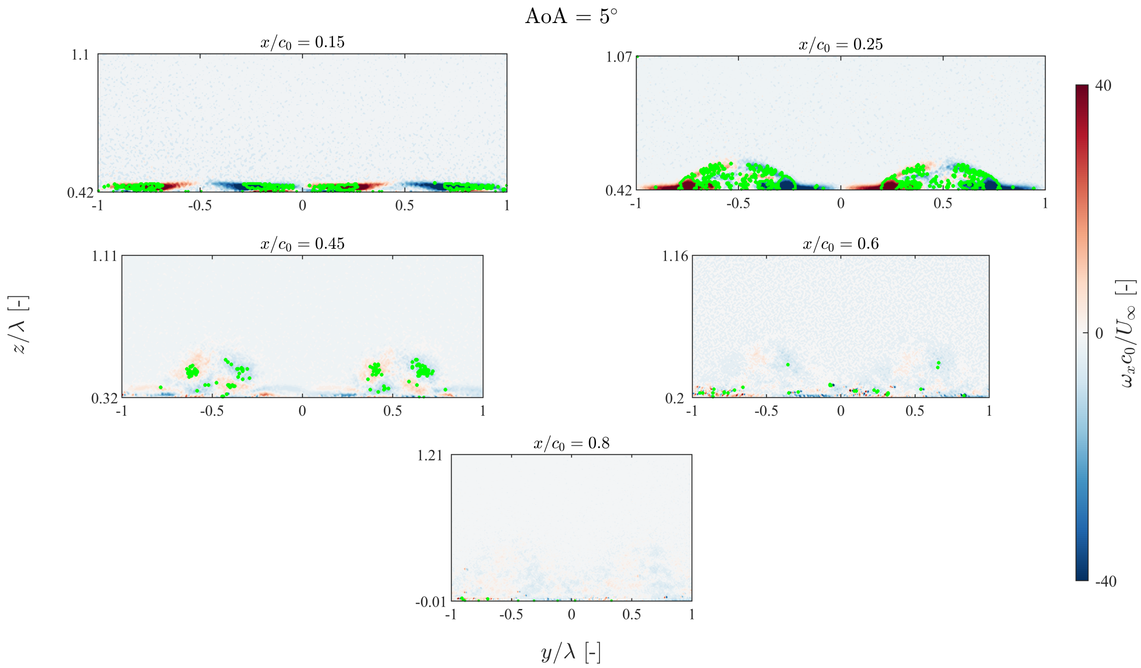

Figure 3.24: Contour plots of non-dimensionalized streamwise vorticity overlaid with iso-lines of Q = 0.002 of A05 wing on the planes x/c_0 = [0.15, 0.25, 0.45, 0.6, 0.8], at AoA = 5°, U_∞ = 5 m/s.

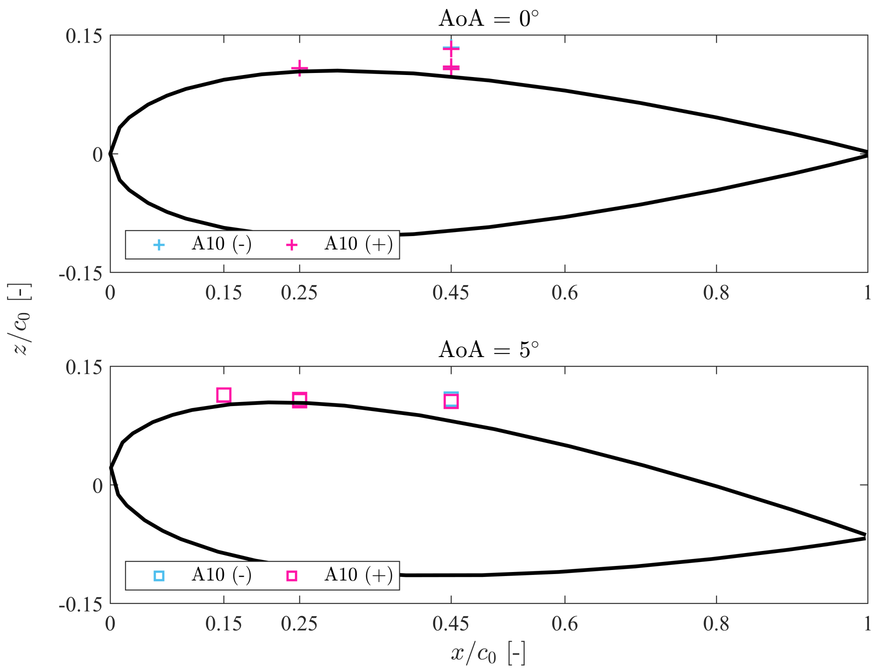

Figure 3.25: Side view of the vortex core distribution of A05 wing on the planes x/c_0 = [0.15, 0.25, 0.45, 0.6, 0.8], at AoA = 0°, U_∞ = 5 m/s.

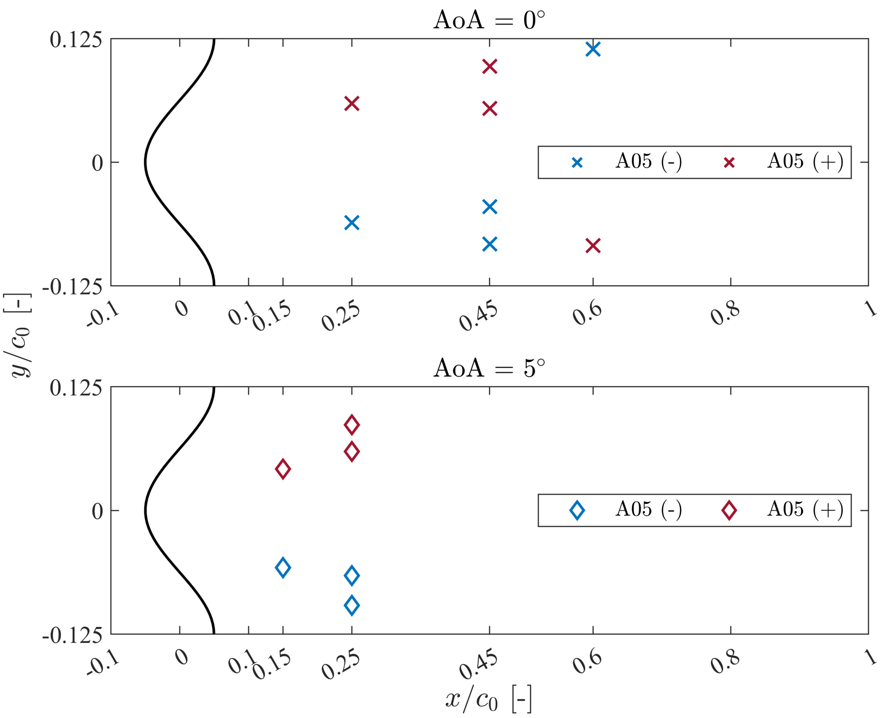

Figure 3.26: Top view of the vortex core distribution of A05 wing on the planes x/c_0 = [0.15, 0.25, 0.45, 0.6, 0.8], at AoA = 5°, U_∞ = 5 m/s.

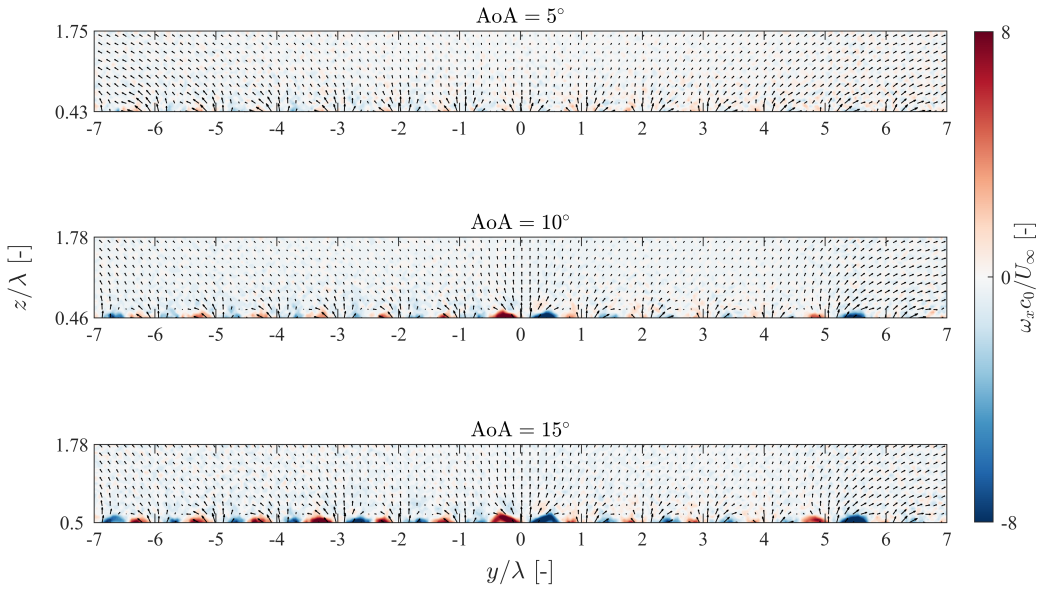

Figure 3.27: Contour plots of mean non-dimensionalized vorticity overlaid by vector fields of the mean velocity of A10 wing on the plane x/c_0 = 0.15, at AoA = 5°, 10°, 15°, U_∞ = 5 m/s, showing every 3rd vector for clarity.

Table 3.2: SC spacing of A10 (U_∞ = 5 m/s).

AoA [°]	5	10	15
SC spacing	-	5λ, 7λ	5λ, 7λ

3.2. Amplitude effect

Increasing the tubercle amplitude while keeping the wavelength the same means that the sweep angle of the tubercle is increased, which would generate higher LEV strength and result in stronger upwash and downwash on the wing. In this section, the effect of the amplitude is examined. The tubercle amplitude becomes twice that of A05 and the results are compared with those of A05.

3.2.1. Stall cell patterns

The higher sweep angle essentially means a stronger spanwise pressure gradient in the interval between a peak and a trough. This leads to a more significant acceleration of the flow on cross-planes, which in turn increases the magnitude of ω_z as shown in Figure 3.27. In addition to the magnitude, another difference compared to the A05 results is that the low-vorticity regions at trough locations shrink. The regions are proposed to be occupied by a group of low-speed flow particles inside the SCs. However, the stronger circulating motion alters the vorticity patterns at the trough locations and The high-vorticity regions on both sides of a trough are not raised. This shift is unlikely to be caused simply by the increased upwash AoA, as similar patterns are not observed in the A05 results when the AoA is 15°. Instead, the circulating motion of the LEV could be the main cause. In Figure 3.2, the unsteadiness result is given. Similar to previous results, the unsteadiness above separated regions is low due to the acceleration effect of the contracted stream tube. The acceleration effect is more obvious in Figure 3.29 where the SC spacing can be determined as before and is summarized in Table 3.2. The SCs occur already at an AoA = 10°, and the patterns remain almost the same until AoA = 15°. Besides the SC spacing is also very similar to that of A05, which means that the SC spacing may not be sensitive to the tubercle amplitude under Re = 33000.

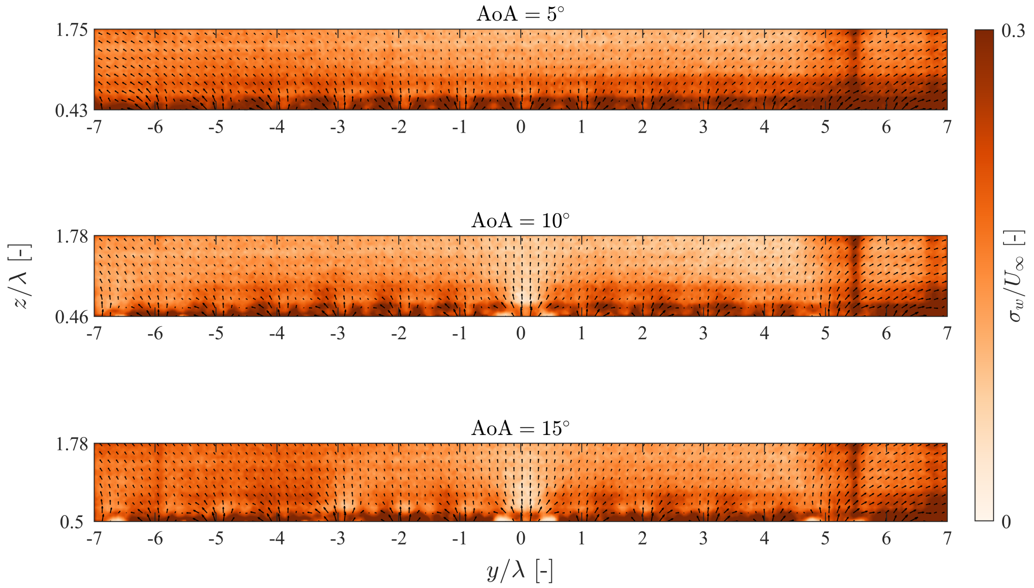

Figure 3.28: Contour plots of non-dimensionalized std of wall-normal velocity of A10 wing on the plane x/c_0 = 0.15, at AoA = 5°, 10°, 15°, U_∞ = 5 m/s, showing every 3rd vector for clarity.

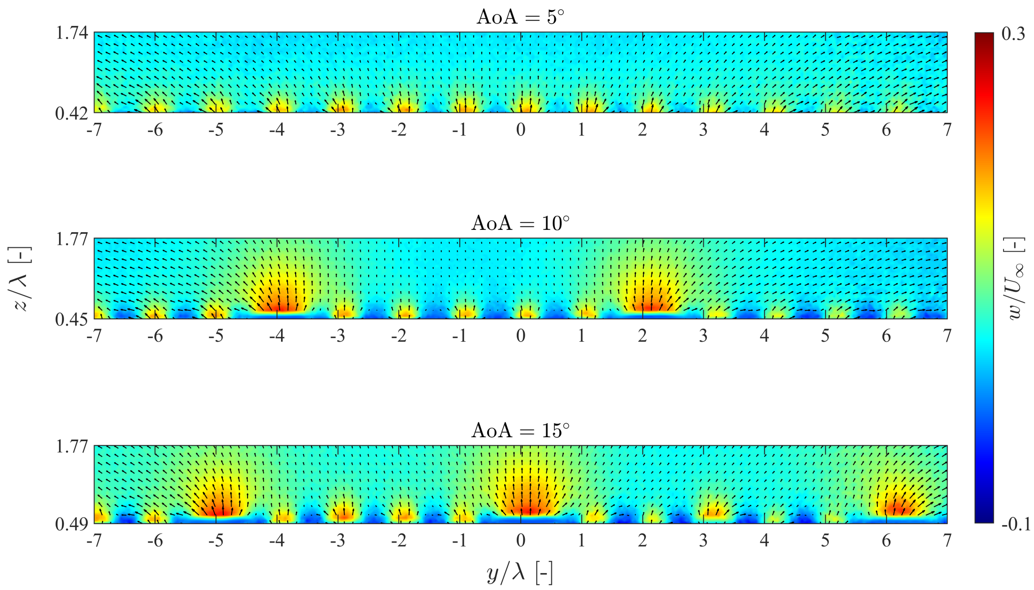

Figure 3.29: Contour plots of mean wall-normal velocity component of A10 wing on the plane x/c_0 = 0.15, at AoA = 5°, 10°, 15°, U_∞ = 5 m/s, overlaid by vector fields of the mean velocity, showing every 3rd vector for clarity.

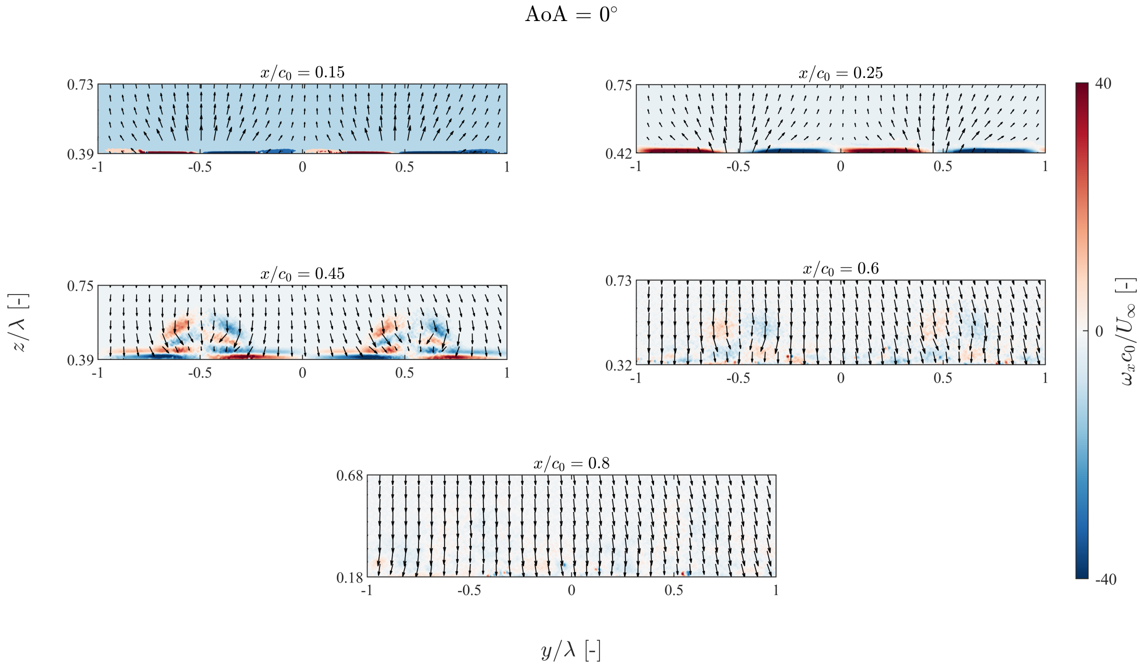

Figure 3.30: Contour plots of mean non-dimensionalized vorticity overlaid by vector fields of the mean velocity of A10 wing on the planes x/c_0 = [0.15, 0.25, 0.45, 0.6, 0.8], at AoA = 0°, U_∞ = 5 m/s, showing every 10th vector for clarity.

3.2.2. Velocity and vorticity

In the previous results of A05, the flow patterns become already chaotic at downstream planes in both post- and deep stall states and less information can be extracted. Therefore, only the pre-stall state, where AoAs are 0° and 5°, is discussed. Flow patterns of both cases are very similar to the A05 cases, whereas the separation occurs earlier. At AoA = 0°, the high-vorticity regions are confined into narrow regions near the wing and suddenly break down and unsteadiness increases drastically at the location of the third plan, whereas in the A05 case, this happens on the x/c_0 = 0.6 plane. This early separation occurs also for high AoA case and the separated regions become larger as can be seen in Figure 3.32. Besides, the complicated sandwich structures are not observed for the range of AoA tested, which could be attributed to the strong LEV and early separation on the suction side.

The vorticity patterns on the planes close to the LE are greatly changed due to the increased tubercle amplitude. On the first plane, the LEV development is at the early stage and the influences of the increased amplitude can be identified in both Figure 3.34 and Figure 3.36. In the AoA ranging from 0° to 15°, the LEV sheets are close to the wing. Although the SCs have already formed at AoA = 10°, the vorticity patterns in unseparated regions are very similar to the pre-stall results, which is also true for patterns on the second plane. At AoA = 20°, however, a double-arch structure is observed at a trough location, and evolve into a square-shaped arch on the second plane. When AoA further increases, the arch structures occur at all trough locations and the shape is similar to the structure that is first observed on the plane. In other words, the double-arch structures form on the first plane and evolve into square-like arch structures observed on the second plane. The arch structure observed at AoA = 15° on the second shares a similar shape to that observed by Custodio in the dye flow visualization of a tubercled wing with a similar tubercle sweep angle [30]. Besides, the flow patterns of A10 on the second plane, including both vorticity and std, are similar to A05 results of the first plane as shown in Figure 3.12. The flow patterns on the second plane of A05 are different and a large half-spheric bubble can be observed at AoA = 15° in Figure 3.14. Since the occurrence of the square-shaped arch structure for the A10 wing is one plane later than the A05 wing, it can be inferred that the tubercle with increased amplitude could slow down the LEV sheets' evolution due to the high circulation magnitude. The circulation can be regarded as the rotating inertia and the higher its magnitude is, the more resistant the LEV sheet is to changing its shape. Hence, the LE flow pattern of both wings could be interpretable within the same framework, and the order of flow pattern evolution

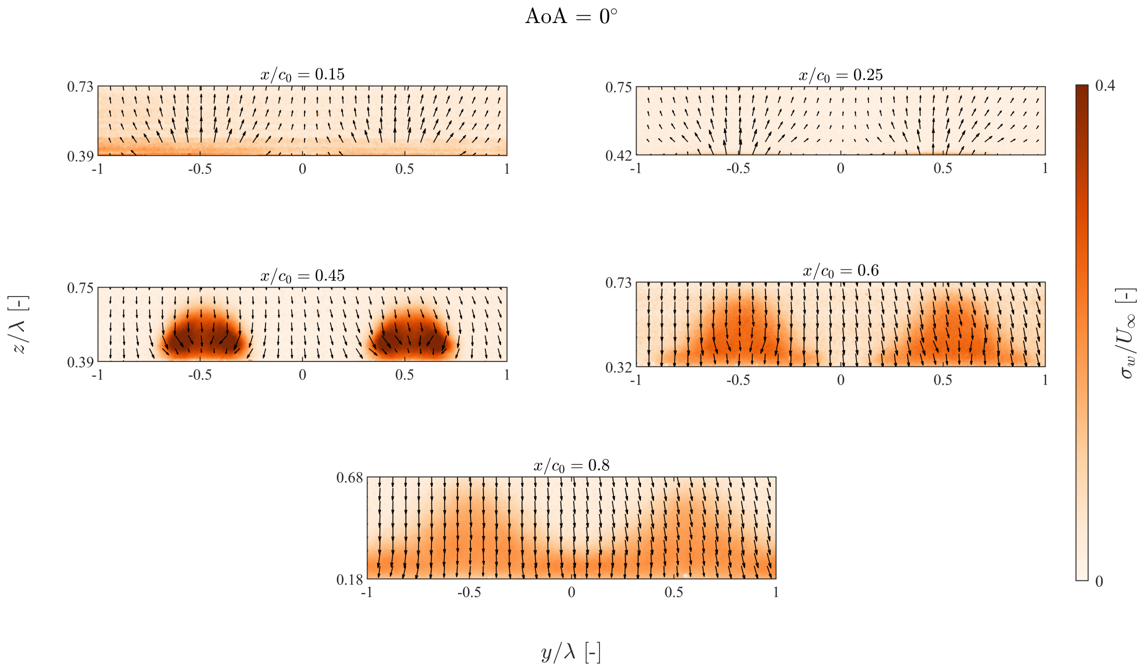

Figure 3.31: Contour plots of non-dimensionalized std of wall-normal velocity of A05 wing on the planes x/c_0 = [0.15, 0.25, 0.45, 0.6, 0.8], at AoA = 5°, U_∞ = 5 m/s, showing every 10th vector for clarity.

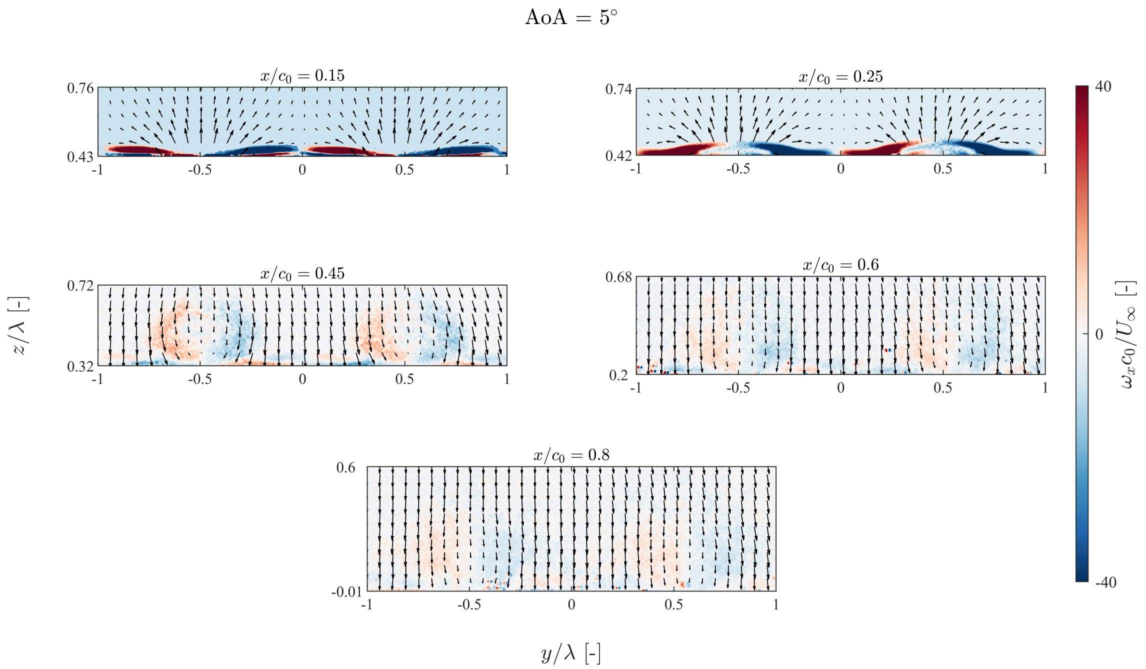

Figure 3.32: Contour plots of mean non-dimensionalized vorticity overlaid by vector fields of the mean velocity of A10 wing on the planes x/c_0 = [0.15, 0.25, 0.45, 0.6, 0.8], at AoA = 5°, U_∞ = 5 m/s, showing every 10th vector for clarity.

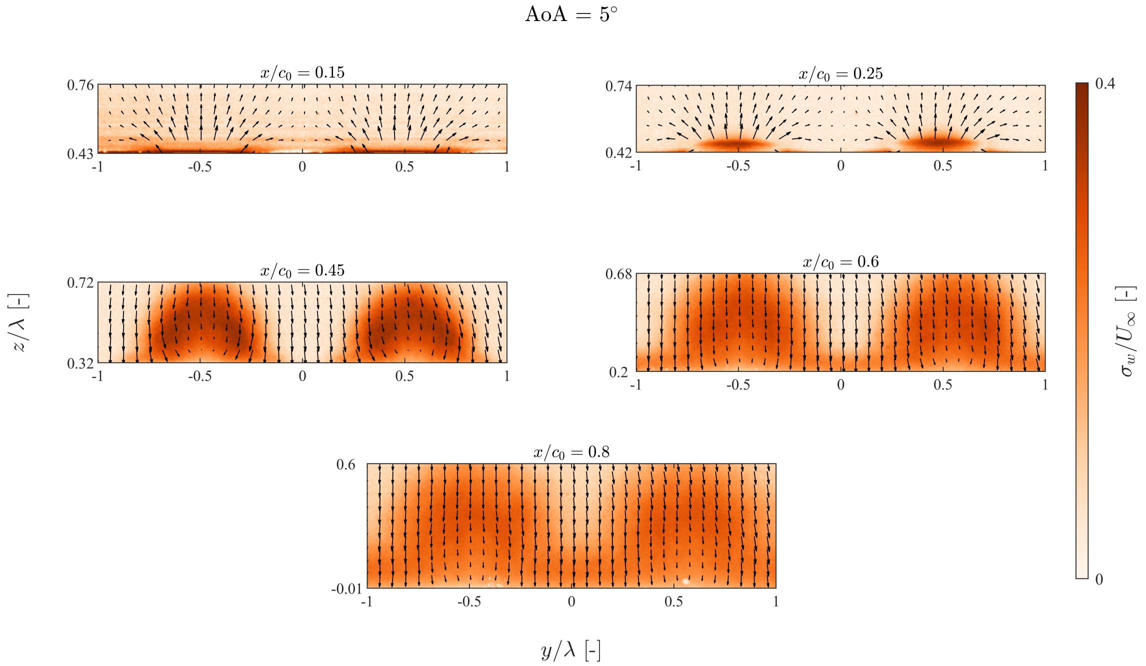

Figure 3.33: Contour plots of non-dimensionalized std of wall-normal velocity of A05 wing on the planes x/c_0 = [0.15, 0.25, 0.45, 0.6, 0.8], at AoA = 5°, U_∞ = 5 m/s, showing every 10th vector for clarity.

should be x/c_0 = 0.15 of A10, A10 x/c_0 = 0.25 of A10 or x/c_0 = 0.15 of A05, and x/c_0 = 0.25 of A05.

3.2.3. LEV strength

Vorticity strength on the first two planes of the A10 wing is quantified by using the circulation based on the line integral approach as discussed before, and the result is given in Figure 3.38. For both planes, the circulation magnitude starts from a non-zero value at AoA = 0° and increases almost linearly up to 30°. The circulation decreases in the downstream plane due to viscosity for most AoA cases and strong unsteady phenomena are observed at AoA larger than 15°.

The comparison between the experimental data and analytical models is given in Figure 3.39. The results from both sources match well, particularly in the slope at pre-stall AoAs. The SCs occur at AoAs larger than 10°, whereas they are not observed in the FOV as shown in Figure 3.34. This could explain why the deviation from model predictions is not very significant at AoA = 10° and 15°. However, this agreement is still considered as a coincidence because of a huge Re gap.

3.2.4. Pre-stall flow patterns

Streamwise velocity gradient

Similar to the vorticity patterns, the results of streamwise velocity gradient is affected by the larger tubercle amplitude as well. At AoA = 0°, the separated flow is observed at x/c_0 = 0.6, where the velocity gradient decreases due to the large region taken by the low-speed flow above the wing surface. However, the separation is not observed until the plane x/c_0 = 0.8. For larger AoA, the transition happens more swiftly; right after the maximum thickness location, the low-speed regions are identified. The stronger upwash at trough locations strengthens the adverse pressure gradient at trough locations and thus facilitates the transition to happen earlier.

Streamwise circulation evolution

The streamwise circulation evolution at AoA = 5° is similar for both wings except that the circulation magnitude is nearly doubled for the A10 wing due to strong vorticity generated along the LE. Besides, the circulation at the rear part is about 1/3 of the circulation at the first plane, while this ratio is about 1/5 for the A05 wing. The circulation of the case AoA = 0° differs from the previous result after the second plane. The vorticity on both sides of a tubercle peak is close to zero and the 'sign switching' phenomenon

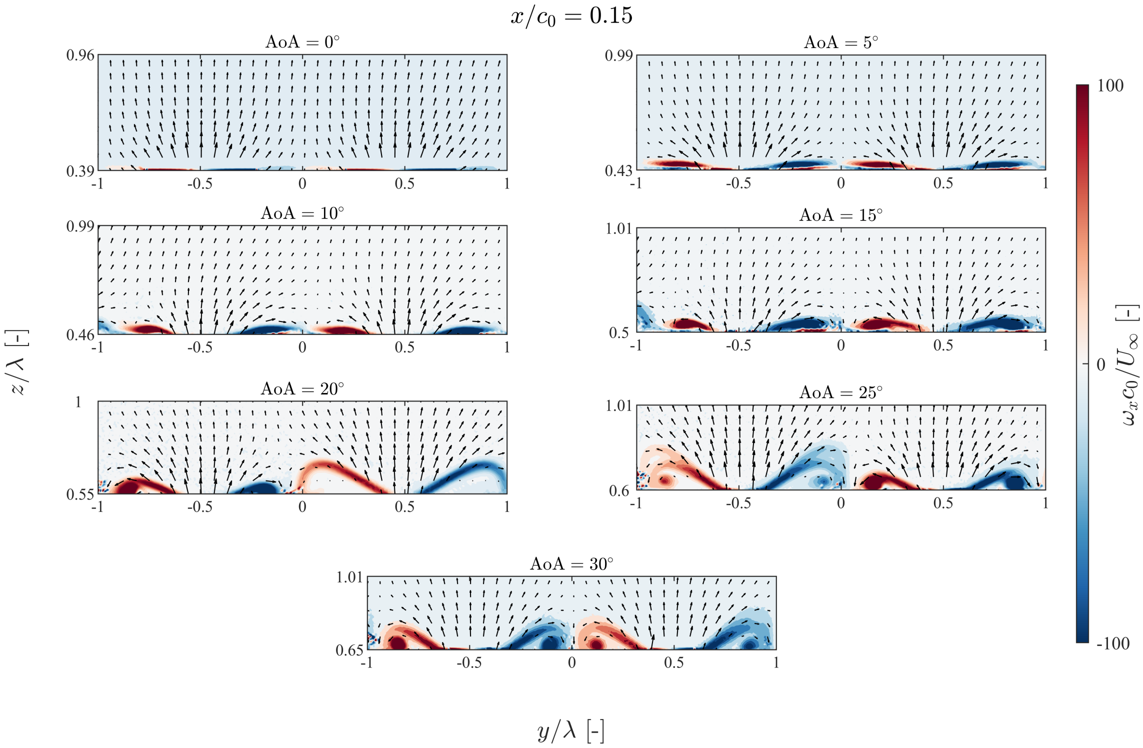

Figure 3.34: Contour plots of mean non-dimensionalized vorticity overlaid by vector fields of the mean velocity of velocity magnitude of A05 wing on the plane x/c_0 = 0.15, at AoA = [0°, 5°, 10°, 15°, 20°, 25°, 30°], U_∞ = 5 m/s, showing every 10th vector for clarity.

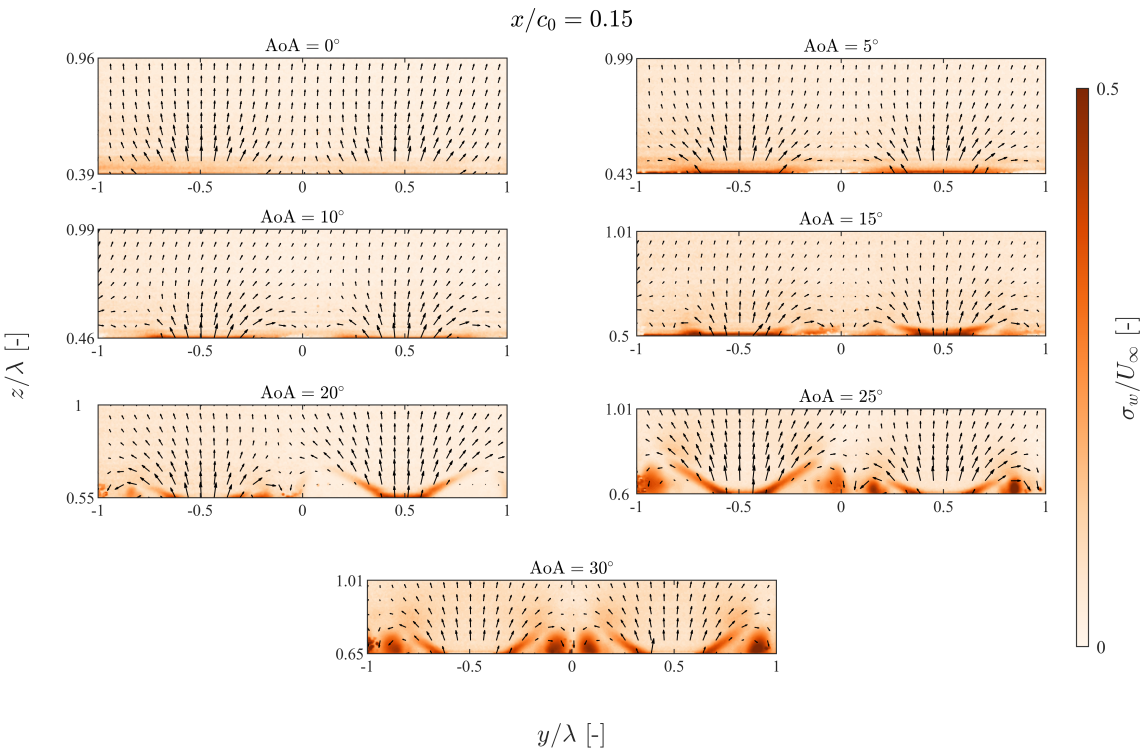

Figure 3.35: Contour plots of non-dimensionalized std of wall-normal velocity of A10 wing on the plane x/c_0 = 0.15, at AoA = [0°, 5°, 10°, 15°, 20°, 25°, 30°], U_∞ = 5 m/s, showing every 10th vector for clarity.

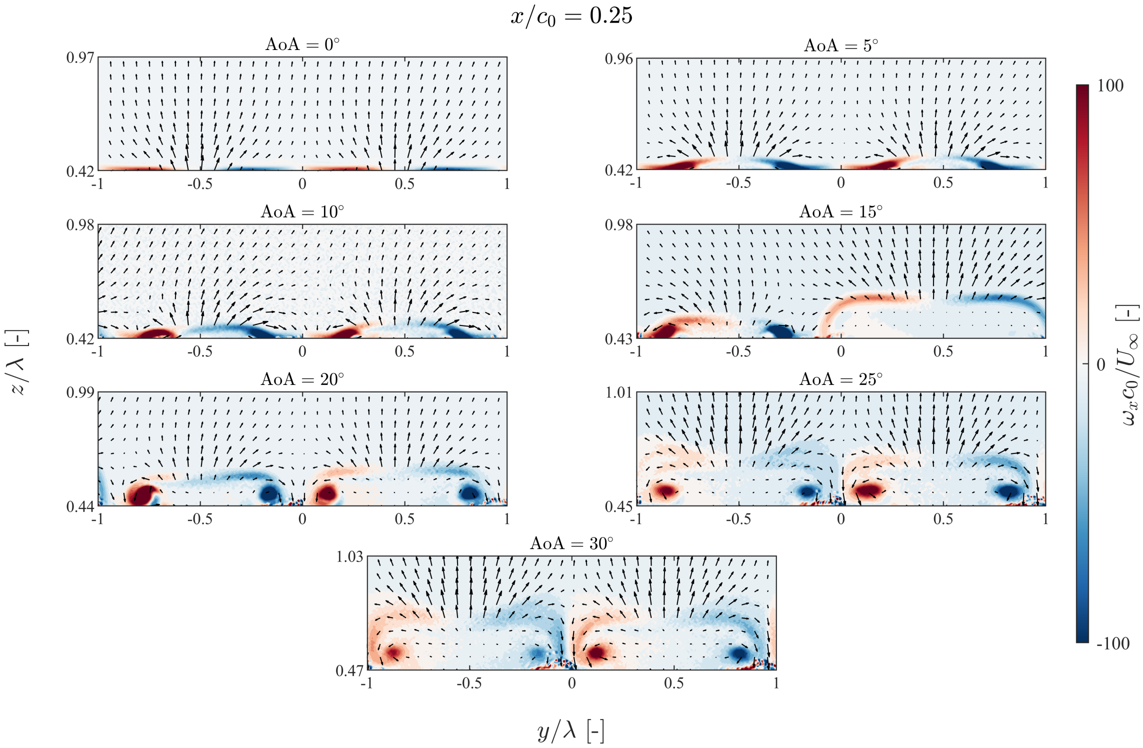

Figure 3.36: Contour plots of mean non-dimensionalized vorticity overlaid by vector fields of the mean velocity of velocity magnitude of A10 wing on the plane x/c_0 = 0.25, at AoA = [0°, 5°, 10°, 15°, 20°, 25°, 30°], U_∞ = 5 m/s, showing every 10th vector for clarity.

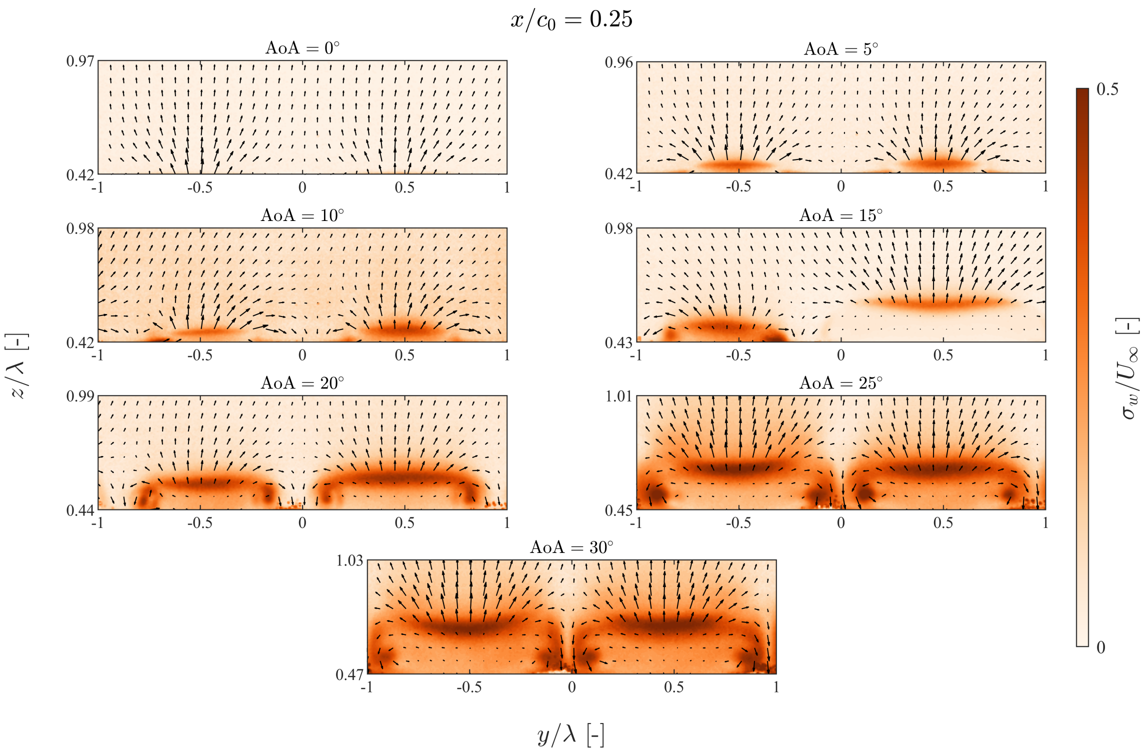

Figure 3.37: Contour plots of non-dimensionalized std of wall-normal velocity of A10 wing on the plane x/c_0 = 0.25, at AoA = [0°, 5°, 10°, 15°, 20°, 25°, 30°], U_∞ = 5 m/s, showing every 10th vector for clarity.

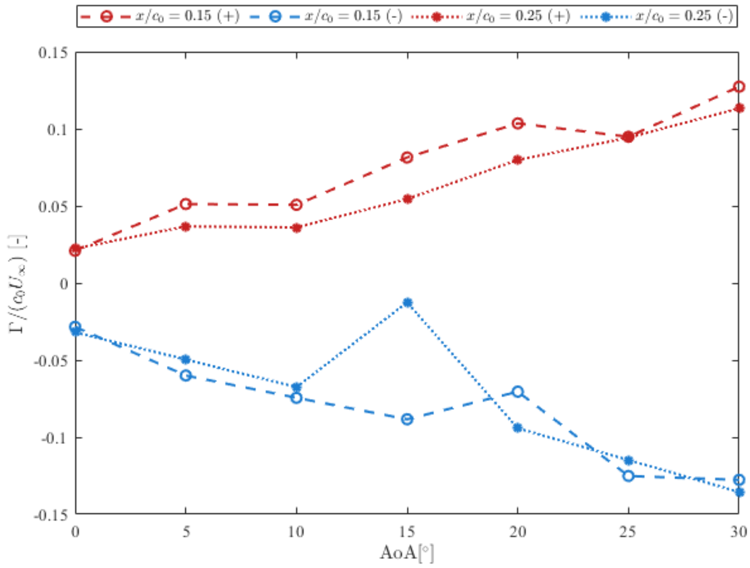

Figure 3.38: Streamwise LEV strength of A10 wing on the planes x/c_0 = 0.15 and 0.25, at AoA = [0°, 5°, 10°, 15°, 20°, 25°, 30°], U_∞ = 5 m/s.

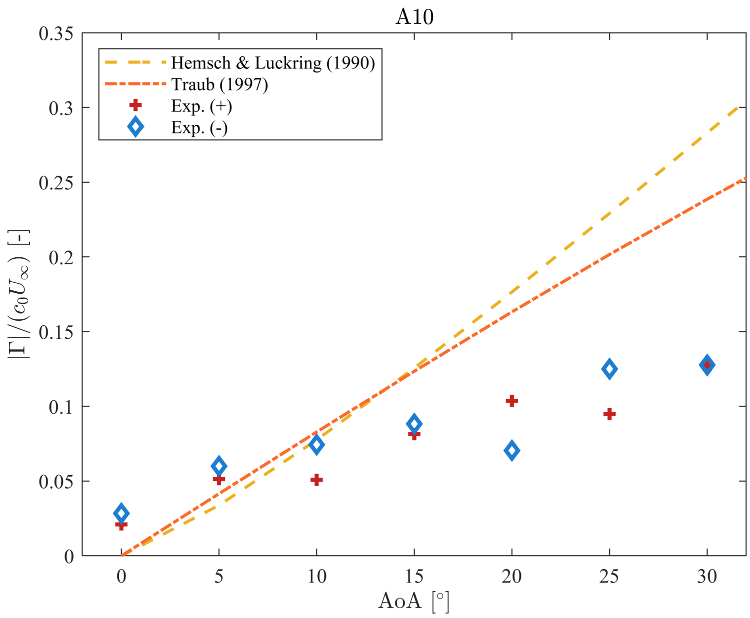

Figure 3.39: Results of streamwise LEV strength obtained experimental data and theoretical estimation of A10 wing on the plane x/c_0 = 0.15 at AoA = [0°, 5°, 10°, 15°, 20°, 25°, 30°].

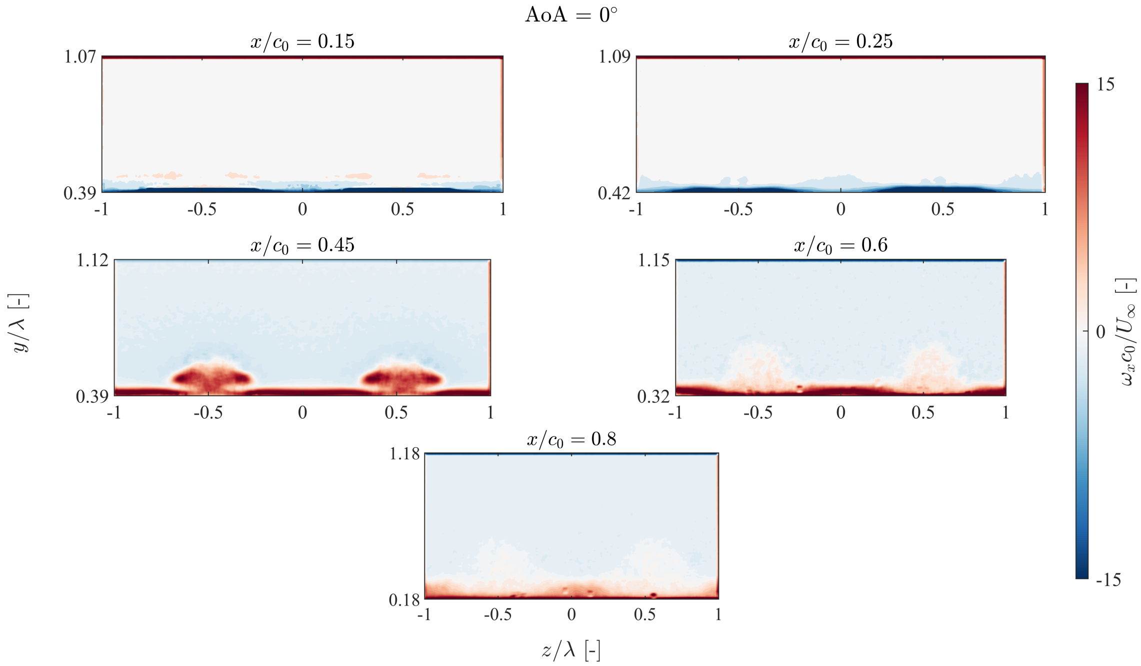

Figure 3.40: Contour plots of streamwise velocity gradient of A10 wing on the planes x/c_0 = [0.15, 0.25, 0.45, 0.6, 0.8], at AoA = 0°, U_∞ = 5 m/s.

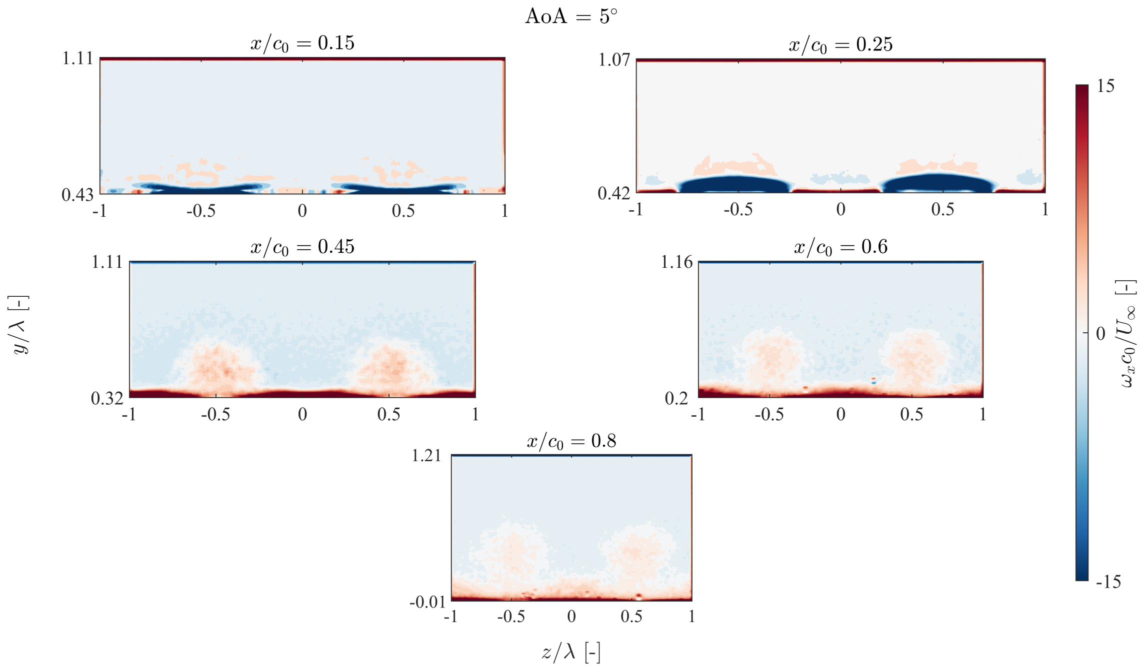

Figure 3.41: Contour plots of streamwise velocity gradient of A05 wing on the planes x/c_0 = [0.15, 0.25, 0.45, 0.6, 0.8], at AoA = 5°, U_∞ = 5 m/s.

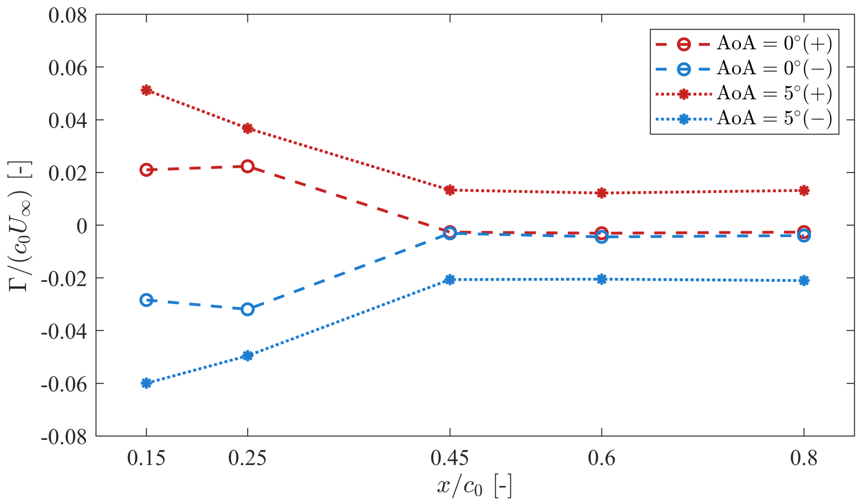

Figure 3.42: Plot of non-dimensionalized streamwise vorticity evolution behind a peak of A10 wing on the planes x/c_0 = [0.15, 0.25, 0.45, 0.6, 0.8], at AoA = [0°, 5°], U_∞ = 5 m/s.

is not observed, which can be ascribed to the early separation. It could be concluded that the increased amplitude can not only increase the circulation magnitude but also enhance its resistance to external factors that might reduce it.

Vortex core distribution

Although the separation occurs earlier and more suddenly for the A10 wing, the vortex identified on the third plane in Figure 3.43 shows an intermittent state of the vortex interaction. Three cores of the same sign are identified on each side of the peak located at x/c_0 = 0. Additionally, on the x/c_0 = 0.45 plane in Figure 3.44, the high-vorticity regions at trough locations form oval-shaped structures and vortex cores are identified on those branches. This characteristic is reminiscent of vortices that undergo breakdown; the concentrated vortex core is split while the circulation magnitude is almost unchanged as shown in Figure 3.42. The structure can be considered as the next stage of development for the three-core structure discussed in the case of AoA = 0°. The side view and top view of vortex distribution are given in Figure 3.45 and Figure 3.46 respectively and the number of vortex cores increases compared to that of A05. The strong LEV sheets could contribute to the vortex breakdown observed.

3.3. Re effect

3.3.1. Stall cell pattern

In Figure 3.47, the distribution of vorticity and std on the first plane of the A05 wing at U_∞ = 2 m/s are given. It is observed that the non-dimensionalized ω_z increases due to a stronger viscosity effect. The SC patterns are affected by this effect as well. When AoA = 5°, the sign of local separation is observed y/λ = -4 in Figure 3.49. The SC pattern occurs at 10° and the SC spacing is 6λ, which is similar to the case of U_∞ = 5 m/s. Further increase of AoA to 15° results in a larger SC covering around 3 tubercles in the interval of y/λ = -5 to -3, with the former SC observed in the center. Although the three separated regions are not connected, it can be imagined they would merge and form a larger separated region downstream. It is surprising that the separation occurs at several neighboring trough locations as the compartmentalization is assumed to be strong based on the vorticity result; the high vorticity is proposed to function as wing fences to prevent further expansion of separated regions [36]. The results here suggest that the compartmentalization effect may not be fully represented by the magnitude of non-dimensionalized ω_x alone. Instead, the convection effect of the high-speed inflow could contribute to the formation of more stable comparting lines and the free stream velocity should also be considered as a significant factor.

Opposite to the results of U_∞ = 2 m/s, the non-dimensionlized ω_x has a lower magnitude in the case of U_∞ = 15 m/s. In addition, the weak viscosity effect modifies the SC pattern shown in Figure 3.52. At AoA = 10 °, a flow structure similar to that observed in the deep stall case in Figure 3.47 is observed from y/λ = -2

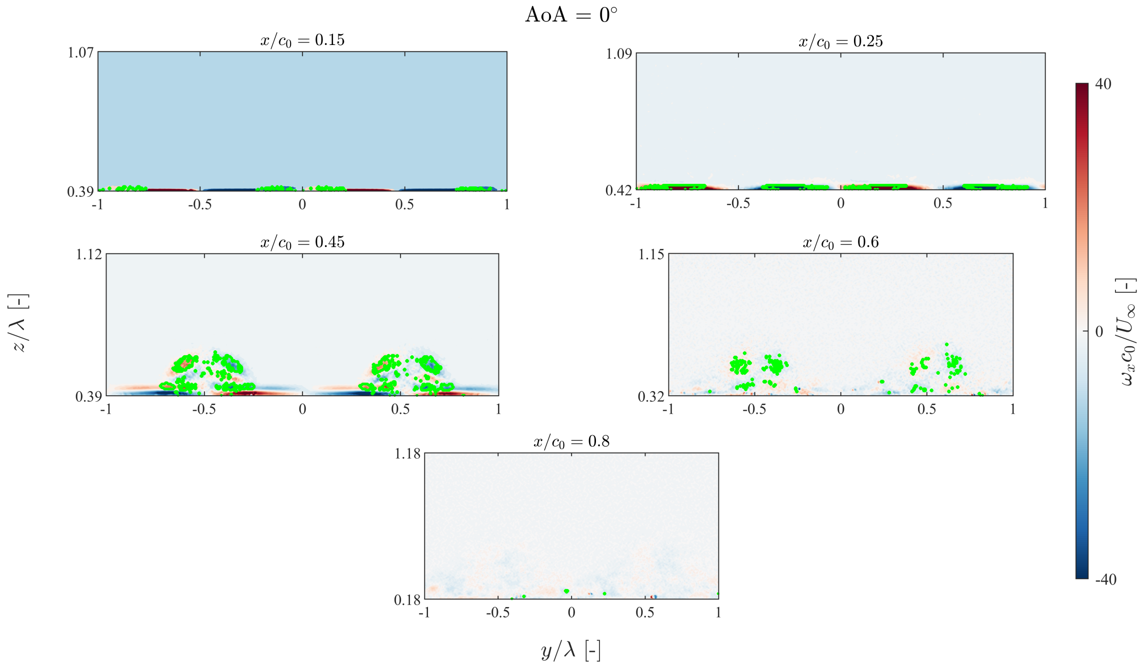

Figure 3.43: Contour plots of non-dimensionalized streamwise vorticity overlaid with iso-lines of Q = 0.001 of A10 wing on the planes x/c_0 = [0.15, 0.25, 0.45, 0.6, 0.8], at AoA = 0°, U_∞ = 5 m/s.

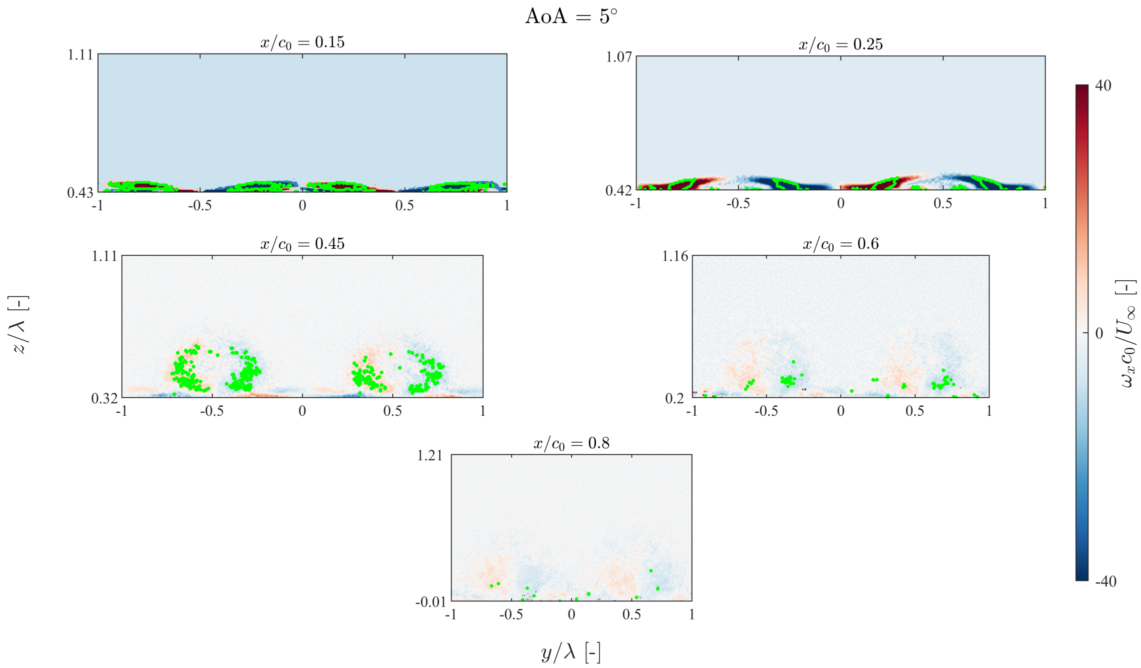

Figure 3.44: Contour plots of non-dimensionalized streamwise vorticity overlaid with iso-lines of Q = 0.002 of A10 wing on the planes x/c_0 = [0.15, 0.25, 0.45, 0.6, 0.8], at AoA = 5°, U_∞ = 5 m/s.

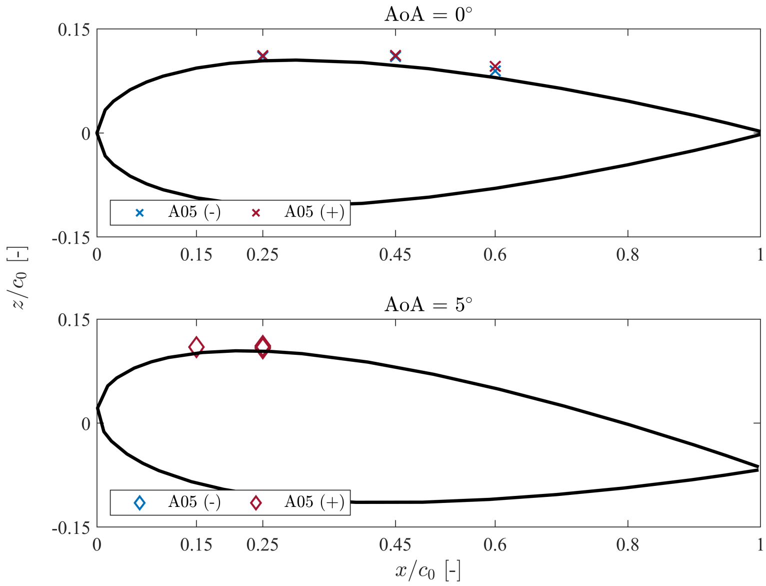

Figure 3.45: Side view of the vortex core distribution of A10 wing on the planes x/c_0 = [0.15, 0.25, 0.45, 0.6, 0.8], at AoA = 0°, U_∞ = 5 m/s.

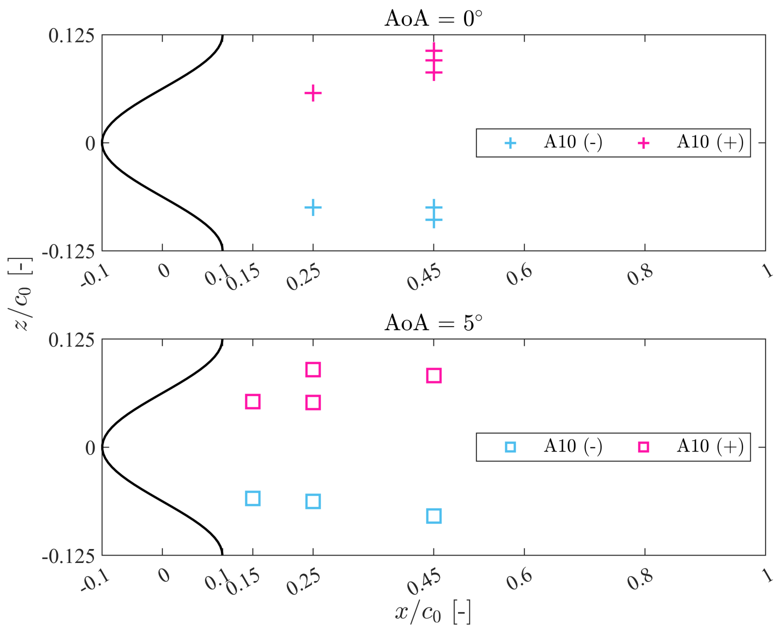

Figure 3.46: Top view of the vortex core distribution of A10 wing on the planes x/c_0 = [0.15, 0.25, 0.45, 0.6, 0.8], at AoA = 5°, U_∞ = 5 m/s.

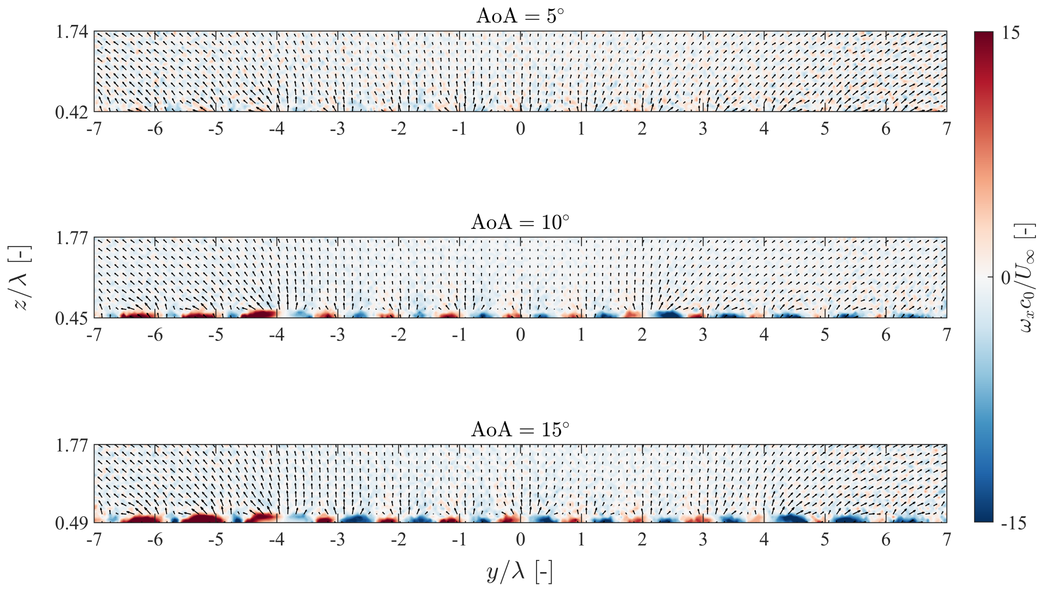

Figure 3.47: Contour plots of mean non-dimensionalized vorticity overlaid by vector fields of the mean velocity of A05 wing on the plane x/c_0 = 0.15, at AoA = 5°, 10°, 15°, U_∞ = 2 m/s, showing every 3rd vector for clarity.

Table 3.3: SC spacing of A05 (U_∞ = 2 m/s).

AoA [°]	5	10	15
SC spacing	-	6λ	-

to 0. The unsteadiness of this region is not low as can be seen in Figure 3.51, meaning that the structure is unstable. In fact, an interesting intermittency phenomenon is found by observing the instantaneous contour plots of w as shown in Figure 3.53. A single SC shifts from y/λ = -1 to y/λ = -2, and then moves to the middle of the span. The phenomenon is also reported in another research [74]. The lifespan of the SC shifting is found to be much longer than that of the vortex shedding, and the unsteadiness of the inflow or the SC is proposed to contribute to the phenomenon [74]. The local AoAs of intermittently separated regions should be close to the stall AoA, which is increased due to the high Re. It is also noticed that the number of spurious points grows in the FOV over time, and this could be ascribed to high inflow velocity, small interrogation window, or seeding intensity. At an AoA of the deep stall, the SC pattern occurs and again the SC spacing is similar to previous cases.

3.3.2. Velocity and vorticity

Flow patterns of U_∞ = 2m/s are given in Figure 3.54, which are found to be similar to the results tested at U_∞ = 5 m/s with an AoA = 10°. In the current results, however, the thickness of the LEV sheet is increased due to strong viscosity effects. Besides, the SC patterns form on the third plane, despite a relatively small AoA and the flow patterns become chaotic at further downstream regions. Moreover, the unsteadiness

Table 3.4: SC spacing of A05 (U_∞ = 15 m/s).

AoA [°]	5	10	15
SC spacing	-	-	5λ, 6λ

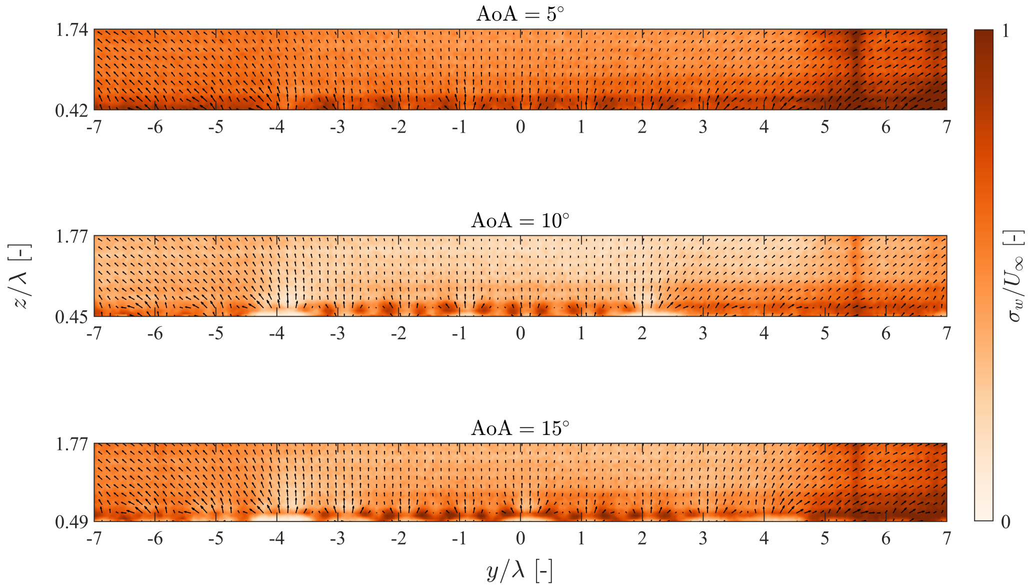

Figure 3.48: Contour plots of non-dimensionalized std of wall-normal velocity of A05 wing on the plane x/c_0 = 0.15, at AoA = 5°, 10°, 15°, U_∞ = 2 m/s, showing every 3rd vector for clarity.

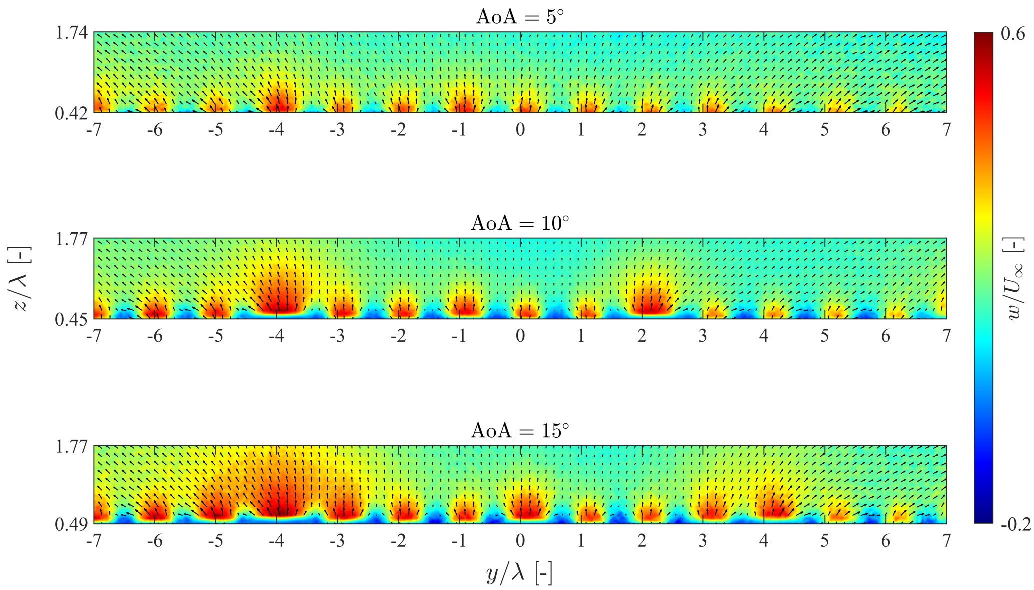

Figure 3.49: Contour plots of mean wall-normal velocity component of A05 wing on the plane x/c_0 = 0.15, at AoA = 5°, 10°, 15°, U_∞ = 2 m/s, overlaid by vector fields of the mean velocity, showing every 3rd vector for clarity.

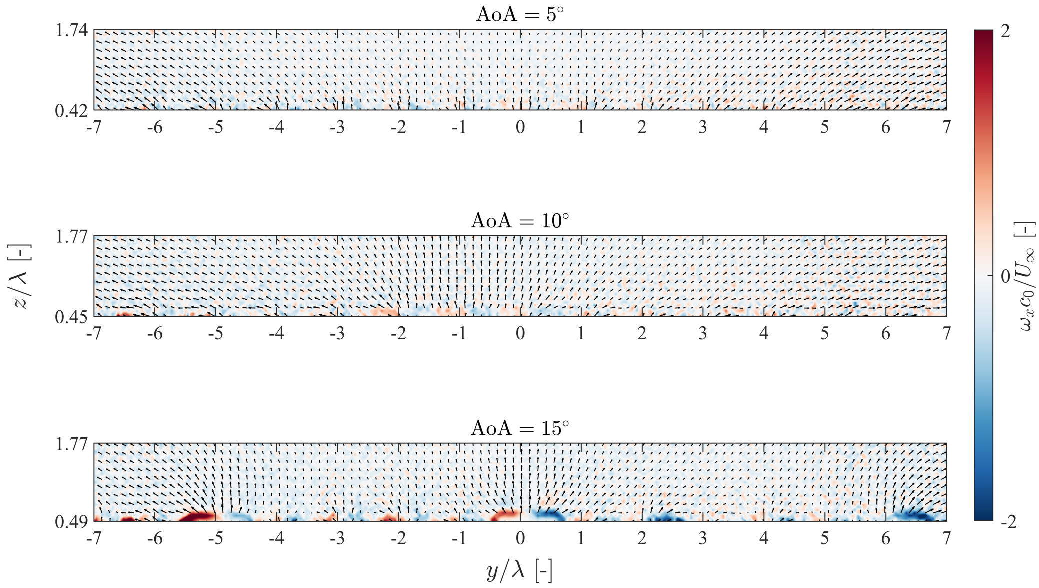

Figure 3.50: Contour plots of mean non-dimensionalized vorticity overlaid by vector fields of the mean velocity of A05 wing on the plane x/c_0 = 0.15, at AoA = 5°, 10°, 15°, U_∞ = 15 m/s, showing every 3rd vector for clarity.

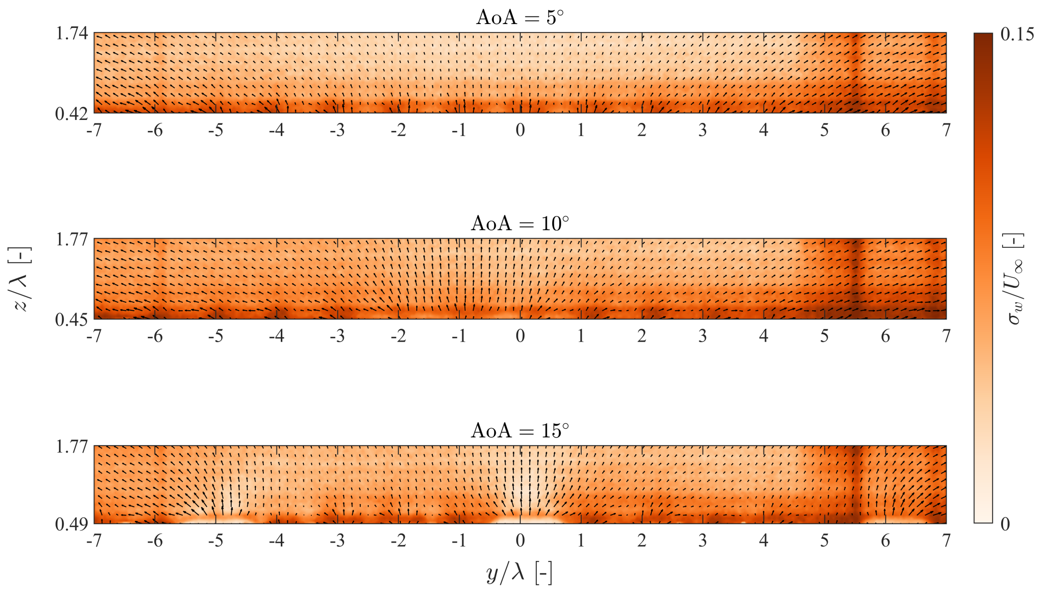

Figure 3.51: Contour plots of non-dimensionalized std of wall-normal velocity of A05 wing on the plane x/c_0 = 0.15, at AoA = 5°, 10°, 15°, U_∞ = 15 m/s, showing every 3rd vector for clarity.

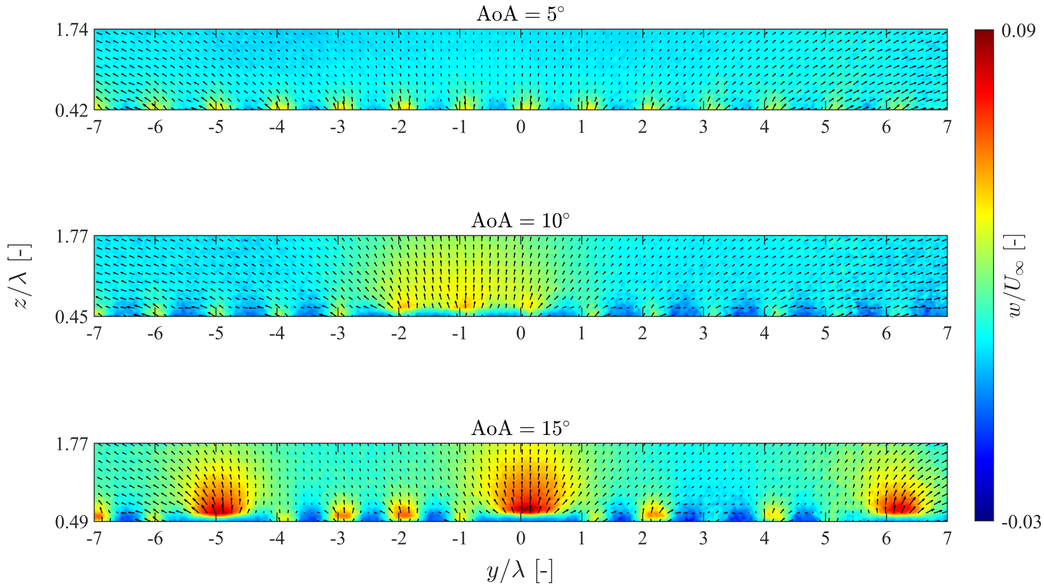

Figure 3.52: Contour plots of mean wall-normal velocity component of A05 wing on the plane x/c_0 = 0.15, at AoA = 5°, 10°, 15°, U_∞ = 15 m/s, overlaid by vector fields of the mean velocity, showing every 3rd vector for clarity.

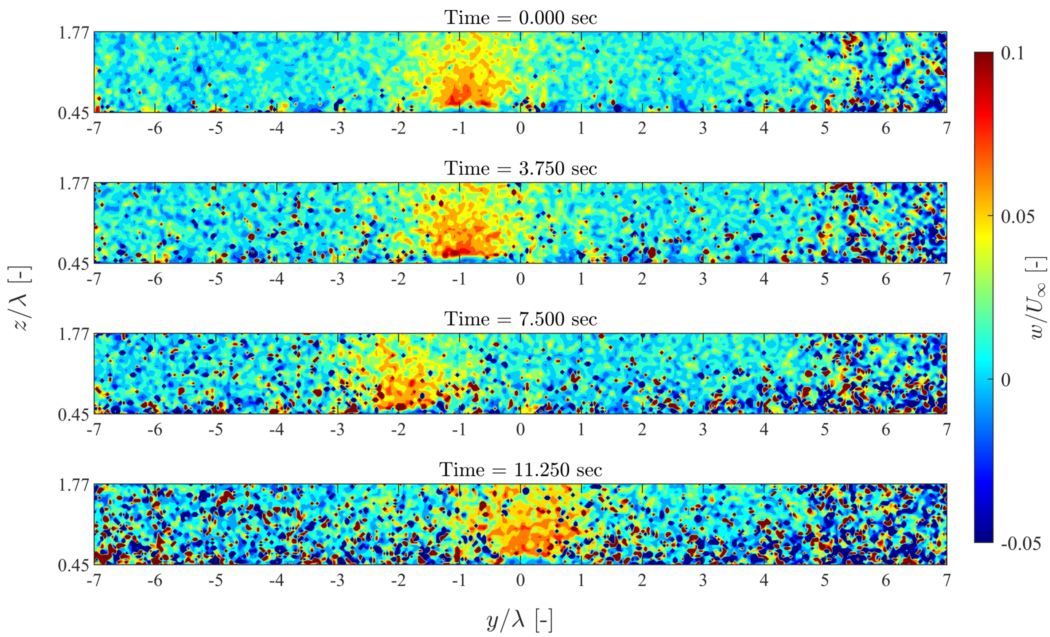

Figure 3.53: SC shifting between y/λ = -2 and 0

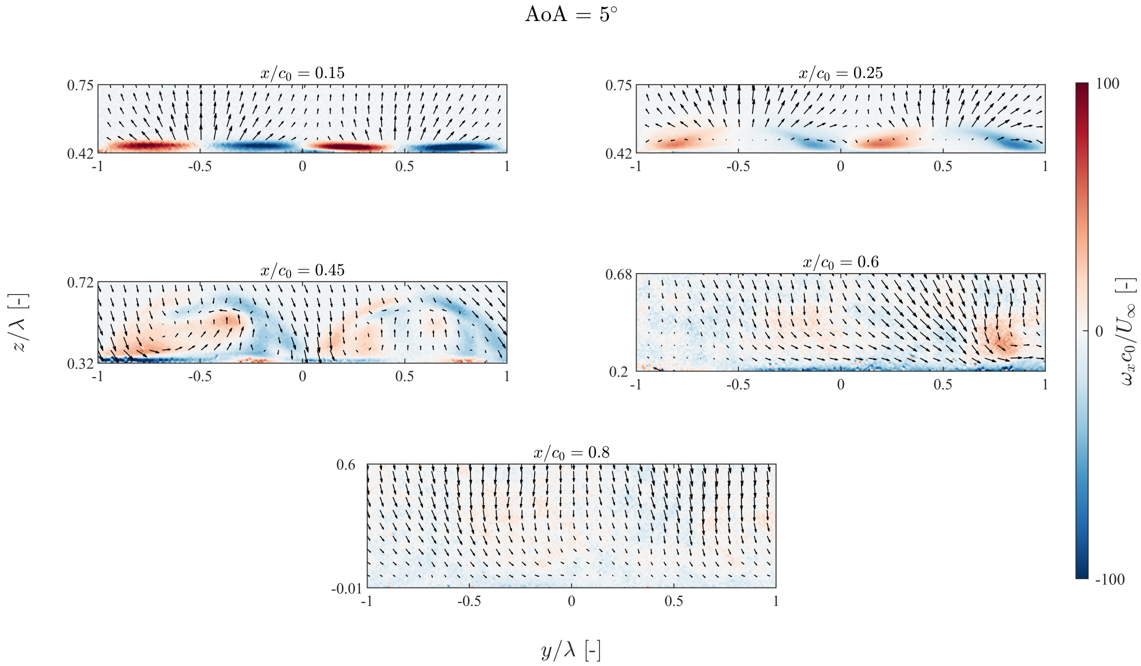

Figure 3.54: Contour plots of mean non-dimensionalized vorticity overlaid by vector fields of the mean velocity of A05 wing on the planes x/c_0 = [0.15, 0.25, 0.45, 0.6, 0.8], at AoA = 5°, U_∞ = 2 m/s, showing every 10th vector for clarity.

in the FOV is high, especially at trough locations and shear layers. A clear Re dependency can also be observed in Figure 3.56, where the inflow velocity is 15 m/s. The LEV sheet thickness is small and the flow patterns are identifiable even until the last plane. The periodic distribution of the std indicates that strong interactions are absent and the broken vortices may be confined to narrow regions.

The observations discussed above can be demonstrated in a more quantifiable way by using the streamwise vorticity evolution as shown in Figure 3.58, with the amplitude effect included as well. Although the general trend is that the circulation would decrease gradually from the LE to TE, the result where the wing is tested at U_∞ = 15 m/s (i.e., Re = 100000) shows a strong unsteady behavior, whereas this is not observed for the cases with higher inflow velocity. The difference in LEV strength can be identified by comparing the non-dimensionalized circulation at the first plane, and it is found that the lower the Re, the higher the circulation. One possible explanation can be that the flow separation behavior around the tubercle LE of finite thickness depends on Re. It can be concluded that the Re effect could modify the LEV strength and thus affect the flow stability on the suction side.

3.3.3. LEV strength

Although Custodio [30] proposed that the LEV strength is not dependent on Re, a strong Re dependency of LEV strength is found in Figure 3.59. At AoA = 5°, LEV strength is calculated for different inflow velocities. It is found that the LEV strength decreases as Re or inflow velocity increases. The reason can be that flow separation behavior is different under different Re. At lower Re, the flow tends to separate earlier after encountering tubercles, and high vorticity regions are generated close to the LE, while for a high Re flow, the separation is postponed and is confined to smaller regions close to the wall. It is also noticed that vortex magnitude is different already at AoA = 5° for the inflow velocity of 2 m/s. Despite a similar Re, the phenomenon is not observed in Custodio's result.

3.4. Summary

In this chapter, the experimental results of A05 and A10 at several streamwise cross-planes are presented. The results regarding both pre-stall and post-stall flow behaviors at U_∞ = 5 m/s are categorized into four groups which are SC patterns, velocity and vorticity, LEV strength, and pre-stall flow patterns. Results of

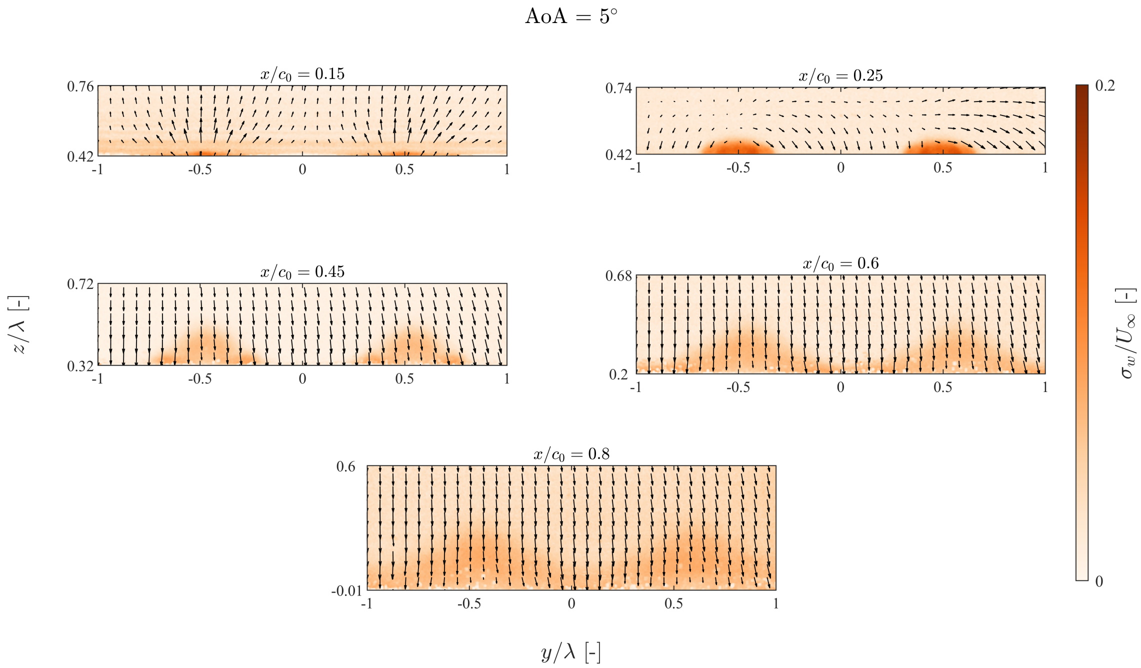

Figure 3.55: Contour plots of non-dimensionalized std of the wall-normal velocity of A05 wing on the planes x/c_0 = [0.15, 0.25, 0.45, 0.6, 0.8], at AoA = 5°, U_∞ = 2 m/s, showing every 10th vector for clarity.

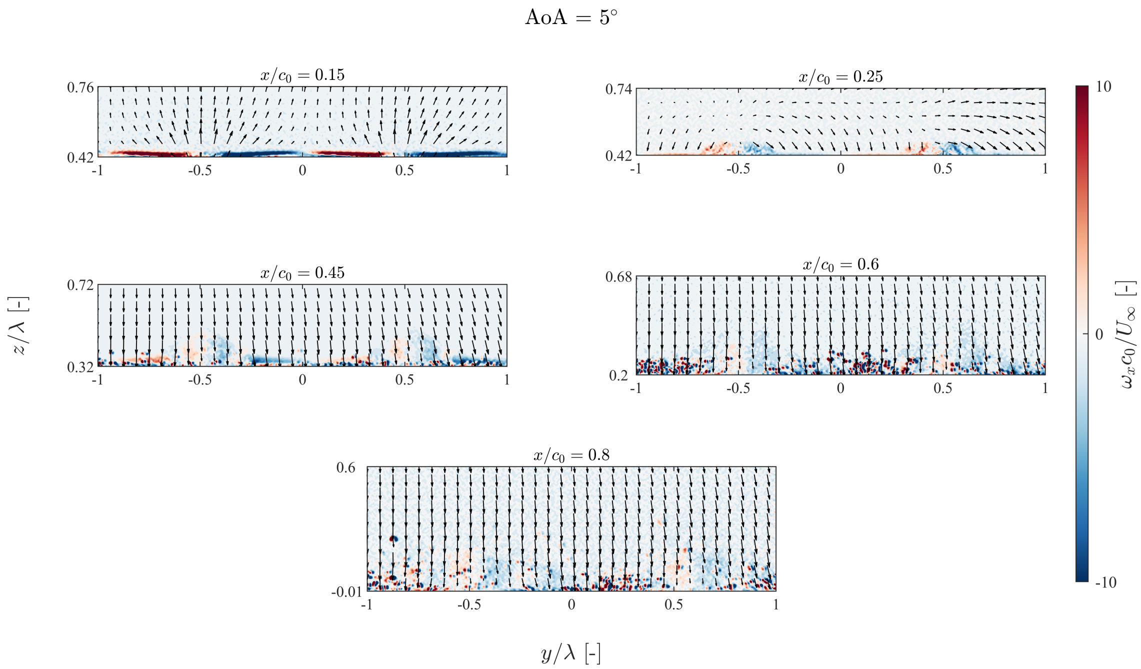

Figure 3.56: Contour plots of mean non-dimensionalized vorticity overlaid by vector fields of the mean velocity of A05 wing on the planes x/c_0 = [0.15, 0.25, 0.45, 0.6, 0.8], at AoA = 5°, U_∞ = 15 m/s, showing every 10th vector for clarity.

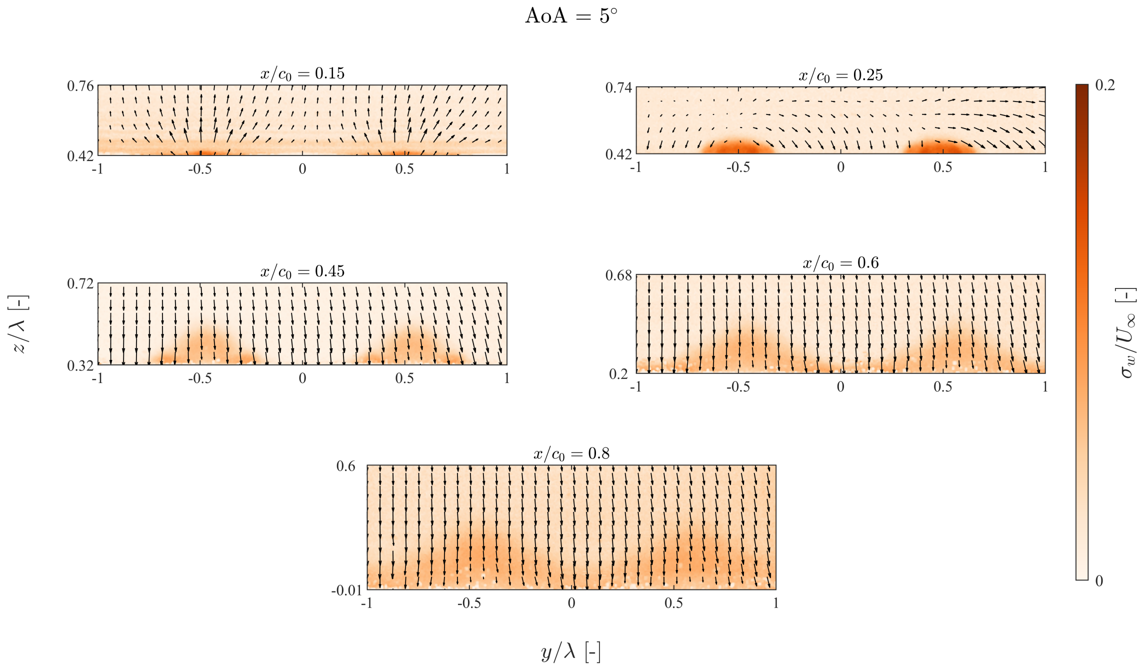

Figure 3.57: Contour plots of non-dimensionalized std of the wall-normal velocity of A05 wing on the planes x/c_0 = [0.15, 0.25, 0.45, 0.6, 0.8], at AoA = 5°, U_∞ = 15 m/s, showing every 10th vector for clarity.

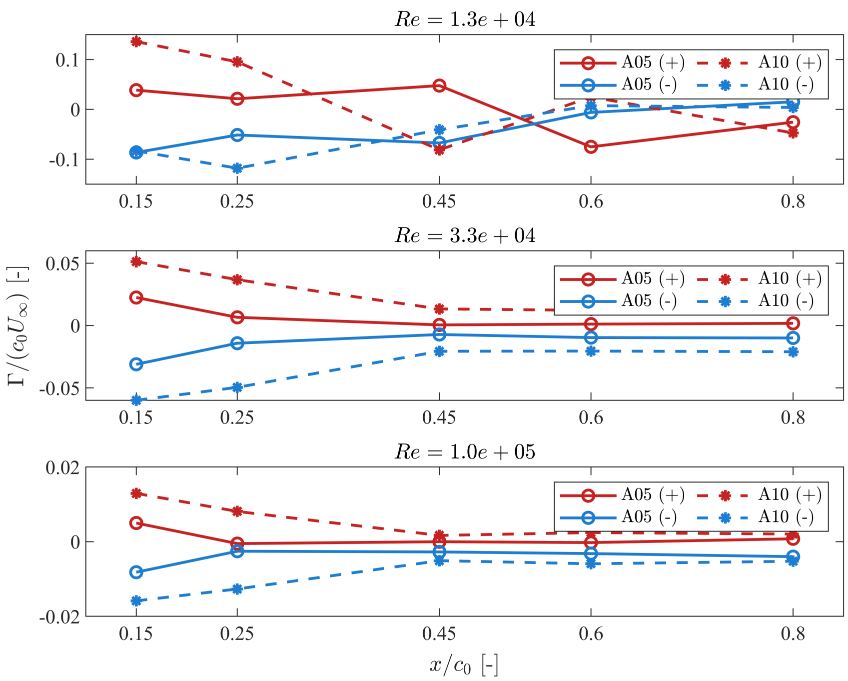

Figure 3.58: Streamwise LEV strength of A05 and A10 wings on the planes x/c_0 = [0.15, 0.25, 0.45, 0.6, 0.8], at AoA = 5°, U_∞ = [2 m/s, 5 m/s, 15 m/s].

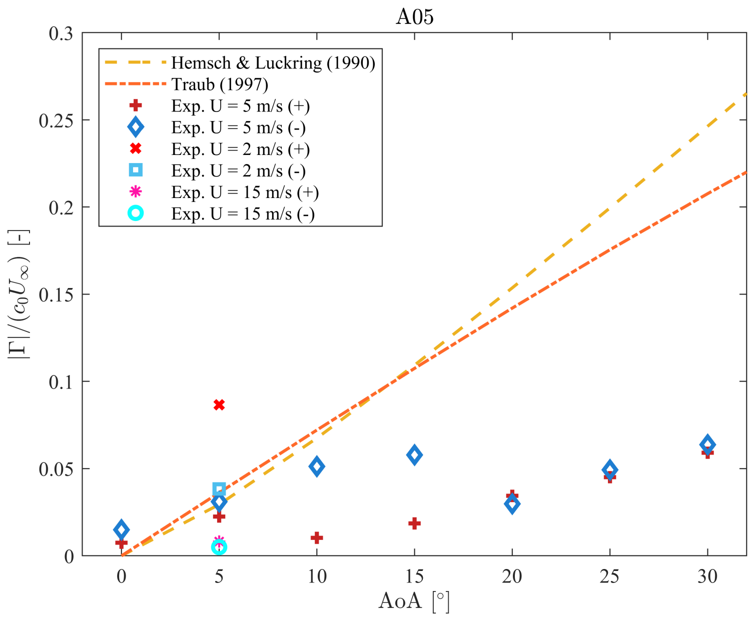

Figure 3.59: Results of streamwise LEV strength obtained experimental data and theoretical estimation of A05 wing on the plane x/c_0 = 0.15 at AoA = [0°, 5°, 10°, 15°, 20°, 25°, 30°] with Re effect assessed at AoA = 5°.

the first three groups of A05 tested at U_∞ = 2 m/s and 5 m/s are also presented and discussed to evaluate the Re effect.

First, the results of A05 are introduced and discussed. The SCs are found to occur on the suction side at AoA = 10° and 15° and can be visualized by using the ω_x contour plots. The regions of high ω_x are found near the locations of SCs, indicating strong shearing caused by upwash effects at trough locations. The shearing layers separate the external flow and the flow inside SCs where the flow velocity is low and velocity fluctuation is small. The formation of SCs decreases the cross-section area of local stream tubes and thus the flow passing above the SCs is accelerated. This feature makes the demonstration of the SC pattern more clearly. The spacing of SCs can then be determined by counting the number of tubercles between two separated trough locations and it is found that the value is 5λ or 6λ which means that the SC spacing is not sensitive to the AoA variation.

More flow details are presented by narrowing the FOV on the regions behind two tubercles in the middle of the wing. Results of velocity and vorticity show that the flow patterns are distinguishable on most planes at a pre-stall AoA while becoming chaotic at high AoAs. The pre-stall pattern is primarily dominated by the interaction between the LEV and the LSB. At a pre-stall AoA, the LEV generated along the LE would form a sheet of high vorticity and travel downstream. In this process, the sheets on both sides of a trough are closer and would deform due to the induced velocity. The ends of the sheets close to the trough location will be lifted and will encounter the LSB located at troughs in the further downstream. The interaction between the LEV sheet and the LSB is hyper-intricate. It is observed that the LEV sheet would climb up to the top of regions occupied by the LSB and contribute to the formation of a strong shearing layer together with vortices emanating inside the LSB. The interaction process would become more complicated once the transition occurs and the flow pattern is chaotic near the rear parts of the wing as the flow separation occurs. In addition to the qualitative observation, the flow pattern evolution is analyzed quantitatively. The information of streamwise flow is obtained by using the continuity law and the flow separation regions can be identified. Besides, the streamwise circulation evolution at a peak location is obtained by applying the line integral method which is more accurate by combining physical knowledge at the wall. The results show that the general trend of circulation would decrease as the flow travels downstream which could be ascribed to the viscous dissipation and diffusion. Additionally, since the vortex interaction also contributes to the evolution, the result is informative about the interaction and supports the analysis of observed velocity and vorticity results. For example, the increase of circulation at x/c_0 = 0.45 corresponds to the observed vortices inside LSB on the same plane. This vortex structure is further supported by the vortex core distribution obtained by using the Q-criterion.

LEV formation mechanism is investigated by considering flow patterns on the first two planes, which are close to the LE. The LEV strength is used as an indicator and the circulation is calculated by using the line integral method. The results are compared with predictions of two empirical models, which were initially developed for estimating the LEV strength of a delta wing, and show good agreement only in the case tested at an inflow velocity of 5 m/s. Strong Re and tubercle geometry dependency affect the LEV circulation greatly. Therefore, despite the similarity between a tubercle and a delta wing in the flow pattern, the underlying LEV vortex generation mechanism is not the same.

The amplitude effect is examined by testing the A10 wing whose amplitude is twice the tubercle amplitude of A05. The increase in amplitude results in stronger circulating motion near the LE and the flow patterns near the LE are greatly modified. However, the SC spacing is found not sensitive to the amplitude increase and is very similar to that of the A05 wing. Due to the strong LEV and upwash effect, the flow structures on the suction side evolve faster and many features observed before are not shown anymore. The separation occurs earlier as well. Flow patterns near the LE share similar characteristics as A05 results. LEV sheets generated by larger amplitude tubercles are believed to tend to maintain their shape longer and the LE flow patterns of both wings could be interpreted within the same framework. By changing the model parameters accordingly, the LEV strength can be predicted and compared with experimental results. Although SCs are observed at AoA = 10° already in a larger FOV, the flow remains unseparated in the FOV where the circulation is calculated, and the experimental data and model prediction match each other until AoA = 15°. Therefore, it can be concluded that the flow mechanism of LE tubercles is the same for both pre-stall cases and post-stall cases as long as the flow remains unseparated behind tubercles. The main feature affecting the streamwise flow patterns is found to be the LEV sheets of higher vorticity, which not only facilitate the transition to happen earlier but also enhance the vortex interaction which leads to the breakdown.

The inflow condition also has influences on the flow pattern. The Re dependency is evaluated by testing the A05 at U_∞ = 2 m/s and 15 m/s, corresponding to Re = 13333 and 100000 respectively. In the results of U_∞ = 2 m/s, the non-dimensional ω_x is higher due to the stronger viscosity effect. However, the SCs start to form already at AoA = 5°, and separated regions extend at higher AoA which is not observed in the case where Re is higher. This difference can be explained by the weak convection effect in the low Re flow. Hence, the result indicates that not only the circulation strength but also the inflow velocity should be considered as the underlying factors of the compartmentalization effect. Different from the low ReT result, the LEV strength of U_∞ = 15 m/s is much lower, whereas the SC is only observed when AoA = 15°. Besides, the streamwise flow fields are more regular which means that the high Re can enhance the stability of the flow.

Part II

Theoretical study

4

Modeling approaches

The complicated flow mechanisms and wide applications of tubercles make it appealing to develop reduced-order models (ROM) to predict the performance of vehicles equipped with tubercled wings. In this chapter, different methods are developed and evaluated for their ability to predict both pre-stall and post-stall characteristics of tubercled wings, together with the effectiveness evaluation of those methods. In Section 4.1, adapted versions of the lifting line theory (LLT) approach and non-linear lifting line theory (NLLT) for a tubercled wing are developed and pre-stall results are compared with experimental data. Following this, conventional panel method is used to further evaluate the effectiveness of the potential-low approaches at a pre-stall AoA. The insights obtained in previous sessions are collected and lead to the attempt of developing a vortex interaction model in Section 4.2. The summary is given in Section 4.3

4.1. Potential flow solution

Previous experimental studies have shown that the LEV plays a significant role in flow evolution. It would be interesting to explore whether its strength can be accurately predicted using potential flow approaches.

4.1.1. Theoretical approach: adapted Gross's model

The original Gross's model inspires the work of applying the NLLT approach to investigate the circulation distribution and predict the circulation analytically. Before considering the case of a tubercled wing, the derivation of Gross's model is first reviewed.

To predict the size of stall cells on a straight wing with the chord c, Gross [53] assumes the spanwise circulation distribution by using the LLT:

$$\Gamma_{\text{straight}}(y) = \Gamma_0 + \Gamma_1 \cos\left(\frac{2\pi}{L} y\right), \tag{4.1}$$

where Γ_0 and Γ_1 are circulation magnitudes for the constant part and sinusoidal part respectively, and L is the assumed stall cell size with its value to be determined. The induced AoA is then calculated from the Biot-Savart law to be:

$$\alpha_i(y) = \frac{\pi}{2U_\infty L}\,\Gamma_1 \cos\left(\frac{2\pi}{L} y\right). \tag{4.2}$$

The circulation can then be expressed in another way by using the Kutta-Joukowski theorem and assuming a linear relationship between C_l and AoA:

$$\Gamma_{\text{straight}}(y) = \frac{1}{2} U_\infty\, c\, C_l = \frac{1}{2} U_\infty\, c\, (C_{l,0} - \frac{\partial C_l}{\partial \alpha} \alpha_i(y)), \tag{4.3}$$

where $C_{l,0}$ is determined by the geometrical AoA. Since the circulation is unique, Equation (4.1) and Equation (4.3) can be equated to find out the expression for the stall cell size L:

$$\frac{L}{c} = -\frac{\pi}{4}\frac{\partial C_l}{\partial \alpha}, \tag{4.4}$$

which shows that the cell size non-dimensionalized by the chord length is proportional to the lift curve slope, and the stall cells only exist when the slope is negative, meaning that the wing stalls.

Following the Gross's model, a pre-stall circulation distribution for a tubercle wing can be assumed simply by replacing the L in Equation (4.1) with the tubercle wavelength λ, which gives:

$$\Gamma_{\text{tubercle}}(y) = \Gamma_0 + \Gamma_1 \cos(\frac{2\pi}{\lambda} y). \tag{4.5}$$

The calculation of induced AoA at each section is the same as that in Gross's model. However, the application of the KJ theorem to obtain the circulation expression is different as the chord length depends on the spanwise location, which means:

$$\begin{aligned}\Gamma_{\text{tubercle}}(y) =& \frac{1}{2} U\, c(y)\, C_l \\ =& \frac{1}{2} U c(y) \left(C_l \, - \frac{\partial C_l}{\partial \alpha} \frac{\pi \Gamma_1}{2U\lambda} \cos\left(\frac{2\pi}{\lambda} y\right)\right).\end{aligned}$$

The chord distribution should be in phase with the assumed circulation distribution, which means that $c(y) = A\cos(\frac{2\pi}{\lambda} y) + c_0$ with c_0 the chord length of the baseline airfoil. Rearranging the expression, we can obtain:

$$\Gamma_{\text{tubercle}}(y) = \frac{1}{2} U\, C_l\, c_0 - \frac{\partial C_l}{\partial \alpha} \frac{\pi \Gamma_1 A}{4\lambda} + \left(\frac{1}{2} U C_l A - \frac{\partial C_l}{\partial \alpha} \frac{\pi \Gamma_1 c_0}{4\lambda}\right) \cos\left(\frac{2\pi}{\lambda} y\right) + \frac{\partial C_l}{\partial \alpha} \frac{\pi \Gamma_1 A}{4\lambda} \cos\left(\frac{4\pi}{\lambda} y\right). \tag{4.6}$$

At a pre-stall AoA, it can be imagined that the bound vortex strength is modulated by the periodicly-distributed tubercles. Therefore, it can be assumed that the contribution from the mode of any frequency higher than $\frac{2\pi}{\lambda}$ is negligible, the fourth term on the left-hand side can be left out. Equating Equation (4.5) and modified Equation (4.6), the circulation magnitudes can be obtained:

$$\begin{aligned}\Gamma_0 &= \frac{1}{2} U\, C_l\, c_0 - \frac{\partial C_l}{\partial \alpha} \frac{\pi \Gamma_1 A}{4\lambda}, \\ \Gamma_1 &= \frac{\frac{1}{2} U A}{1 + \pi c_0 \, \frac{\partial C_l / \partial \alpha}{4\lambda}} C_l.\end{aligned}$$

4.1.2. Numerical approaches: NLLT and panel method

After obtaining the circulation distribution using a theoretical approach, it would be natural to compare the result with that calculated from classical numerical approaches for validation. Both the NLLT and the panel method are used and their formulation is introduced in the subsection.

NLLT

The NLLT was first developed to solve the non-linear problem encountered in the post-stall or complicated geometry. The term 'non-linear' in NLLT indicates that an iterative approach is used to obtain a solution, and the NLLT is essentially applicable to pre-stall conditions. Two types of NLLT are formulated for a tubercled wing case, which are spatila NLLT and spectral NLLT.

The spatial NLLT method is the most commonly used approach, where the wing is discretized into several stations. An initial circulation is first specified for each station to represent the strength of the bound vortex. By definition of the horseshow vortex system, the difference of strength between neighboring stations is the trailing vortex strength which determines the upwash or downwash velocity at stations. The local AoAs at stations are modified by total induced velocity and the bound vortex strength is changed due to the upwash/downwash effect. The new circulation distribution is calculated from the KJ theorem:

$$\Gamma_{\text{temp}} = \frac{1}{2} U_\infty c_n C_{l,n}, \tag{4.7}$$

where c_n is the local chord length, and $C_{l,n}$ is the local lift coefficient determined from the modified AoA. Then, a new system of trailing vortices is generated, which again modifies the AoAs experienced at different stations. In practice, to ensure the calculation stability, a damping coefficient ϵ is used to update the circulation distribution:

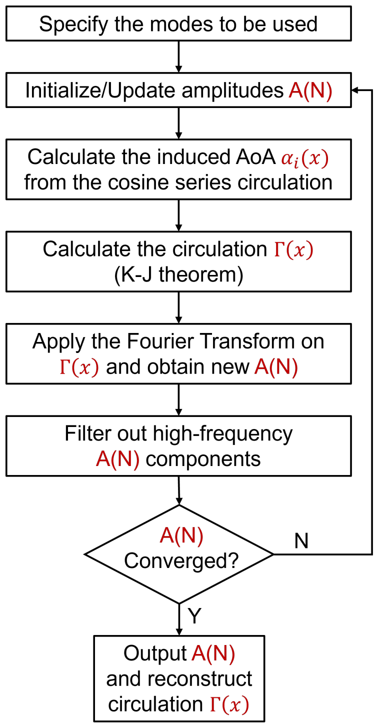

Figure 4.1: Flowchart of the spectral NLLT method.

$$\Gamma_{\text{new}} = \Gamma_{\text{old}} + \epsilon(\Gamma_{\text{old}} - \Gamma_{\text{temp}}). \tag{4.8}$$

When the difference between Γ_{new} and Γ_{old} is smaller than the specified threshold, the calculation converges and the Γ_{new} is the final circulation distribution.

While the spatial NLLT provides a straightforward approach to iterating the circulation distribution in physical space, it is also possible to solve the problem using a spectral method. The spectral NLLT, proposed by Spalart [62] to predict the SC size, assumes that the circulation distribution is composed of N sinusoidal modes with wavelengths that are integer multiples of the tubercle wavelength. Instead of prescribing the circulation at each station, the amplitude is assigned to modes and iterated to find the final amplitude result. The result is used to reconstruct the circulation distribution in the physical space. The procedure is similar to the spatial NLLT and is summarized in Figure 4.1. More details of the code is given in Appendix B.

Panel method

Different from the LLT, the panel method allows the wing to preserve its geometry. The surface of the wing is discretized by panels with each panel assigned two locations for flow singularity and control point; both locations can be the same. To solve the flow field, the singularity strength needs to be obtained. This can be achieved by specifying the boundary condition on the control point and normally it is the no-penetration condition in the context of an inviscid flow. However, it is possible that infinite solutions exist and the unique solution is determined by applying the Kutta condition at the TE. The flow field can then be calculated from the singularity distribution and strength.

There are two types of flow singularities to choose from, one is the vortex and the other is the source/sink. In xflr5, the latter one is used, and source and doublets (i.e., a pair of source and sink very close to each other) are applied on the surface. This selection is based on the developer's experience, and the method is described in detail in early study [75]. The advantage of the choice is that it can represent the thickness effect, which matches the need. The weakness is that the viscosity is completely ignored as the circulation around a source/sink singularity is zero. The viscous effects are incorporated into the method by simply interpolating the inviscid results with viscous data. In addition, the circulatory motion of the flow is not presented in the result. The Kutta condition is implemented at the TE with the help of a wake model.

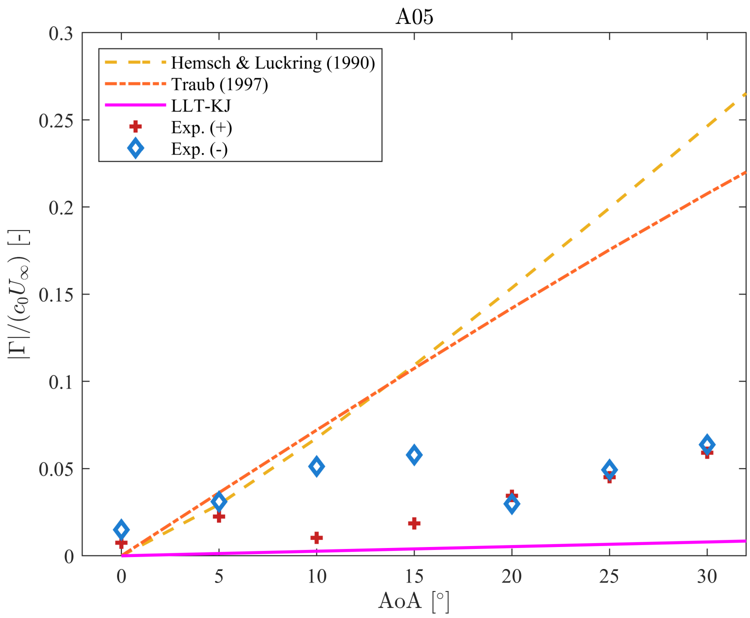

Figure 4.2: Results of streamwise LEV strength obtained experimental data and theoretical estimation of A05 wing on the plane x/c_0 = 0.15 at AoA = [0°, 5°, 10°, 15°, 20°, 25°, 30°].

4.1.3. Model's capability of predicting LEV strength

The Γ_1 obtained in the previous session represents the amplitude of spanwise circulation distribution. Therefore, the maximum circulation difference along the span should be $2\Gamma_1$, corresponding to the circulation difference between a peak location and a trough location. Since the variation in circulation along the lifting line is reflected in the strength of trailing vortices oriented in the streamwise direction, the $2\Gamma_1$ at a pre-stall AoA can be interpreted as the LEV strength as discussed in Subsection 3.1.3. By using the thin airfoil theory, the LEV strength predicted by the LLT combined with the KJ theorem is given in Figure 4.2 and is compared with the experimental data and empirical model prediction. The result of the LLT-KJ model is found to underestimate the LEV in both pre-stall AoAs and post-stall AoAs. The predicted LEV strength is significantly lower than the experimental data, which suggests some flow mechanisms crucial for tubercled wings are not captured in the LLT-type model. In Figure 4.3, a comparison is made to evaluate the performances of LLT-based methods on the A05 wing. Note again that the 'NLLT' here does not mean a post-stall case, rather it refers to the iteration used in the method. The spectral 'NLLT (cos)' result is derived from the spectral 'NLLT (K-J)' result by filtering out high-frequency components. The predicted wavelengths and amplitudes are similar across all LLT-based methods used, indicating that they perform comparably in predicting LEV strength in the pre-stall region. This fact, together with the previous comparison with the experimental result reduces the effectiveness of LLT-based approaches to model flow features of a tubercled wing even at a small AoA.

More factors should be included to develop a ROM for the tubercled wing and one direction to explore is the effect of finite airfoil thickness. In LLT-type models, the effect is ignored by using the 2D airfoil lift polar, and detailed geometry and related flow interaction are not considered. Therefore, it can be expected that by introducing the real geometry of tubercles, the flow pattern should be more similar to that in reality. The panel method can be chosen for this purpose as the whole wing geometry is discretized by panels. In this way, the geometry details, such as the airfoil thickness, and LE curvature, could contribute to the flow field results, which might result in more accurate predictions.

The numerical simulation is conducted in the open-source software xflr5 by using the 3D panel method. Due to the tip effect enforced by default, the wing span is specified as long as possible to mitigate the downwash effect in the middle part of the wing. The circulation distribution is calculated by using the KJ theorem and the result near the wing root is shown in Figure 4.4. The difference between the extreme values labeled can be regarded as the strength of the shed trailing vortex and is calculated to be around 0.0041. The strength estimated from the LLT-KJ model is around 0.0013, which is lower than the panel method result.

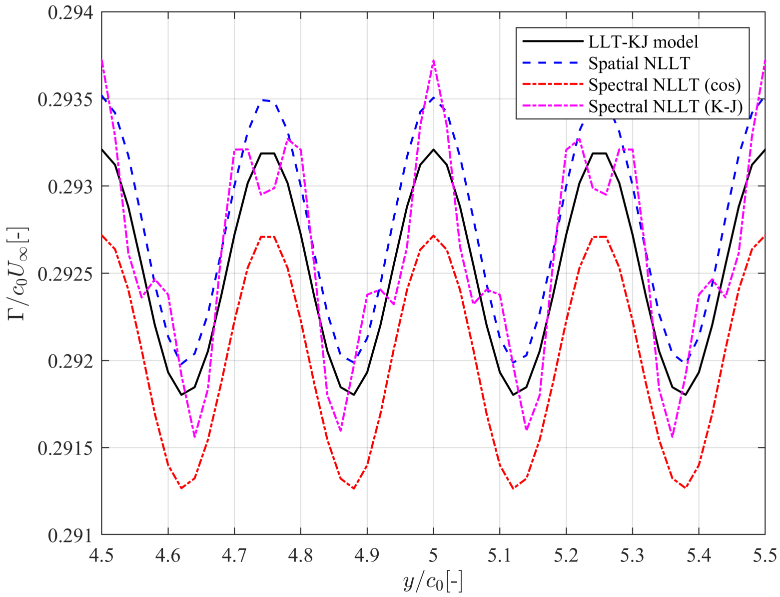

Figure 4.3: Comparison of spanwise circulation distribution predicted by LLT-KJ model, spatial NLLT and spectral NLLT at AoA = 5°.

Therefore, the geometry effect indeed is a contributing factor and should not be ignored in the pre-stall LEV strength estimation. However, the improved result is still much lower than the experimental result. The main cause is proposed to be the numerical setting of boundary conditions in the software. The Kutta condition, which is a dispensable condition for a unique converged result, is only applied along the TE of the wing. Considering the flow near the tubercles, the condition should also be implemented along the LE. This modification would allow the wing to generate stronger streamwise vortices near LE, which is expected to enhance the capability of the panel method to predict the LEV strength.

The primary finding of this part not only evaluates the effectiveness of methods used in previous studies but also provides insights into the flow patterns near the LE. The wing geometry plays a crucial role in generating strong LEV and standard numerical settings may not be sufficient to accurately capture the flow patterns near the leading edge. Overall, the failure of LLT-type models and the panel method puts an emphasis on the significance of the vortices generated near the LE, which should not be ignored in future development of ROM.

4.2. Adaption attempt of Crow's model

In the adapted Crow's model, leading-edge vortices are assumed to extend infinitely in the streamwise direction, both downstream and upstream. The schematic of the vortex system is given in Figure 4.5, where the locations of two LE vortices and the control point of the perturbed vortex segment, marked with red crosses and a red point respectively, are denoted in the figure. The analysis is on the $y-z$ plane as the LE vortex filament is infinitely long in the x direction and thus the displacement of the vortex segment will not change the induced velocity on itself.

If we only consider the velocity in the w direction, the velocities induced on the perturbed vortex segment located at $y = y_n$ by 2 vortex filaments are:

$$
\begin{aligned}
w_1 &= -\frac{\Gamma_{LE}}{2\pi}\frac{y_n - y_1}{(y_n - y_1)^2 + (\frac{b}{2} - \frac{h}{2} + \Delta z)^2};\\
w_2 &= -\frac{\Gamma_{LE}}{2\pi}\frac{y_n - y_2}{(y_n - y_2)^2 + (\frac{b}{2} - \frac{h}{2} + \Delta z)^2}.
\end{aligned}
$$

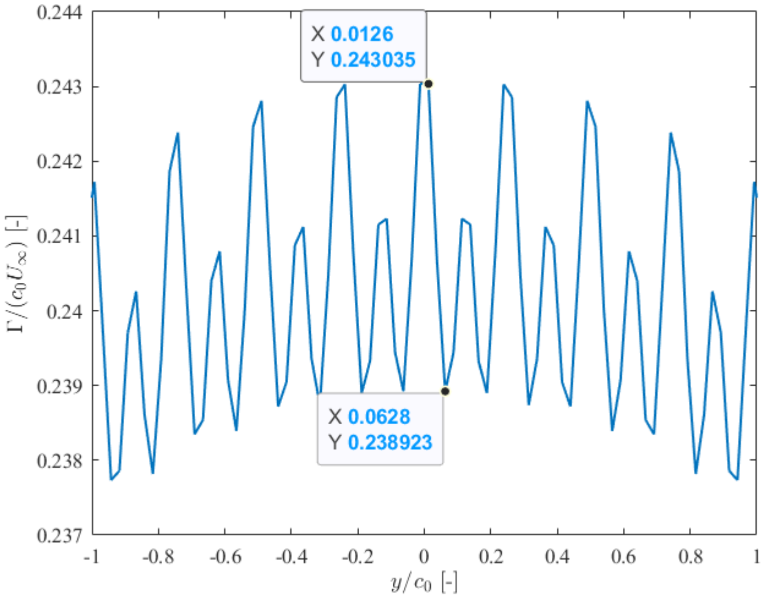

Figure 4.4: Circulation distribution of the A05 with the span of $10c_0$ tested at AoA = 5°. The extreme values near the root are labeled.

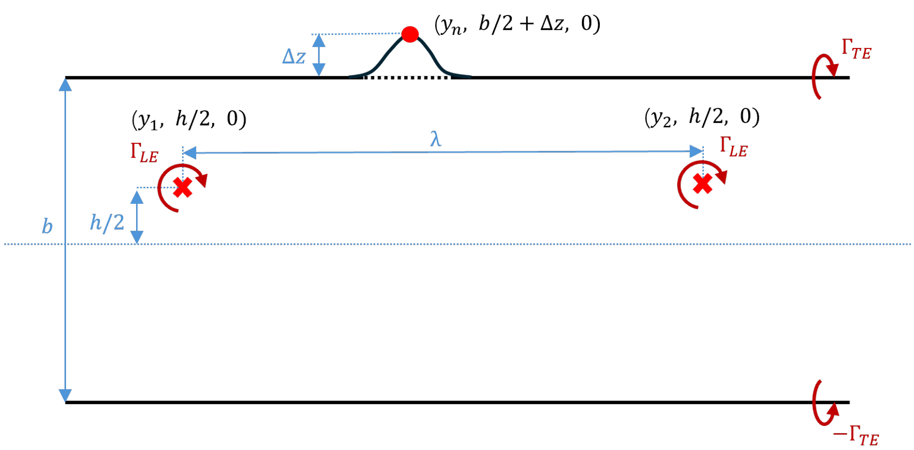

Figure 4.5: Schematic of the vortex system with only 2 leading edge vortices generated from 2 neighboring tubercles considered.

Then, we consider more LE vortices, The LE vortices can be classified into 2 categories: those that are located to the left of the control point (i.e., $y < y_n$), and those that are located to the right of the control point (i.e., $y > y_n$). Therefore, the velocities induced by those LE vortices are:

$$w_{j,L} = -\frac{\Gamma_{LE}}{2\pi}\frac{\Delta x_L}{(\Delta y_L)^2 + (\frac{b}{2} - \frac{h}{2} + \Delta z)^2}, \quad \Delta y_L = y_n - y_j + (j-1)\lambda, \quad j = 1,2,3,...$$
$$w_{j,R} = -\frac{\Gamma_{LE}}{2\pi}\frac{\Delta y_R}{\Delta y_R^2 + (\frac{b}{2} - \frac{h}{2} + \Delta z)^2}, \quad \Delta y_R = y_n - y_j - j\lambda, \quad j = 1,2,3,....$$

The total induced velocity is obtained by summing them up:

$$\begin{aligned} w &= \sum_{j=1}^{\infty}(w_{j,L} + w_{j,R}) \\ &= \sum_{j=1}^{\infty} -\frac{\Gamma_{LE}}{2\pi}\left(\frac{\Delta y_L}{(\Delta y_L)^2 + (\frac{b}{2} - \frac{h}{2} + \Delta z)^2} + \frac{\Delta y_R}{(\Delta y_R)^2 + (\frac{b}{2} - \frac{h}{2} + \Delta z)^2}\right) \end{aligned}$$

Before further analysis, the equation should be linearized. Take the $w_{j,R}$ for example: if the displacement Δz is very small, we have:

$$\begin{aligned} (w_{j,R}(\Delta z))_{linearized} &= w_{j.R}(0) + \left.\frac{\partial w_{j,R}}{\partial y}\right|_{\Delta z=0} \Delta z \\ &= \frac{\Delta y_R}{(\Delta y_R)^2 + (\frac{b}{2} - \frac{h}{2})^2} - \frac{\Delta y_R (b-h)}{(\Delta y_R)^2 + (\frac{b}{2} - \frac{h}{2})^2}\Delta z. \end{aligned}$$

The first term can be regarded as the baseflow and the second term is for the perturbation Therefore, after subtracting the baseflow, the equation can be linearized as:

$$w_{linearized} = \sum_{j=1}^{\infty} -\frac{\Gamma_{LE}}{2\pi}\left(\frac{\Delta y_L}{(\Delta y_L)^2 + (\frac{b}{2} - \frac{h}{2})^2} + \frac{\Delta y_R}{(\Delta y_R)^2 + (\frac{b}{2} - \frac{h}{2})^2}\right)\Delta z \tag{4.9}$$

Now, we turn to the case where quadruplexes are considered. The vortex system is shown in Figure 4.6. Note that the spacing between two vortices in the x direction is denoted as s, and the vorticity strength of the counter-rotating LE vortex is $-\Gamma_{LE}$.

The induced velocity expression can be written out for each pair of LE vortices by considering the sign change of both coordinates and the strength. If we define a function form as:

$$\phi_j(c_1, c_2, c_3) = -\frac{\Gamma}{\pi}\left(\frac{y_n + c_3 + (j-1)\lambda}{((y_n + c_3 + (j-1)\lambda)^2 + (c_1 + c_2)^2)^2} + \frac{y_n + c_3 - j\lambda}{((y_n + c_3 - (j\lambda)^2 + (c_1 + c_2)^2)^2}\right)$$

The contribution of each LE vortex in the quadruplex can be obtained:

$$v_{j,up-left} = \phi_j(\frac{b}{2}, -\frac{h}{2}, \frac{s}{2})\,\Delta z, \quad v_{j,up-right} = \phi_j(-\frac{b}{2}, \frac{h}{2}, -\frac{s}{2})\,\Delta z,$$
$$v_{j,low-left} = \phi_j(-\frac{b}{2}, -\frac{h}{2}, \frac{s}{2})\,\Delta z, \quad v_{j,low-right} = \phi_j(\frac{b}{2}, \frac{h}{2}, -\frac{s}{2})\,\Delta z.$$

The final result for the induced velocity is:

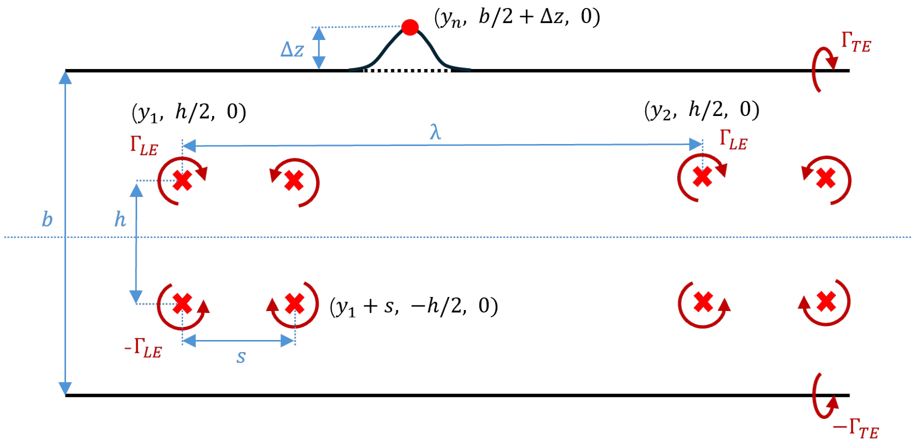

Figure 4.6: Schematic of the vortex system with 4 leading edge vortices generated from 2 neighboring tubercles considered.

$$w = \sum_{j=1}^{\infty}(w_{j,up-left} + w_{j,up-right} + w_{j,low-left} + w_{j,low-right}). \tag{4.10}$$

In practice, parameters b, s, h, Γ_{LE} are to be determined by experimental results, and λ is obtained from tubercle geometry. The ratio $\frac{v}{\Delta y}$ is named as "growth factor". If "growth factor" is denoted as $f(y_n)$. Since the induced velocity is essentially the first time derivation of the displacement Δz, Equation (4.10) can be re-written into:

$$\frac{\partial(\Delta z(y_n, t))}{\partial t} = f(y_n)\,\Delta z(y_n, t). \tag{4.11}$$

The above equation implies that the displacement should grow or decay exponentially. However, the growth rate depends on the spanwise location which means that only the evolution of local perturbation, rather than a global one, can be obtained. Therefore, the system stability is not possible to analyze, and post-stall results cannot be obtained.

4.3. Summary

Theoretical modeling methods are applied to a tubercled wing and their effects are evaluated in the chapter.

The LLT provides a natural approach to depict the circulation distribution with spanwise variation. The sinusoidal variation of chord length is reflected in the circulation calculation using the KJ theorem and the trailing vortices in the horseshow vortex system can be interpreted as the model of downwash and upwash effects. Besides, the trailing vortex strength between a peak location and a trough location can be considered as the LEV strength discussed before, which allows the comparison with the previous results.

The LLT-type models and conventional panel method are found not capable of predicting the flow characteristics even at a pre-stall AoA, due to the absence of strong LEV. This fact further emphasizes the significance and necessity of including the LEV in theoretical modeling. Therefore, the original Crow's model is adapted for a tubercled wing case with LEV considered. However, the stability of the TE vortices is difficult to analyze as the perturbation evolution can only be conducted at a certain local spanwise location, rather than on a global mode. Thus, this modeling approach might not be appropriate as it cannot give any insight into post-stall SC patterns. However, the failure of the model does not mean that the LEV effect sould be omitted in the analysis. Instead, it is one of the main characteristics dominating the flow pattern over the wing and should always be considered to develop any ROM.

Part III

Closure

5
Conclusion

Since their remarkable performance was discovered, tubercled wings have attracted significant attention from both industry and academia. Their exceptional stall behavior makes them an appealing choice in the wind energy field. However, the underlying flow mechanisms remain unclear and continue to interest researchers in fluid dynamics. The goal of this thesis work is to contribute to the collective understanding of the pre- and post-stall flow patterns over the suction side of a tubercled wing, as well as to examine previous ROM approaches used in academia. For those purposes, the following four research questions were explored and answered:

Can a tubercle be considered as a small delta wing?
The LEV generated by spanwise pressure difference along the LE is a distinctive feature of tubercled wings. Although it is widely considered to modify the AoA variation along the span, the generation process is controversial. The tubercles are believed to function similarly to vortex generators, small delta wings, or wing fences. To the author's best knowledge, the discussion on the flow mechanisms is primarily from a qualitative perspective. Even if some arguments are based on previous experimental or numerical results, they are used to oppose, rather than directly support, any opinion regarding the LEV formation mechanism. One challenge facing researchers on this aspect could be that it is difficult to select an indicator of a certain flow control mechanism, which makes it hard to determine the primary contributing factor of LEV. For example, the claim of similarity to vortex generators is refuted due to the latter's large dimension compared to the BL thickness.

In the current thesis work, the LEV circulation is used as an indicator to quantitatively investigate the similarity between a tubercle and a small delta wing. The comparison is made between experimental data and predictions of models for delta wings. The results agree well until SCs are observed in the domain used to calculate circulation. When AoA further increases and the stall occurs, the models' predictions overestimate the strength as the potential flow assumption made in such models is violated. However, this similarity in magnitude and trend in pre-stall and post-stall regions respectively does not mean that the tubercle functions similarly as a small delta wing. The good agreement is regarded as a coincidence after examining the results for the wings tested at different Re and the tubercled wing with a different geometry. Therefore, it can be concluded that a tubercle does not share a similar mechanism as a delta wing regarding the LEV formation. The current thesis work can be viewed as an exploration to study the flow control mechanism of tubercles from a quantitative perspective.

How does the LEV affect flow patterns on the suction side in pre-stall regions?
Wing of moderate Re features LSBs when the AoA is not high. The interaction between the LEV and the LSB is believed to dominate the flow patterns on the suction side of the wing. Although previous numerical studies have demonstrated close-ups of the structures formed in the interaction, the process details are not explained.

Despite limited streamwise resolution, the overall flow evolution is captured in the current thesis work. At pre-stall AoAs, the LEVs are generated along the LE due to the spanwise pressure gradient. Rather than a concentrated vortex core, the LEV is in the form of a vortex sheet, meaning that its degree of freedom is high and the interaction with LSB or other LEV sheets can be complicated. Three elements are identified in the interaction, which are the LEV sheet, the shear layer of the LSB, and vortices generated inside the

LSB. After encountering the LSB, the LEV sheet is lifted and interacts with the LSB shear layer. At a further downstream location, new vortices emanating inside the LSB join the interaction and generate a region of strong shearing together with the LEV, forming a 'sandwich structure'. The new shear layer continues to gain energy from neighboring vortices while growing in size and finally takes over the region occupied by the LEV sheet and LSB vortex before. This pattern shift is accompanied by a 'sign switching' phenomenon observed in the vorticity contour plot as the induced vortex has the opposite sign to neighboring vortices. The discussion above regarding the LEV-LSB interaction can be regarded as a framework in which the flow evolution observed at other pre-stall AoAs can be explained.

What are the influences of amplitude and Re on stall cell patterns?
The formation of SCs along the span at a post-stall AoA is one of the intriguing characteristics of a tubercled wing. In previous studies, the SC size varies from case to case and is very sensitive to experimental or numerical setup.

Both the amplitude and Re dependency are investigated in the thesis work. The effect of amplitude is analyzed by testing the A10 wing while keeping the wavelength the same as the A05 wing. This increase in amplitude leads to stronger circulatory motion near the LE and significantly alters the flow patterns there. Although some structures of the SC disappear, the SC size is found to be not sensitive to the increased amplitude and remains similar to that observed with the A05 wing. Additionally, the SC size remains the same when AoA is increased from 10° to 15° in the post-stall region. The Re dependency is evaluated by testing the A05 at Re = 13333 and 100000 respectively. Regardless of the strong viscosity effect and the higher non-dimensional ω_x observed, the wing experiences an earlier stall, and SCs even extend to neighboring regions. The compartmentalization effect is weak which suggests that not only the streamwise vorticity strength but also the inflow velocity should be considered to understand the effect. When Re is high, the SC pattern is observed at a higher AoA of 15°. The SC sizes of all Re cases are similar, showing their independence on Re. This conclusion can be favorable for ROM development as the Re effect is hard to model theoretically.

What are the limitations of current analytical approaches to model a tubercled wing?
Analytical models are well-suited for predicting the performance of a tubercled wing, as they can rapidly produce results while elucidating the underlying contributing factors. The thesis work focuses on two key features: the LEV strength and the SC size.

The exploration of analytical approaches starts from the LLT-type models where the adaptation for a tubercled wing is relatively simple. By replacing the constant chord length with a sinusoidal chord length distribution, the wavy LE characteristic can be well captured. The derivation based on the idea of the LLT and the KJ theorem gives an analytical formula to estimate the shed trailing vortices and is regarded as the LEV strength in the thesis context. The predictions of the formula match the numerical results produced by spatial and spectral NLLT methods but turn out to greatly underestimate the LEV circulation measured in the experiment. The difference is reduced by applying the panel method, which takes the actual wing geometry into account. However, the discrepancy remains significant and is attributed to the absence of the Kutta condition along the leading edge, which is not accounted for in the simulation tool. If the condition is applied along the LE, strong streamwise vortices can be expected just as the spanwise vortex is enhanced near the TE after introducing the kutta condition at the TE. In summary, the results highlight the limitations of LLT-type models as well as the conventional panel method in dealing with a tubercled wing.

Crow's model is used to model the interaction within the vortex system of a tubercled wing, aiming to provide an analytical way of predicting the SC size based on the wing geometry and viscous flow features. The problem is approached by modeling each pair of LEV sheets behind a tubercle peak as a quadruplex with the wall effect considered. Those quadruplexes are then added between two parallel infinitely long vortex filaments as a modification to the original model. The induced velocity on the vortex filaments is considered to be a perturbation involving modes of various wavelengths and a characteristic wavelength can be identified for SC distribution. However, this modification introduces discrete vortex quadruplexes into the stability analysis. The perturbation is found to depend on the spanwise location and only the evolution of local disturbances can be obtained. Consequently, this modeling approach may be unsuitable because it cannot provide insights into post-stall SC patterns. However, the model's limitations do not suggest that the LEV effect should be ignored in the analysis. On the contrary, the LEV effect is a key factor that significantly influences the flow pattern and must always be considered when developing any ROM in the future.

6 Recommendations

Despite insightful results obtained in the experimental and theoretical studies, there remain questions to answer regarding the flow complexity of a tubercled wing. This chapter will reflect on the methods and results of the current thesis work and provide suggestions for future relevant research.

Measuremnt of all velocity components

While the streamwise velocity gradient is obtained by using the mass conservation law, the obtained results are not instrumental as expected to understand the flow acceleration and deceleration behaviors. Besides, the recirculating region inside an LSB is difficult to confirm. These consequences are caused by that the gradient is calculated in an Eulerian grid rather than the Lagrangian grid following the wing surface. To accurately reconstruct the velocity along the surface, the stereo-PIV can be an appealing choice as the out-of-plane velocity is also measured at each grid point.

Enhancement of streamwise resolution

High-resolution flow fields are achieved only in the cross-sectional planes, while the streamwise resolution remains inadequate due to the limited number of cross-sectional planes. Only five planes are measured in the tests, and this low streamwise resolution significantly hampers the ability to discern the detailed evolution processes, making it impossible to accurately characterize the flow pattern on the suction side. To alleviate the effect, a straightforward approach is to use the same 2D PIV setup while measuring much more crossflow planes. Considering the difficulty of creating the light fence and changing measurement planes, a more promising way would be adopting the 3D PIV, which allows measurements in the whole flow field.

Quantification of LEV strength in other theoretical approaches

By comparing the non-dimensional streamwise vorticity generated by a tubercle and a delta wing of the same size, the tubercle is proposed to not function like a small delta wing in vortex generation. This quantitative way of evaluating the tubercle effect can be extended to examine its similarity to other flow control devices, such as the vortex generator and wing fence. Future comparisons are expected to offer more perspectives to understand the flow control mechanism of tubercles.

Systematic study of Re dependency

The Re tested in the experiments is at the order of magnitude of 10^4 to 10^5, and the Re effect plays an important role in the SC pattern and LEV formation. Previous research focuses more on the Re of 10^5 and a strong Re dependency is neglected. Considering the flow complexity at a low Re regime, it would be meaningful to investigate the Re effect on the flow patterns systematically in the future study.

ROM development with the LEV effect involved

It has been shown that the strong LEV is not reflected in the results of either LLT-type models or the panel method. An attempt to predict the SC spacing is made to incorporate the LEV effect into Crow's model. Although the attempt is not successful, the importance of LEV is clearly conveyed by the theoretical study and the LEV effect should always be considered in future ROM development.

References

[1] International Whaling Commission. *Humpback Whale (Megaptera novaeangliae)*. https://iwc.int/about-whales/whale-species/humpback-whale. Accessed: 2024-08-05. 2024.

[2] NOAA Fisheries. *Humpback Whale (Megaptera novaeangliae) Overview*. https://www.fisheries.noaa.gov/species/humpback-whale/overview. Accessed: 2024-08-05. 2024.

[3] MJ Stanway. *Hydrodynamic effects of leading-edge tubercles on control surfaces and in flapping foil propulsion. Massachusetts Institute of Technology. Dept. of Mechanical Engineering*. 2006.

[4] DT New et al. "Flow control through bio-inspired leading-edge tubercles". In: *Springer Nature Switzerland AG. Part of Springer Nature, University of Edinburgh, Springer, Cham, doi* 10 (2020), pp. 978–973.

[5] Wikipedia contributors. *File:Humpback stellwagen edit.jpg*. https://en.wikipedia.org/wiki/File:Humpback_stellwagen_edit.jpg. Accessed: 2024-08-05. 2024.

[6] Thomas Ridgway Kieckhefer. *Feeding ecology of humpback whales in continental shelf waters near Cordell Bank, California*. San Jose State University, 1992.

[7] Timothy G Leighton et al. "Trapped within a wall of sound". In: *Acoustics bulletin* 29.1 (2004), pp. 24–29.

[8] Dennis M Bushnell et al. "Drag reduction in nature". In: *Annual review of fluid mechanics* 23 (1991), pp. 65–79.

[9] Franke E Fish et al. "Hydrodynamic design of the humpback whale flipper". In: *Journal of morphology* 225.1 (1995), pp. 51–60.

[10] Frank Fish. "Performance constraints on the maneuverability of flexible and rigid biological systems". In: (1999).

[11] Giorgio Moscato et al. "Improving performances of biomimetic wings with leading-edge tubercles". In: *Experiments in Fluids* 63.9 (2022), p. 146.

[12] D. S. Miklosovic et al. "Leading-edge tubercles delay stall on humpback whale (*Megaptera novaeangliae*) flippers". In: *Physics of Fluids* 16.5 (2004), pp. L39–L42. DOI: 10.1063/1.1688341. URL: https://dx.doi.org/10.1063/1.1688341.

[13] David S Miklosovic et al. "Experimental evaluation of sinusoidal leading edges". In: *Journal of aircraft* 44.4 (2007), pp. 1404–1408.

[14] Hugo Carreira Pedro et al. "Numerical Study of Stall Delay on Humpback Whale Flippers". In: *46th AIAA Aerospace Sciences Meeting and Exhibit*. Aerospace Sciences Meetings. American Institute of Aeronautics and Astronautics, 2008. DOI: 10.2514/6.2008-58410.2514/6.2008-584. URL: https://doi.org/10.2514/6.2008-584.

[15] Hamid Johari et al. "Effects of leading-edge protuberances on airfoil performance". In: *AIAA journal* 45.11 (2007), pp. 2634–2642.

[16] Kristy L. Hansen et al. "Performance Variations of Leading-Edge Tubercles for Distinct Airfoil Profiles". In: *AIAA Journal* 49.1 (2011), pp. 185–194. DOI: 10.2514/1.J050631.

[17] Zhaoyu Wei et al. "Aerodynamic characteristics and surface flow structures of moderate aspect-ratio leading-edge tubercled wings". In: *European Journal of Mechanics-B/Fluids* 75 (2019), pp. 143–152.

[18] Wikipedia contributors. *Renewable energy — Wikipedia, The Free Encyclopedia*. Accessed: 2024-08-06. 2024. URL: https://en.wikipedia.org/wiki/Renewable_energy.

[19] L Downer et al. “Whalepower tubercle blade power performance test report”. In: *Wind Energy Institute of Canada, Tignish, PE, Canada* (2008).

[20] Yinan Zhang et al. “Flow control on wind turbine airfoil affected by the surface roughness using leading-edge protuberance”. In: *Journal of Renewable and Sustainable Energy* 11.6 (2019). DOI: 10.1063/1.5116414. URL: https://doi.org/10.1063/1.5116414.

[21] Y. N. Zhang et al. “Aerodynamic load control on a dynamically pitching wind turbine airfoil using leading-edge protuberance method”. In: *Acta Mechanica Sinica* 36 (2020), pp. 275–289. DOI: 10.1007/s10409-020-00939-2. URL: https://ui.adsabs.harvard.edu/abs/2020AcMSn..36..275Z.

[22] Mohamed Ibrahim et al. “Advances in horizontal axis wind turbine blade designs: introduction of slots and tubercle”. In: *Journal of Energy Resources Technology* 137.5 (2015), p. 051205.

[23] Menghao Fan et al. “Numerical and experimental investigation of bionic airfoils with leading-edge tubercles at a low-Re in considering stall delay”. In: *Renewable Energy* 200 (2022), pp. 154–168.

[24] Weichao Shi et al. “Numerical optimization and experimental validation for a tidal turbine blade with leading-edge tubercles”. In: *Renewable Energy* 96 (2016), pp. 42–55.

[25] Fan Wu et al. “Effect of the Wavy Leading Edge to Aerodynamic Performance Improvement in A Nuclear Steam Turbine Last Stage Blade”. In: *ES Energy & Environment* 16 (2022), pp. 47–58.

[26] Michael D Bolzon et al. “Tubercles and their applications”. In: *Journal of aerospace engineering* 29.1 (2016), p. 04015013.

[27] Lihao Feng et al. “Leading-edge tubercles on swept and delta wing configurations”. In: *Flow Control Through Bio-inspired Leading-Edge Tubercles: Morphology, Aerodynamics, Hydrodynamics and Applications* (2020), pp. 111–129.

[28] Jonathan Borg. “The effect of leading edge serrations on dynamic stall”. PhD thesis. University of Southampton, 2012.

[29] Ernst A Van Nierop et al. “How bumps on whale flippers delay stall: an aerodynamic model”. In: *Physical review letters* 100.5 (2008), p. 054502.

[30] Derrick Custodio. “The effect of humpback whale-like leading edge protuberances on hydrofoil performance”. In: *Worcester Polytechnic Institute* 75 (2007).

[31] Chang Cai et al. “Numerical investigations of hydrodynamic performance of hydrofoils with leading-edge protuberances”. In: *Advances in Mechanical Engineering* 7.7 (2015), p. 1687814015592088.

[32] I. Gursul. “Recent developments in delta wing aerodynamics”. In: *The Aeronautical Journal* 108.1087 (2004), pp. 437–452. DOI: 10.1017/S0001924000000269. URL: https://www.cambridge.org/core/product/FEAF8ABFD5602E111D0B8476489320A4.

[33] John T Hrynuk et al. “The effects of leading-edge tubercles on dynamic stall”. In: *Journal of Fluid Mechanics* 893 (2020), A5.

[34] Nikan Rostamzadeh et al. “The formation mechanism and impact of streamwise vortices on NACA 0021 airfoil’s performance with undulating leading edge modification”. In: *Physics of Fluids* 26.10 (2014).

[35] Alex Skillen et al. “Flow over a wing with leading-edge undulations”. In: *Aiaa Journal* 53.2 (2015), pp. 464–472.

[36] Chang Cai et al. “Modeling of the compartmentalization effect induced by leading-edge tubercles”. In: *Physics of Fluids* 34.8 (2022).

[37] Andrey A Sidorenko et al. “Plasma control of vortex flow on a delta wing at high angles of attack”. In: *Experiments in fluids* 54 (2013), pp. 1–12.

[38] Zhaoyu Wei et al. “An experimental study on flow separation control of hydrofoils with leading-edge tubercles at low Reynolds number”. In: *Ocean Engineering* 108 (2015), pp. 336–349.

[39] Michael J Hemsch et al. “Connection between leading-edge sweep, vortex lift, and vortex strength for delta wings”. In: *Journal of Aircraft* 27.5 (1990), pp. 473–475.

[40] Lance W Traub. “Prediction of delta wing leading-edge vortex circulation and lift-curve slope”. In: *Journal of aircraft* 34.3 (1997), pp. 450–452.

[41] Mohamed Gad-el-Hak. “Micro-air-vehicles: can they be controlled better?” In: *Journal of aircraft* 38.3 (2001), pp. 419–429.

[42] Itiro Tani. “Low-speed flows involving bubble separations”. In: *Progress in Aerospace Sciences* 5 (1964), pp. 70–103. DOI: `https://doi.org/10.1016/0376-0421(64)90004-1`. URL: `https://www.sciencedirect.com/science/article/pii/0376042164900041`.

[43] Heesu Kim et al. “Flow structure modifications by leading-edge tubercles on a 3D wing”. In: *Bioinspiration & biomimetics* 13.6 (2018), p. 066011.

[44] BK Sreejith et al. “Experimental and numerical study of laminar separation bubble formation on low Reynolds number airfoil with leading-edge tubercles”. In: *Journal of the Brazilian Society of Mechanical Sciences and Engineering* 42.4 (2020), p. 171.

[45] Shirzad Hosseinverdi et al. “Topology and flow structures of three-dimensional separation bubbles: the effect of aspect ratio”. In: *45th AIAA Fluid Dynamics Conference*. 2015, p. 2630.

[46] Chang Cai et al. “Periodic and aperiodic flow patterns around an airfoil with leading-edge protuberances”. In: *Physics of Fluids* 29.11 (2017). DOI: `10.1063/1.4991596`.

[47] Rafael Pérez-Torró et al. “A large-eddy simulation on a deep-stalled aerofoil with a wavy leading edge”. In: *Journal of Fluid Mechanics* 813 (2017), pp. 23–52.

[48] Steven A Yon et al. “Study of the unsteady flow features on a stalled wing”. In: *AIAA journal* 36.3 (1998), pp. 305–312.

[49] Andy P Broeren et al. “Spanwise variation in the unsteady stalling flowfields of two-dimensional airfoil models”. In: *AIAA journal* 39.9 (2001), pp. 1641–1651.

[50] N Gregory et al. *Progress report on observations of three-dimensional flow patterns obtained during stall development on aerofoils, and on the problem of measuring two-dimensional characteristics*. Citeseer, 1971.

[51] Günter Schewe. “Reynolds-number effects in flow around more-or-less bluff bodies”. In: *Journal of Wind Engineering and Industrial Aerodynamics* 89.14-15 (2001), pp. 1267–1289.

[52] D Weihs et al. “Cellular patterns in poststall flow over unswept wings”. In: *AIAA journal* 21.12 (1983), pp. 1757–1759.

[53] Andreas Gross et al. “Criterion for spanwise spacing of stall cells”. In: *AIAA Journal* 53.1 (2015), pp. 272–274.

[54] Allen E Winkelman et al. “Flowfield model for a rectangular planform wing beyond stall”. In: *AIAA Journal* 18.8 (1980), pp. 1006–1008.

[55] Haley Dell’Orso et al. “Parametric investigation of stall cell formation on a NACA 0015 airfoil”. In: *AIAA Journal* 56.8 (2018), pp. 3216–3228.

[56] A Dropkin et al. “Computation of flow field around an airfoil with leading-edge protuberances”. In: *Journal of Aircraft* 49.5 (2012), pp. 1345–1355.

[57] Ming Zhao et al. “Numerical simulation of flow characteristics behind the aerodynamic performances on an airfoil with leading edge protuberances”. In: *Engineering Applications of Computational Fluid Mechanics* 11.1 (2017), pp. 193–209.

[58] Miles Owen et al. “Towards the understanding of humpback whale tubercles: Linear stability analysis of a wavy flat plate”. In: *Fluids* 5.4 (2020), p. 212.

[59] Steven C Crow. “Stability theory for a pair of trailing vortices”. In: *AIAA journal* 8.12 (1970), pp. 2172–2179.

[60] John D Anderson Jr et al. “Numerical lifting line theory applied to drooped leading-edge wings below and above stall”. In: *Journal of Aircraft* 17.12 (1980), pp. 898–904.

[61] Nikan Rostamzadeh et al. “The effect of undulating leading-edge modifications on NACA 0021 airfoil characteristics”. In: *Physics of fluids* 25.11 (2013).

[62] Philippe R Spalart. “Prediction of lift cells for stalling wings by lifting-line theory”. In: *AIAA journal* 52.8 (2014), pp. 1817–1821.

[63] Frédéric Plante et al. “Stall cell prediction using a lifting-surface model”. In: *AIAA Journal* 60.1 (2022), pp. 213–223.

[64] John D. Anderson. *Fundamentals of Aerodynamics*. 5th. New York: McGraw-Hill Education, 2010.

[65] Usman Butt et al. “Experimental investigations of flow over NACA airfoils 0021 and 4412 of wind turbine blades with and without Tubercles”. In: *Wind Engineering* 46.1 (2022), pp. 89–101.

[66] David Holst et al. “Static and dynamic analysis of a NACA 0021 airfoil section at low reynolds numbers based on experiments and computational fluid dynamics”. In: *Journal of Engineering for Gas Turbines and Power* 141.5 (2019), p. 051015.

[67] A. Sciacchitano et al. *Laboratory Exercise Manual for Experimental Aerodynamics (AE4-180)*. Aerospace Engineering Department, TU Delft. 2023.

[68] Lumibird. *EverGreen ² (70-200 mJ @ 532 nm)*. `https://www.quantel-laser.com/en/products/item/evergreen-70-200-mj-.html`. Accessed: 2024-08-12. 2024.

[69] LaVision GmbH. *Imager sCMOS CLHS*. Tech. rep. Accessed: 2024-08-12. Göttingen, Germany: LaVision GmbH, 2020.

[70] Jewel B Barlow et al. *Low-speed wind tunnel testing*. John wiley & sons, 1999.

[71] H Julian Allen et al. *Wall interference in a two-dimensional-flow wind tunnel with consideration of the effect of compressibility*. Tech. rep. US Government Printing Office, 1944.

[72] Haley Dell’Orso et al. “Measurement of three-dimensional stall cells on a two-dimensional NACA0015 airfoil”. In: *AIAA Journal* 54.12 (2016), pp. 3872–3883.

[73] Jinhee Jeong et al. “On the identification of a vortex”. In: *Journal of fluid mechanics* 285 (1995), pp. 69–94.

[74] Mogeng Li et al. “Stall cells organisation on an aerofoil with leading-edge tubercles”. In: (2024).

[75] Brian Maskew. *Program VSAERO theory Document: a computer program for calculating nonlinear aerodynamic characteristics of arbitrary configurations*. Tech. rep. NASA, 1987.

A
Test matrix

Main Campaign					
#	AoA [deg]	Inflow velocity [m/s]	Re	dt [us]	Power [%]
Block 1: A05L25, x/c = 0.15					
1	0	5	33333	30	85
2	5	5	33333	30	85
3	5	2	13333	75	85
4	5	15	100000	10	85
5	10	5	33333	30	85
6	15	5	33333	30	85
7	20	5	33333	30	85
8	25	5	33333	30	85
9	30	5	33333	30	85
Block 2: A10L25, x/c = 0.15					
10	0	5	33333	30	85
11	5	5	33333	30	85
12	5	2	13333	75	85
13	5	15	100000	10	85
14	10	5	33333	30	85
15	15	5	33333	30	85
16	20	5	33333	30	85
17	25	5	33333	30	85
18	30	5	33333	30	85
Block 3: A05L25, x/c = 0.25					
19	0	5	33333	30	80
20	5	5	33333	30	80
21	10	5	33333	30	80
22	15	5	33333	30	80
23	20	5	33333	30	80
24	25	5	33333	30	80
25	30	5	33333	30	80
26	5	2	13333	30	80
27	5	15	100000	30	80
28	5	15	100000	20	80
29	5	2	13333	75	80
30	5	15	100000	10	80
Block 4: A10L25, x/c = 0.25					
31	0	5	33333	30	80
32	5	5	33333	30	80
33	5	2	13333	75	80
34	5	15	100000	10	80
35	10	5	33333	30	80
36	15	5	33333	30	80
37	20	5	33333	30	80
38	25	5	33333	30	80
39	30	5	33333	30	80
Block 5: A05L25, x/c = 0.45					
40	0	5	33333	30	85
41	5	5	33333	30	85
42	5	2	13333	75	85

43	5	15	100000	10	85
44	10	5	33333	30	85
45	20	5	33333	30	85
Block 6: A10L25, x/c = 0.45					
46	0	5	33333	30	85
47	5	5	33333	30	85
48	5	2	13333	75	85
49	5	15	100000	10	85
Block 7: A05L25, x/c = 0.6					
50	0	5	33333	30	80
51	5	5	33333	30	80
52	5	2	13333	75	80
53	5	15	100000	10	80
54	10	5	33333	30	80
55	20	5	33333	30	80
Block 8: A10L25, x/c = 0.6					
56	0	5	33333	30	80
57	5	5	33333	30	80
58	5	2	13333	75	80
59	5	15	100000	10	80
Block 9: A05L25, x/c = 0.8					
60	0	5	33333	30	80
61	5	5	33333	30	80
62	5	2	13333	75	80
63	5	15	100000	10	80
64	10	5	33333	30	80
65	20	5	33333	30	80
Block 10: A10L25, x/c = 0.8					
66	0	5	33333	30	80
67	5	5	33333	30	80
68	5	2	13333	75	80
69	5	15	100000	10	80
Block 11: A05L25, x/c = 1.0					
70	0	5	33333	30	80
71	5	5	33333	30	80
72	5	2	13333	75	80
73	5	15	100000	10	80
74	10	5	33333	30	80
75	20	5	33333	30	80
Block 12: A10L25, x/c = 1.0					
76	0	5	33333	30	80
77	5	5	33333	30	80
78	5	2	13333	75	80
79	5	15	100000	10	80
Extra Campaign					
Block 13: A05L25, x/c = 0.15					

80	5	2	13333	150	90
81	5	5	33333	60	90
82	5	15	100000	20	90
83	10	2	13333	150	90
84	10	5	33333	60	90
85	10	15	100000	20	90
86	15	2	13333	150	90
87	15	5	33333	60	90
88	15	15	100000	20	90
Block 14: A010L25, x/c = 0.15					
89	5	2	13333	150	90
90	5	5	33333	60	90
91	5	15	100000	20	90
92	10	2	13333	150	90
93	10	5	33333	60	90
94	10	15	100000	20	90
95	15	2	13333	150	90
96	15	5	33333	60	90
97	15	15	100000	20	90

B

Spectral NLLT Algorithm

A pseudo-code of the spectral NLLT algorithm is given below. Note that the main difference from the spatial NLLT is that the quantity to iterate is changed from the bound vortex circulation to the mode amplitude.

Algorithm 1: Spectral NLLT pseudo code

Data: input airfoil Cl-AoA data, wing geometry, spatial basis frequency, number of modes N, initial amplitudes of modes, wind tunnel width, parameters for spanwise discretization, parameters for iteration, etc.

Result: $\Gamma(x), C_l(x), \alpha_i(x)$, converged amplitudes of different modes, etc.

```
initialization;
while error < convergence criterion do
    Update amplitudes A(N) = old A(N) + damping factor * (new A(N) - old A(N));
    Calculate induced velocity w(x);
    Calculate effective AoA a(x);
    Calculate circulation Γ(x) and C_l(x);
    Conduct the Fourier transform on Γ(x) to obtain new amplitude A(N) of each mode, with the
      filter applied on amplitudes of high-frequency components;
end
```

C

Crow's model derivation

The vortex system used by Crow is a pair of counter-rotating vortices of the same strength. The setup is shown in Figure 1.15. The Biot-Savart law is applied to calculate the induced velocity at a segment on the n^{th} vortex filament:

$$\mathbf{U}_n = \sum_{m=1}^{2} \Gamma_m \int \frac{\mathbf{R}_{mn} \times \mathrm{d}\mathbf{L}_m}{4\pi |\mathbf{R}_{mn}|^3}. \tag{C.1}$$

The $\mathbf{R}_{mn}$ is a distance vector, in the direction from the segment where the induced velocity is calculated, to the vortex segment inducing the velocity and it can be computed from:

$$\mathbf{R}_{mn} = \mathbf{e}_x(x'_m - x_n) + \mathbf{e}_y(s_m - s_n) + (\mathbf{r}'_m - \mathbf{r}_n), \tag{C.2}$$

where the first two terms represent the distance in x and y direction when there is no perturbation, and the last term stands for the distance in y and z direction caused by the radial displacement perturbations, and it is in the form of $\mathbf{r}_n = \mathbf{e}_y y_n(x_n, t) + \mathbf{e}_z z_n(x_n, t)$, which is a function of the position on the x axis and time. The prime symbol is used to avoid confusion when both vortex segments under consideration are on the same vortex filament. s is a fixed value, which can be either $b/2$ or $-b/2$, representing the nominal (without perturbations) position of the filament in the y direction.

The $\mathrm{d}\mathbf{L}_m$ in Equation (C.1) is the length vector of a vortex segment, which is illustrated in Figure C.1, and it can calculated from:

$$d\mathbf{L}_n = (\mathbf{e}_x + \partial \mathbf{r}_n / \partial x_n) dx_n. \tag{C.3}$$

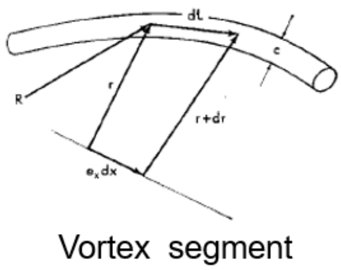

Figure C.1: Relation between an arc-length $\mathrm{d}\mathbf{L}_m$ and a displacement down the longitudinal axis.

So far, we have obtained three equations for four unknowns: $\mathbf{U}_n$, $\mathbf{R}_{mn}$, $\mathbf{r}_n$, and $\mathrm{d}\mathbf{L}_n$. To close the system of equations, the vorticity-transport theorem is used, which means the vortex segment moves with fluid particles in an inviscid and neutrally buoyant fluid. Mathematically, it means:

$$D\mathbf{r}_n/Dt = \partial \mathbf{r}_n/\partial t + u_n(\partial \mathbf{r}_n/\partial x_n) = \mathbf{e}_y v_n + \mathbf{e}_z w_n. \tag{C.4}$$

The convection terms in y and z directions have no contributions as the radial displacement is a function of x and t.

Substituting Equation (C.2), Equation (C.3), and Equation (C.4) into Equation (C.1), we can obtain:

$$\begin{aligned}\mathbf{U}_n = \sum_{m=1}^{2}\frac{\Gamma_m}{4\pi}\Bigg\{&\mathbf{e}_x\int_{-\infty}^{\infty}\frac{(s_m-s_n)(\partial z'_m/\partial x'_m)dx'_m}{[(x'_m-x_n)^2+(s_m-s_n)^2]^{3/2}}+\\ &\mathbf{e}_y\int_{-\infty}^{\infty}\frac{[(z'_m-z_n)-(x'_m-x_n)(\partial z'_m/\partial x'_m)]}{[(x'_m-x_n)^2+(s_m-s_n)^2]^{3/2}}dx'_m+\\ &\mathbf{e}_z\int_{-\infty}^{\infty}\frac{[(x'_m-x_n)(\partial y'_m/\partial x'_m)-(s_m-s_n+y'_m-y_n)]}{[(x'_m-x_n)^2+(s_m-s_n)^2]^{3/2}}dx'_m\Bigg\}\end{aligned} \tag{C.5}$$

The expression can be linearized by assuming the radial displacement is small enough compared to the spacing b and the vortex segment slope is much smaller than 1, meaning: $|\mathbf{r}_n|/b \ll 1$ and $|\partial \mathbf{r}_n/\partial x_n| \ll 1.$

The linearization process will be given below by taking the last term in Equation (C.5) as an example. The coefficient of the $\mathbf{e}_z$ can be written as:

$$f(y,z) = \frac{x(\partial y'_m/\partial x'_m)-(s+y)}{[x^2+(s+y)^2+z^2]^{3/2}}, \tag{C.6}$$

where $x = x'_m - x_n, y = y'_m - y_n, z = z'_m - z_n$, and $s = s_m - s_n$. $f(y,z)$ is a multiple-variable function and it can linearized in the following way by assuming y, z are both small quantities:

$$f_L(y,z) = f(0,0) + \frac{\partial f}{\partial y}\Big|_{(0,0)} y + \frac{\partial f}{\partial z}\Big|_{(0,0)} z. \tag{C.7}$$

After expansion and simplication, Equation (C.7) gives:

$$\begin{aligned}f_L(y,z) = &\frac{x(\partial y'_m/\partial x'_m)-s}{(x^2+s^2)^{3/2}} + [\frac{x(\partial^2 y'_m/\partial x'_m \partial y)-1}{(x^2+s^2)^{3/2}} - \frac{3s(x\partial y'_m/\partial x'_m - s)}{(x^2+s^2)^{5/2}}]\cdot y\\ &+0\cdot z\end{aligned} \tag{C.8}$$

Since the perturbation should be continuous, the second derivative term $(\partial^2 y'_m/\partial x'_m \partial y)$ can be rewritten to be $(\partial^2 y'_m/\partial y \partial x'_m)$, which is zero. If the second-order small terms are left out:

$$f_L(y,z) = \frac{x(\partial y'_m/\partial x'_m)-(s+y)}{(x^2+s^2)^{3/2}} - \frac{3s^2 y}{(x^2+s^2)^{5/2}}. \tag{C.9}$$

The linearization process can be applied to the $\mathbf{e}_x$ and $\mathbf{e}_y$ terms in Equation (C.5) as well and the linearized expression for $\mathbf{U}_n$ is:

$$\begin{aligned}\mathbf{U}_n = \sum_{m=1}^{2}\frac{\Gamma_m}{4\pi}\Bigg\{&-\mathbf{e}_z\int_{-\infty}^{\infty}\frac{(s_m-s_n)dx_m}{[(x'_m-x_n)^2+(s_m-s_n)^2]^{3/2}}+\\ &\mathbf{e}_x\int_{-\infty}^{\infty}\frac{(s_m-s_n)(\partial z'_m/\partial x'_m)dx'_m}{[(x'_m-x_n)^2+(s_m-s_n)^2]^{3/2}}+\\ &\mathbf{e}_y\int_{-\infty}^{\infty}\frac{[(z'_m-z_n)-(x'_m-x_n)(\partial z'_m/\partial x'_m)]}{[(x'_m-x_n)^2+(s_m-s_n)^2]^{3/2}}dx'_m+\\ &\mathbf{e}_z\int_{-\infty}^{\infty}\Bigg(\frac{3(s_m-s_n)^2(y'_m-y_n)}{[(x'_m-x_n)^2+(s_m-s_n)^2]^{5/2}}-\\ &\frac{[(y'_m-y_n)-(x'_m-x_n)(\partial y'_m/\partial x'_m)]}{[(x'_m-x_n)^2+(s_m-s_n)^2]^{3/2}}\Bigg\}dx'_m\end{aligned} \tag{C.10}$$

Substitute Equation (C.10) into the Equation (C.4), and ignore the second-order effect (i.e., longitudinal convection), the kinematic relation becomes:

$$
\begin{aligned}
&\frac{\partial \mathbf{r}_n}{\partial t} = \sum_{m=1}^{2} \frac{\Gamma_m}{4\pi} \times \\
&\Bigg\{ \mathbf{e}_y \int_{-\infty}^{\infty} \frac{[(z_m{}' - z_n) - (x_n{}' - x_n)(\partial z_m{}'/\partial x_m{}')]}{[(x_m{}' - x_n)^2 + (s_m - s_n)^2]^{3/2}} dx_m{}' + \\
&\mathbf{e}_z \int_{-\infty}^{\infty} \Bigg(\frac{3(s_m - s_n)^2 (y_m{}' - y_n)}{[(x_m{}' - x_n)^2 + (s_m - s_n)^2]^{5/2}} - \\
&\frac{[(y_m{}' - y_n) - (x_m{}' - x_n)(\partial y_m{}'/\partial x_m{}')]}{[(x_m{}' - x_n)^2 + (s_m - s_n)^2]^{3/2}} \Bigg) \Bigg\} dx_m{}'
\end{aligned}
\tag{C.11}
$$

.

The above equation admits a solution in the exponential form: $\mathbf{r}_n = \hat{\mathbf{r}}_n e^{at+ikx_n} = (\mathbf{e}_y \hat{y}_n + \mathbf{e}_z \hat{z}_n) e^{at+ikx_n}$, and the $k = \frac{2\pi}{\lambda}$, where λ is the wavelength of the perturbation. We can feed the solution in such a form into the dynamic system to examine its evolution. Plugging the solution into the system would transform the integro-differential equation into a system of algebraic equations for the perturbation vector $\hat{\mathbf{r}}_n$. Take $\hat{\mathbf{r}}_1$ for example:

$$
\begin{aligned}
a\hat{y}_1 = -&\frac{\Gamma_2}{2\pi} \hat{z}_1 \int_0^{\infty} \frac{dx}{(x^2 + b^2)^{3/2}} + \\
&\frac{\Gamma_2}{2\pi} \hat{z}_2 \int_0^{\infty} \frac{\text{cos}kx + kx\text{sin}kx}{(x^2 + b^2)^{3/2}} dx + \\
&\frac{\Gamma_1}{2\pi} \hat{z}_1 \int_d^{\infty} \frac{\text{cos}kx + kx\text{sin}kx - 1}{x^3} dx
\end{aligned}
\tag{C.12}
$$

$$
\begin{aligned}
a\hat{z}_1 = -&\frac{\Gamma_2}{2\pi} \hat{y}_1 \int_0^{\infty} \frac{dx}{(x^2 + b^2)^{3/2}} + \\
&\frac{\Gamma_2}{2\pi} \hat{y}_2 \int_0^{\infty} \frac{\text{cos}kx}{(x^2 + b^2)^{3/2}} dx - \\
&\frac{\Gamma_1}{2\pi} \hat{y}_1 \int_d^{\infty} \frac{\text{cos}kx + kx\text{sin}kx - 1}{x^3} dx
\end{aligned}
\tag{C.13}
$$

d is the distance of cut-off, which represents the influence of vortex core: anything happens within the sphere with radius being cut-off distance is ignored. Similar results for $\hat{\mathbf{r}}_2$ can be obtained by changing the subscript and sign of each term. In the end, the dynamic system of the perturbation vector $\hat{\mathbf{r}}_n$ can be established using dimensionless quantities:

$$
\begin{aligned}
\alpha\hat{y}_1 &= -\hat{z}_1 + \psi\hat{z}_2 - \beta^2\omega\hat{z}_1 \\
\alpha\hat{z}_1 &= -\hat{y}_1 + \chi\hat{y}_2 + \beta^2\omega\hat{y}_1 \\
\alpha\hat{y}_2 &= \hat{z}_2 - \psi\hat{z}_1 + \beta^2\omega\hat{z}_2 \\
\alpha\hat{z}_2 &= \hat{y}_2 - \chi\hat{y}_1 - \beta^2\omega\hat{y}_2,
\end{aligned}
\tag{C.14}
$$

where:

$$
\begin{aligned}
\chi(\beta) = \beta K_1(\beta),\ &\psi(\beta) = \beta^2 K_0(\beta) + \beta K_1(\beta), \\
\omega(\delta) = \frac{1}{2}&[(\text{cos}\delta - 1)/\delta^2 + \text{sin}\delta/\delta - Ci(\delta)].
\end{aligned}
\tag{C.15}
$$

K_1 and K_2 are the Bessel functions of the second type, Ci is the integral cosine. All of these can be calculated conveniently using MATLAB. β is the non-dimensionalized wavenumber (i.e., kb), and δ is the dimensionless cut-off distance (i.e., kd).

The dynamic system can be decomposed into symmetric and anti-symmetric modes as below, which can simplify the stability analysis as the eigenvalues can be easily obtained.

$$\begin{aligned} \hat{y}_S &= \hat{y}_2 - \hat{y}_1, z_S = \hat{z}_2 + \hat{z}_1 \\ \hat{y}_A &= \hat{y}_2 + \hat{y}_1, \hat{z}_A = \hat{z}_2 - \hat{z}_1 \end{aligned} \tag{C.16}$$

Now, both modes are fully decoupled. The mode can be regarded as a stand-alone dynamic problem, which can capture certain aspects of the original problem.